Flavor-Changing Neutral Currents at Hadron Colliders

Habilitationsschrift

vorgelegt der

Mathematisch-naturwissenschaftlichen Fakultät

der

Universität Zürich

von

Frank Lehner

aus

Deutschland

Zürich im Dezember 2005

Contents

1 Introduction

The fascinating area of the quark flavor structure and its CP violation in the Standard Model (SM) has become to one of the most interesting topics in present day particle physics. Unlike the well-tested gauge sector of the SM, several mysteries and puzzles in flavor physics do still exist. Why do we have three generations of fermions? Where do fermions get their mass? What is the origin of mixing and CP violation? Experimental results on heavy quarks, particularly in the B system, are challenging the SM more and more with increasing precision and are trying to shed more light on those questions.

Measurements and investigations in the B system have moved into the focus of many experiments. With the advent of two dedicated B-factories in the US and Japan in the year 1999, a very exciting era for precision flavor physics has begun. Over the last six years we have witnessed many exciting B physics results from the two experiments Babar at SLAC and Belle at KEK and we will expect even more results to come. In 2001 the Tevatron hadron collider at Fermi National Acceerator Laboratory has started its operation. In Tevatron's Run II the study of B physics comprises an essential part of its rich physics program and many interesting results that are partially complementary to the B-factories have been presented so far. Moreover, in the very near future the Large Hadron Collider (LHC) will take up its operation in 2007 providing the most copious b-quark production source at that time. The LHCb experiment at LHC will then be a dedicated experiment capable to study and investigate B physics at new precision levels, and Atlas & CMS will pursue own B physics programs as well. More related to the mid-term future are ambitious upgrade plans to convert the running B machines at SLAC and KEK into Super-B factories with the ultimate goal to reach more than one order of magnitude in statistics than at present.

The B physics program at the B-factories, at the running Tevatron and at the upcoming LHC is focusing clearly on two major points: The detailed exploration of CP violation in B decays on the one hand, and the precise measurement of rare flavor-changing neutral current (FCNC) processes on the other hand with the goal to find or at least constrain new physics.

The question that one may ask is why all these experimental and theoretical efforts in B physics? The answer can be simply phrased that flavor physics is ultimately related to electroweak symmetry breaking and thus is probing the Higgs field of the SM and/or any other scalar sector of physics models beyond that. The effects of both, quark mixing and CP violation are inseparably connected to the fact that quarks have mass. CP symmetry is in fact a natural consequence of massless gauge theories, such that any CP violation is intrinsically tied to the mass generation mechanism, i.e., the Higgs mechanism in the SM. Thus, the information on the scalar sector that is obtained from B decays can give complementary information to direct Higgs searches and direct searches for new particles. A complete picture of the Standard Model of electroweak symmetry breaking and mass generation can only be gained if the complete picture of direct and indirect results are put together.

Why is the B system so well-suited for such a fundamental physics program? The answer is partially related to the rareness of FCNC processes in the SM. FCNC transitions are absent at tree level in the SM but appear in higher order diagrams through so-called box and penguin processes. Since the observed quark mass hierarchy dictates the top quark to be much heavier than all the other five quarks, its large mass relaxes natural loop-suppression in the B system that is normally effective in box- and penguin diagrams. The relaxation leads also to a large B_d^0 mixing phase, giving sizeable and observable CP-violating effects in B decays, making

the B system to an ideal laboratory for the investigation of fundamental CP-phenomena.

Typical rare B decays with FCNC transitions have branching ratios that are of the order of 10^{-6}, which is by orders of magnitude larger than in corresponding K and D decays and are thus much easier accessible by experiment. The detailed study of rare FCNC decays is important to find or constrain effects of new physics. The experimental results on the FCNC transition $b \to s\gamma$ for instance, provide severe constraints on charged Higgs masses, sfermion masses and mixing in supersymmetric models. Such indirect tests offer complementary information to direct searches by restricting the parameter space of supersymmetric models as important clues for a future direct search program.

Rare decays are in particular interesting, if more than only one Higgs doublet as in the SM exist. In fact, supersymmetric extensions beyond the SM require minimally two Higgs doublets with flavor violating couplings leading to new sources of flavor-changing neutral currents at large $\tan\beta$, i.e., the ratio of the vacuum expectation values of the Higgs fields. The branching fractions of several rare B meson decays can then be significantly enhanced. Large values of $\tan\beta$ are theoretically interesting since in this region a unification of Yukawa couplings between b and t quarks seems possible. It is an another exciting feature of rare decays, that FCNC transitions via the Higgs bosons do not decouple, i.e., their loop contribution to low energy processes depends only on mass ratios and remains therefore finite. Thus, those flavor violating processes can even then be observed if the new supersymmetric particles are so heavy that a direct detection of a supersymmetric signal is not possible.

Finally, the B system provides an ideal laboratory to apply the framework and tools of perturbative QCD in a quantitative way. This is solely due to fact that the b-quark mass is much larger than the typical scale of the strong interaction Λ_{QCD}. Non-perturbative QCD effects that are arising from long-distances are generally less important and under better control than in other (light) hadron systems. The available perturbative tools allow relative precise calculations and predictions for various rare B decays in the SM and in many extended models that can be confronted with experimental data.

The structure of this work is as follows: After these introductional words the second chapter reviews the experimental conditions and requirements which are necessary to pursue a successful B physics program. The hadron colliders Tevatron and LHC with the experiments DØ and LHCb are described. Emphasis is given on the two silicon detectors for DØ and LHCb, which are essential for precise vertex and tracking information. The third chapter starts with a brief history of FCNC decays and introduces into the theoretical framework of rare B decays such as the operator product expansion. In this part, the general sensitivity of FCNC decays to new physics is also discussed. Chapter four presents an extensive overview of all relevant rare B decays with their current experimental status and their sensitivity to new physics. In this regard, particular attention deserves the most promising decay channel $B_s^0 \to \mu^+\mu^-$. Its numerous impacts on models of new physics is reviewed. Chapter 5 describes the experimental aspects for rare B decay searches at Tevatron in more detail and presents the prospects for a FCNC program in B physics at LHC. Finally, the last chapter summarizes the main conclusions.

2 Experimental Environment for B Physics

The studies in the B system offer an exciting and large window for precision SM tests and for indirect searches of new physics. This window is open to all experimental facilities that are able to produce b-flavored particles in collisions or decay. This chapter starts with the experimental environment necessary to perform a B physics program. Different types of collider machines offer various advantages and disadvantages depending on the type of b-production. Thanks to their long life time, the hadrons containing a b-quark drift a considerably long distance away from the primary interaction vertex before they decay. High resolution vertex detectors are therefore necessary to resolve the decay length and to isolate the secondary from the primary vertex. Two examples of silicon detectors are therefore discussed.

2.1 Experimental Facilities for B Physics

Currently, B physics is studied in e^+e^- collisions at KEK and SLAC, at the hadron collider Tevatron at Fermilab and at the HERA ep collider at DESY. In 2007, when the Large Hadron Collider LHC at CERN will start its operation, it will be by far the most copious $b\bar{b}$ production source of the world.

2.1.1 Machines with e^+e^- Annihilation

The two present B experiments at e^+e^- machines are operating at the $\Upsilon(4S)$ resonance. These are the Babar experiment [1] at the PEP-II collider at SLAC and the Belle experiment [2] at KEK. Just until recently, also CLEO at Cornell has taken data at the $\Upsilon(4S)$ resonance.

Although the $\Upsilon(4S)$ has a smaller production cross section than the first three Υ resonances, it is used because it is the first one which is massive enough to produce B mesons in its decay. The B production cross section for a e^+e^- machine at the $\Upsilon(4S)$ resonance is only 1.1 nb. Its ratio to the total hadronic cross section $\sigma_{b\bar{b}}/\sigma_{had}$ however, is 0.22, which is larger than at any other B production facility, in particular orders of magnitude larger than at hadron colliders.

The $\Upsilon(4S)$ resonance is only little above the B pair production threshold, but can only decay into $B^0\bar{B}^0$ or B^+B^- pairs with equal fractions. After their production, the B mesons are moving very slowly in the center of mass system of the $\Upsilon(4S)$ and travel only 30 μm before decaying. Thus, for a symmetric e^+e^- machine producing the $\Upsilon(4S)$ at rest, it is not possible to measure life times or time-dependent characteristics of their decays, since existing position sensitive vertex detectors have resolutions not much better than 10 μm. To overcome this problem, the two existing B factories PEP-II and KEK-B have asymmetric beams with head-on collisions but different momenta in the center-of-mass system. In the final state, the resulting B mesons have then a boost resulting in a mean flight length of about 250 μm in the laboratory system.

The $\Upsilon(4S)$ state decays only into B mesons with light (u, d) spectator quarks. Other b-flavored species such as B_s^0, $B_c^\pm$ or heavier b-baryons are not accessible at such machines, unless the more massive $\Upsilon(5S)$ state is resonantly produced at the cost of a lower $\Upsilon(5S)$ production cross section. The $\Upsilon(5S)$ is about 40 MeV above $B_s^*\bar{B}_s^*$ pair production threshold and could then allow a production of B_s^0 mesons through $B_s^* \to B_s^0\gamma$ decays.

Several hundred millions of B decays have been detected by the experiments Belle and Babar due to the large instantaneous luminosities of about 10^{34} cm^{-2}s^{-1} of their machines. Up to now (end of Nov 2005) the recorded luminosities of the two detectors were 300 fb^{-1} for Babar and 500 fb^{-1} for Belle.

The clear advantages of e^+e^- annihilation machines operating at the $\Upsilon(4S)$ are their low non-B background with the possibility to trigger on and record all $B\bar{B}$ events. The events are relatively clean, with a mean charged track multiplicity of about 10. In addition, the initial state is composed just of a $B\bar{B}$ meson pair, making it simple to apply powerful kinematical constraints to identify specific final states or to reconstruct inclusive decays like $b \to s\gamma$, or decays with missing particles like neutrinos.

For the mid-term future, there exist proposals to upgrade the existing asymmetric e^+e^- machines at KEK and SLAC and convert them into Super-B factories [3] with the ultimate goal of reaching an instantaneous luminosity of up to 10^{36} cm^{-2}s^{-1} by the year 2015 and to collect a luminosity corresponding to several ab^{-1} already by 2010. Discussions to operate these facilities at the $\Upsilon(5S)$ state are also on-going. This would then have the advantage to access B_s^0 mesons through the decay chain $\Upsilon(5S) \to B_s^* \bar{B}_s^*$ with subsequent decay of B_s^* into $B_s^0\gamma$ states. First B_s^0 mesons from B_s^* decays have been just recently observed at CLEO [4] with a measured production cross section of $\sigma(e^+e^- \to B_s^*\bar{B}_s^*) = 0.11^{+0.04}_{-0.03}(\text{stat.}) \pm 0.02(\text{sys.})$ nb.

At the Z-boson resonance of $\sqrt{s} = 91$ GeV at which e^+e^- machines like LEP and SLC were running in the years from 1990 to 1998 the $b\bar{b}$ cross section reaches 7.0 nb. All types of b-flavored hadrons could be produced through the fragmentation of a b-quark from $Z \to b\bar{b}$ decays into B mesons or baryons. The produced B mesons were highly relativistic with an average boost of $< \beta\gamma > \approx 6$ making lifetime-dependent measurements possible.

Finally, as long-term future for B physics at e^+e^- machines, there is the plan to initially run the next linear collider (ILC) at the Z-pole and collect more than a billion Z events. This Giga-Z collider targets for ultra-high precision electroweak measurements, but represents also a formidable $Z \to b\bar{b}$ source with a potential B program that has not yet been fully exploited.

2.1.2 Machines with Hadron Collisions

Hadron machines running either in fixed target of collider mode offer in contrast to e^+e^- machines a huge $b\bar{b}$ cross section $\sigma_{b\bar{b}}$. The cross section at a center of mass energy $\sqrt{s}$ can be written as:

$$\sigma_{b\bar{b}}(s) = \sum_{i,j} \int dx_1 dx_2 q_i(x_1) q_j(x_2) \hat{\sigma}_{ij \to b\bar{b}}(\hat{s} = x_1 x_2 s). \tag{2.1}$$

Here, $q_{i,j}$ are the parton distribution functions of the colliding hadrons, and $\hat{\sigma}_{ij \to b\bar{b}}$ is the short-distance cross section, which is presently calculated in NLO QCD perturbation theory [5] and some terms in NNLO already exist. In LO QCD, the relevant processes for the production of a heavy quark Q in hadron-hadron collisions are quark-antiquark scattering $q + \bar{q} \to Q + \bar{Q}$ and gluon-gluon fusion $g + g \to Q + \bar{Q}$. The mass of a heavy quark $m_Q \gg \Lambda_{QCD}$ is the large scale of the process and provides a lower cut-off in the virtuality of the off-shell propagators controlling the perturbative expansion in terms of $\alpha_s(m_Q)$. Such a perturbative control is not possible for light quarks, where masses are below Λ_{QCD}. In LO production, the heavy quarks have transverse momenta of the order of the mass m_Q and are produced close in

rapidity. NLO corrections change the overall size but not the shape of transverse momentum and rapidity distribution.

Previously observed discrepancies [6] of the $b\bar{b}$ production cross section between Tevatron measurements and NLO theory of up to a factor of three have been successfully eliminated [7] after a careful reconsideration of the b-quark fragmentation functions and resummation of subleading terms of $\log p_t/m_b$. There is now a good agreement between experimental data on $b\bar{b}$ production and theory.

At high energies, the $b\bar{b}$ cross section is rising strongly with $\sqrt{s}$, while the total hadronic cross section increases only moderately, obtaining a more favorable ratio of $\sigma_{b\bar{b}}/\sigma_{had}$ towards higher energies. A $b\bar{b}$ production cross section of almost 100 μb is achieved at the $p\bar{p}$ collider Tevatron with a center of mass energy of $\sqrt{s} = 2$ TeV leading to a ratio $\sigma_{b\bar{b}}/\sigma_{had} \approx 10^{-3}$. At the LHC with $\sqrt{s} = 14$ TeV, the cross section for $b\bar{b}$ production is even five times larger, while the total hadronic cross section rises only slightly.

For a typical accelerator year of 10^7 s and a luminosity of 2×10^{32} cm^{-2}s^{-1}, $\mathcal{O}(10^{12})$ $b\bar{b}$ pairs are produced (expected) every year. However, only about 0.1% at Tevatron and 0.5% at LHC of all collisions are related to $b\bar{b}$ production. The overwhelming majority of collisions are considered to be background processes, which have to be rejected by designated online and offline selections.

One of the characteristic features of $b\bar{b}$ production at hadron colliders at higher energies is a relatively flat rapidity distribution of the produced b-quarks centered around $\eta = 0$. The distribution is fairly broad and falls off towards higher rapidities. In rapidity, the range of significant b-quark production with high transverse momentum p_t is for Tevatron about ± 3 and for LHC ± 5. A flat and broad rapidity distribution means also that b-quark production at hadron colliders is preferentially at small polar angles and this effect is more pronounced the higher $\sqrt{s}$ is.

The more forward the b-quark, the higher is its Lorentz-boost, making it easier to identify the b-decay by its detached vertex. The boost of the b-quarks in the forward direction can be intuitively explained from the different proton momenta fractions x_i of the initial state partons i involved in the hard scattering process. When the center-of-mass energy of the hadron collisions increase, the momentum difference also increases, resulting in a larger boost in the forward direction.

Hadron colliders provide another important feature of $b\bar{b}$ production. There is a strong correlation between the $b\bar{b}$ pair in the forward (and backward) direction. When one b-quark is produced in a forward direction, then also the other $\bar{b}$-quark is forward, i.e., on the same side of the detector. This correlation is not much pronounced in the central rapidity region.

This is interesting, since many CP violating measurements require the reconstruction of one B decay, while flavor tagging the other b-quark in the event. Thus, the observation of both b-quarks in the detector is of great experimental relevance. The high correlation of both b-quarks in the forward directions allows to instrument only a small part of the forward hemisphere with detectors to collect sufficiently large samples of $b\bar{b}$ pairs. This feature is exploited in the design of the LHCb experiment at LHC and the BTeV[1] experiment at Tevatron, which are both setup as forward spectrometers.

B physics was also studied at hadron fixed target experiments. The experiment HERA-B finished its operation in 2004 and was the latest example of a fixed target hadronic B facility.

[1] In the mean time the BTeV experiment has been canceled.

Table 2.1: Some parameters of experimental facilities for B physics. The luminosity for Atlas/CMS refers to the initial LHC phase only.

Experiment	Type	$\mathcal{L}$ ($\mathrm{cm}^{-2}\mathrm{s}^{-1}$)	$\sqrt{s}$	$\sigma_{b\bar{b}}$	$\sigma_{b\bar{b}}/\sigma_{had}$	boost $< \beta\gamma >$
CLEO III	e^+e^-	1.7×10^{33}	$\Upsilon(4S)$	1.1 nb	0.25	0.06
BaBar/Belle	e^+e^-	10^{34}	$\Upsilon(4S)$	1.1 nb	0.25	≈ 0.5
LEP	e^+e^-	10^{30}	91 GeV	12 nb	0.15	6
CDF/DØ	$p\bar{p}$	10^{32}	1.96 TeV	100 μb	$\approx 10^{-3}$	2-5
HERA-B	pA	int rate 40 MHz	43 GeV	7 nb	$\approx 10^{-6}$	≈ 25
LHCb	pp	2×10^{32}	14 TeV	500 μb	5×10^{-3}	15-20
Atlas/CMS	pp	10^{33}	14 TeV	500 μb	5×10^{-3}	≈ 15

A wire target was used in the halo of the proton beam at HERA providing collisions at $\sqrt{s} = 43$ GeV. The produced B mesons from the fixed target are highly boosted and emitted in the forward direction with a typical energy of about 100 GeV and a long B flight length of about 1 cm. On the other hand, the boost focuses all the particles in a narrow cone, making precision vertexing and momentum reconstruction rather complicated. In addition, the background environment at HERA-B was a huge challenge for online and offline selection due to a small ratio $\sigma_{b\bar{b}}/\sigma_{had} \sim 10^{-6}$.

Finally, access to B physics is also possible at the ep collider HERA. The visible production cross section however, is only about 700 pb, while the total hadronic cross section dominated by photoproduction amounts to $\sigma_{had} = 100$ μb.

A compilation of various facilities that allow the study of B physics is given in Tab. 2.1.

2.2 Fragmentation

At high energy colliders all species of b-flavored hadrons are produced. This happens either directly with the initial production of a b-quark in the hard scatter process and its subsequent hadronization into mesons or baryons or through strong or electromagnetic decays of excited b-hadrons. If the hadronization process itself provides an initial hard scale, as it is the case in high-p_t b-jets originating from Z^0 decays or from $p\bar{p}$ collisions at Tevatron, is it plausible to assume a production independent b-fragmentation. This means that the fraction of the different b-type mesons or baryons after the hadronization of a b-quark is the same for $Z^0 \to b\bar{b}$ and for high energy $p\bar{p} \to b\bar{b}X$ collisions. Although there is no strong theoretical argument to support this assumption, it is adopted as a pragmatic approach in the review [8] of the particle data group (PDG), as long as no new experimental data contradict. The b-hadron fractions f_i of an initial b-quark to form a hadron, i.e., a $B^{\pm}$, B_d^0 or B_s^0 meson or a b-baryon are then estimated from averaged LEP and Tevatron data. It is further assumed that the B^+ and B_d^0 mesons are produced equally, such that $f_u = f_d$. This assumption can be justified by SU(2) isospin symmetry. Moreover, weakly decaying states made of heavy quarks such as the B_c^+ and other heavy baryons are neglected and known to contribute only little. The fragmentation fractions are constraint to be

$$f_u + f_d\,(= f_u) + f_s + f_{baryon} = 1. \tag{2.2}$$

Table 2.2: The world average fragmentation values for b-quarks into mesons and baryons [9].

b hadron species	fraction	Correlation coefficient with $f_d = f_u$ and f_s
B^0, B^+	$f_d = f_u = 0.399 \pm 0.010$	
B_s^0	$f_s = 0.102 \pm 0.014$	-0.564
b Baryons	$f_{baryon} = 0.100 \pm 0.017$	-0.724 -0.162

Table 2.2 shows the Tevatron and LEP averaged fragmentation fractions and their correlations taken from [9]. The fractions are obtained from direct measurements at LEP such as $f_s \times \mathcal{B}(B_s^0 \to D_s^- \ell^+ \nu_l X)$, $\mathcal{B}(b \to \Lambda_b^0) \times \mathcal{B}(\Lambda_b^0 \to \Lambda_c^+ \ell^- \bar{\nu}_\ell X)$ and $\mathcal{B}(b \to \Xi_b^-) \times \mathcal{B}(\Xi_b^- \to \Xi^- \ell^- \bar{\nu}_\ell X)$. The determination of the b-hadron fraction at Tevatron include the measurements of electron-charm final states states and double-semileptonic decays with $\phi\ell^\pm$ and $K^*\ell^\pm$ final states. In addition time-integrated mixing analyses performed with lepton pairs from $b\bar{b}$ events can be used to significantly improve the knowledge of the fragmentation functions f_i.

The present value for the fragmentation f_s using Run I Tevatron data [10] alone is $f_s = 0.120 \pm 0.021$, i.e., somewhat larger than the LEP/Tevatron combined number. It is expected that new Run II data will improve on the fragmentation measurements such that more precise hadron collider fragmentation values are available before LHC starts.

2.3 Tevatron and LHC

The **Tevatron** at Fermi National Accelerator Laboratory (FNAL), Batavia, USA is a proton-antiproton $p\bar{p}$ collider that started its first colliding beam operation in 1989. During a data-taking period from 1992 to 1996 (Run I), the Tevatron experiments CDF and DØ each collected about 125 pb^{-1} of $p\bar{p}$ collision data at a $\sqrt{s}$ of 1.8 TeV, leading to the discovery of the top quark and the measurement of its mass, a precision measurement of the mass of the W boson, detailed analysis of gauge boson couplings, studies of jet production and vastly improved limits on new phenomena, such as leptoquarks and supersymmetric particles, among many other accomplishments.

After a break of about five years, during which the accelerator and the experiments have undergone significant upgrades, the second phase of data taking, called Run II, started in 2001. The Tevatron is expected to deliver between 4 fb^{-1} and 9 fb^{-1} by the year 2009.

The accelerator operates now at a $\sqrt{s}$ of 1.96 TeV with a bunch crossing of 396 ns. The main collider ring has a circumference of about 6 km. The accelerated protons collide with antiprotons, moving in the opposite direction in the same synchrotron ring. The collisions take place in two interaction regions which are surrounded by the two detectors CDF and DØ.

The Tevatron ring is only the last part of a cascade of pre-accelerators at Fermilab as schematically illustrated in Fig. 2.1. The protons used in the collisions are extracted from negatively charged hydrogen ions. The ions are accelerated to 750 keV by a Cockroft-Walton accelerator and injected into a 165 m long linear accelerator which boosts their energy to 400 MeV. The ions are then stripped off their electrons as they pass through a sheet of graphite and are injected into the Booster, a synchrotron which brings their energy to 8 GeV.

Protons from the Booster are sent to the Main Injector, where they are further accelerated

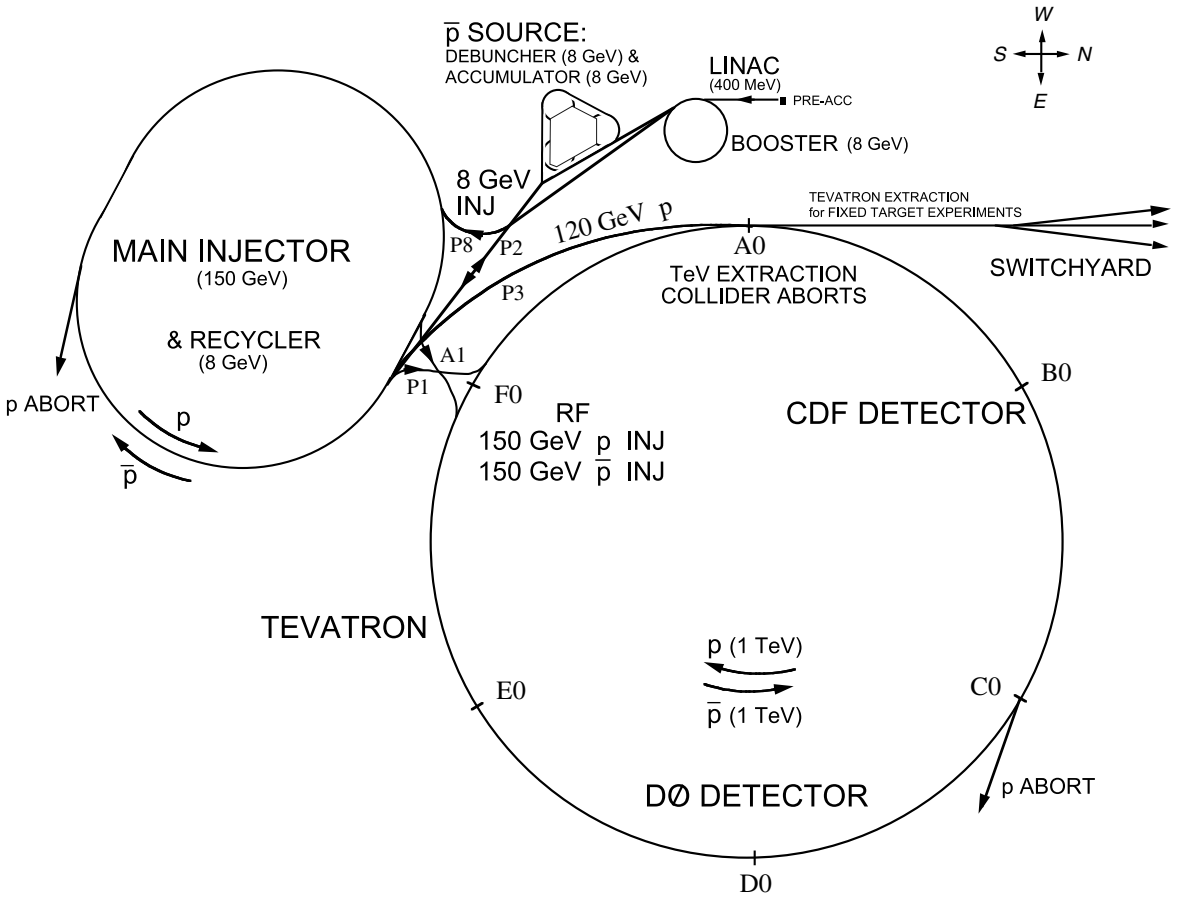

Figure 2.1: The accelerator facilities at *Fermilab* with the Tevatron and the two multi-purpose detectors CDF and DØ.

to 150 GeV. Antiprotons used in the collisions are collected from the interaction products of a portion of the 120 GeV proton beam incident on a Nickel-Copper target. The collision energy is chosen such that the energy spectrum of the emerging antiprotons has its maximum at about 8 GeV. On average, around 50 000 protons are necessary to produce one antiproton in the required energy range. The Tevatron complex is designed in a way that new antiprotons can be produced in parallel to collisions taking place in the main Tevatron ring. The produced antiprotons are cooled and debunched in the Debuncher and Accumulator, and once the number of antiprotons is sufficiently large they are passed to the Main Injector where they are accelerated to 150 GeV for transfer to the Tevatron. Once the protons and antiprotons are injected into the Tevatron, they are accelerated to their final energy of 980 GeV before colliding at the centre of the CDF and DØ detector.

Protons and antiprotons are stored in bunches, with 36 bunches separated by 396 nsec. The 36 bunches in the proton and anti-proton beam are organised into three super-bunches, with a 2 μs gap between each super-bunch. Figure 2.2 shows the integrated luminosity per week and the total integrated luminosity accumulated in Run II from May 2001 until November 2005.

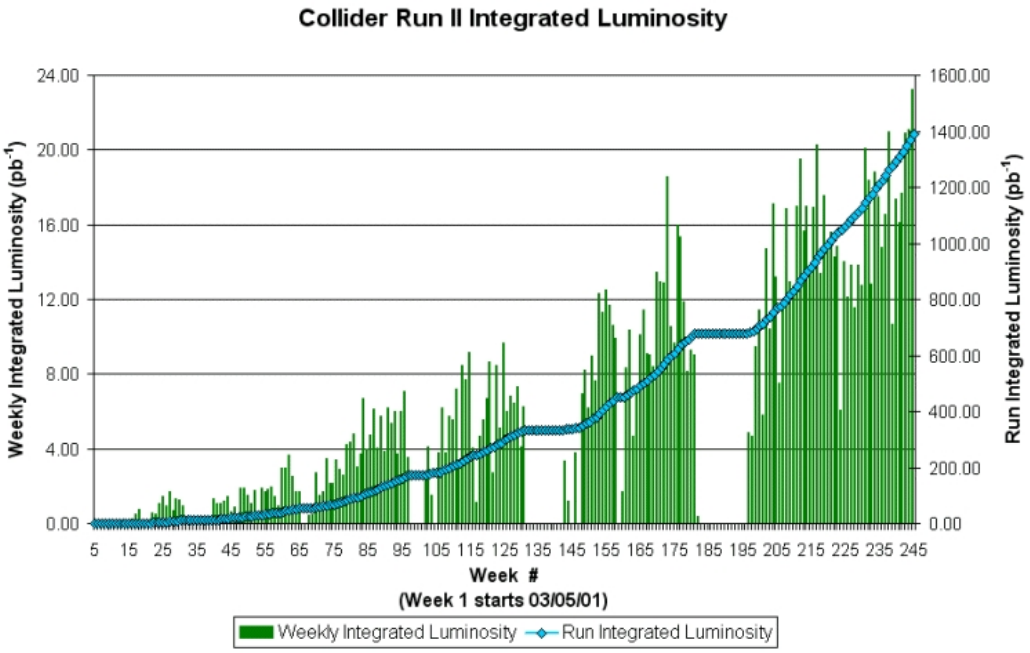

Figure 2.2: The integrated luminosity per week and total integrated luminosity for Run II from May 2001 until November 2005 in pb^{-1}.

The **Large Hadron Collider LHC** at CERN is a proton-proton pp collider with $\sqrt{s} = 14$ TeV. The two superconducting rings are located in the old LEP tunnel with a circumference of 27 km. Figure 2.3 shows the general layout of the LHC. The collider has two high luminosity experiments, ATLAS and CMS, aiming at a peak luminosity of 10^{34} $\mathrm{cm}^{-2}\mathrm{s}^{-1}$. In addition to these high luminosity experiments, there are further interaction regions for the experiments LHCb and ALICE. LHCb is a dedicated B physics experiment and is described in detail in section 2.5.

The high beam intensities at LHC implied by the design luminosity of 10^{34} $\mathrm{cm}^{-2}\mathrm{s}^{-1}$ exclude the use of one antiproton beam and one common vacuum and magnet system for both circulating beams as it is done at Tevatron. Due to space limitations in the LHC tunnel a twin-bore magnet solution is chosen, where the magnet coils surrounding the two beam channels are firmly embodied inside the same iron yoke. The whole superconducting magnet with field of 8.3 T is placed inside a cryostat, containing a bath of superfluid helium with temperature of 1.9 K. Protons are being injected into LHC by the Super Proton Synchroton (SPS) at an energy of 450 GeV.

The time between two consecutive bunch crossing at LHC is 25 ns, which sets the basic clock frequency for the detector electronics to 40 MHz. As a consequence of the filling procedure, however, some bunches are empty.

The first pp collisions are scheduled for September 2007. During the first years after startup, the LHC will run at a lower luminosity of 10^{33} $\mathrm{cm}^{-2}\mathrm{s}^{-1}$.

Some of the main machine parameters of LHC and Tevatron are listed in Tab. 2.3.

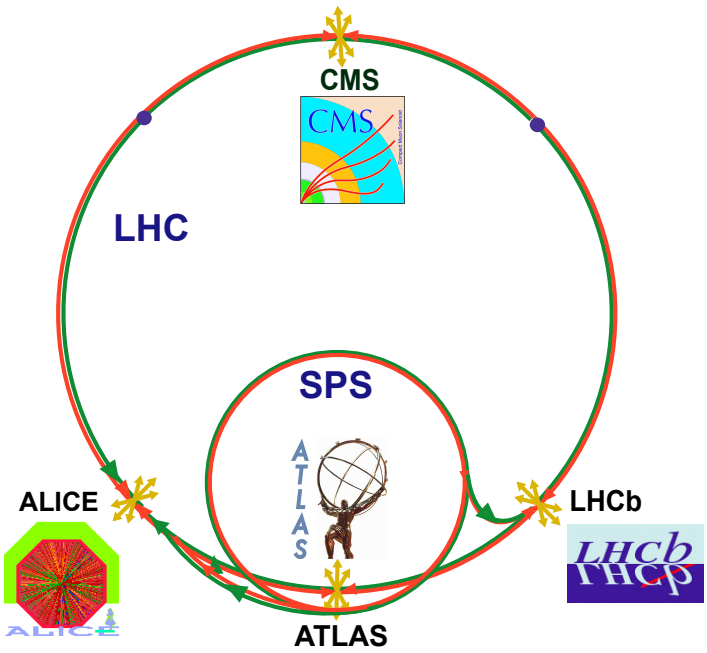

Figure 2.3: The LHC complex with its four experiments.

2.4 The DØ Experiment at Tevatron

The DØ detector was constructed in the late 1980's and early 1990's [11] and operated from 1992 to 1996 in Run I of the Tevatron. It was then significantly upgraded [12, 13] to handle the increased luminosities of Run II.

The DØ detector is a large multi-purpose detector and has been built to measure precisely muons, electrons, jets and missing transverse energy. To serve this purpose, the detector consists of three major subsystems. At the core of the detector, a magnetized tracking system records precisely the angles of charged particles and measures their transverse momenta. A hermetic, finely grained Uranium and Liquid Argon calorimeter measures the energy of electromagnetic and hadronic showers, and a muon spectrometer detects and measures the momenta of escaping muons. Figure 2.4 shows a schematic overview of the detector.

2.4.1 Central Tracking System

The central tracking system is surrounded by a solenoid magnet which provides a nearly uniform (magnetic) field of $B = 2$ T parallel to the beam axis. Charged particles produced in the collision are bent around the field lines. The radius r of the curvature allows for a measurement of the transverse momentum through:

$$p_T[\text{GeV}] = 0.3 \cdot r[\text{m}] \cdot B[\text{T}]\,. \tag{2.3}$$

The superconducting solenoid magnet is designed to optimize the transverse momentum resolution, $\Delta p_T/p_T$, and track recognition. It is 2.73 m in length and 1.42 m in diameter, corresponding to maximum of 0.9 radiation lengths, X_0, for a given pseudo-rapidity and

Table 2.3: Some machine parameters of Tevatron and LHC.

	Tevatron	LHC
Colliding particles	$p\bar{p}$	pp
Circumference (km)	6.28	27
Maximum beam energy (TeV)	1.0	7.0
Injection energy (GeV)	150	450
Luminosity (10^{30} cm^{-2}s^{-1})	210	10^4
Time between collisions (ns)	396	25
Bunch length (cm)	38	7.5
Trans. bunch size σ_{xy} (μm)	22	16
Particles per bunch (p)	$2.6 \cdot 10^{11}$	10^{11}
Particles per bunch ($\bar{p}$)	$4.2 \cdot 10^{10}$	-
Bunches per beam	36	2808

provides a 2 T magnetic field with a field homogeneity of 0.5 %. It operates at 10 K, the current is 4820 A and the stored energy is 5.6 MJ.

Closest to the beam pipe itself is the Silicon Microstrip Tracker (SMT), which allows for the precision measurements, that are crucial for an accurate measurement of impact parameter and the identification of secondary vertices. The SMT is described more in detail in section 2.7. Surrounding the SMT is the Central Fibre Tracker (CFT), consisting of 16 layers of scintillating fibre. The CFT extends to a radius of 50 cm, giving a lever arm long enough to provide sufficient transverse momentum resolution. The DØ central tracking system is illustrated in Fig. 2.5.

The Central Fibre Tracker [12, 13] consists of 835 μm diameter scintillating fibres mounted on eight concentric support cylinders and occupies the radial space from 20 to 52 cm from the centre of the beam pipe. The two innermost cylinders are 1.66 m long, the outer six cylinders are 2.52 m long. Each cylinder supports one double layer of fibres oriented along the beam direction and a second double layer at a stereo angle of alternating $+3^\circ$ and -3°. The two layers of fibres are offset by half a fibre width to ensure full acceptance coverage. The small fibre diameter gives the CFT a cluster resolution of about 100 μm per double layer.

Light production in the fibres is a multi-step process. When a charged particle traverses one of the fibres, the scintillator emits light at $\lambda = 340$ nm through a rapid fluorescence decay. A wave-shifting dye efficiently absorbs the light well at $\lambda = 340$ nm and emits at $\lambda = 530$ nm. The light is then transmitted by total internal reflection to the end of the scintillating fibre, where it is transferred through an optical connection to clear fibre waveguides of identical diameter, which are 7.8 to 11.9 m long. The light is only observed from one end of each scintillating fibre. The opposite end of the scintillating fibres is sputtered with an aluminium coating that provides a reflectivity of 85 to 90%. The clear fibre waveguides carry the scintillation light to visible light photon counters (VLPCs) which convert it into an electronic pulse.

The visible light photon counters are situated in a liquid Helium cryostat and operate at a temperature of 9 K. They detect photons with a quantum efficiency of 85% and provide

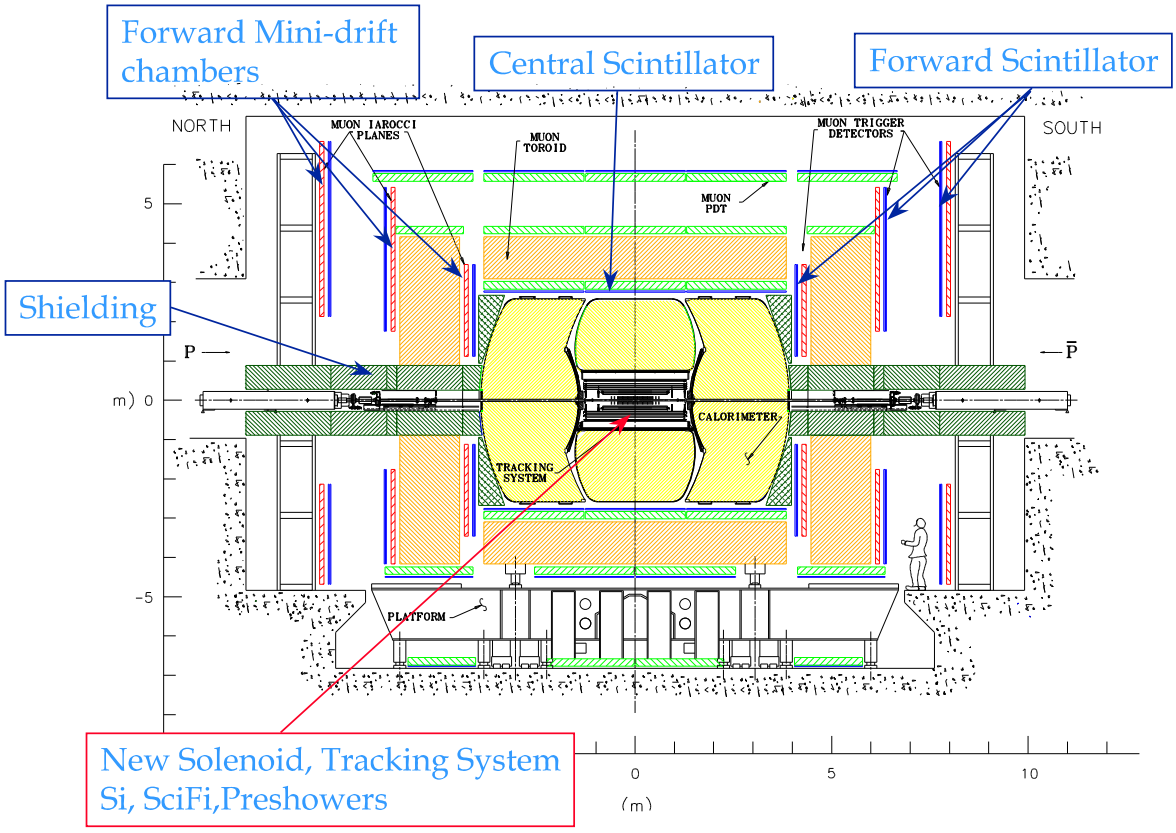

Figure 2.4: Cross-sectional view of the DØ Run II detector.

about 30k- 60k electrons per photon. A minimum ionizing particle creates an average of eight photo-electrons per layer, depending on the angle between the scintillating fibre and the particle trajectory.

2.4.2 Calorimeter System

The task of the calorimeter system is to measure the energy of particles by inducing them to produce electromagnetic and hadronic showers. Inert passive layers of dense material in which the shower begins are followed by active layers, where the surviving fraction of the shower energy is sampled through ionization.

The Liquid Argon calorimeter is designed to provide precise energy measurement, to assist in the identification of electrons, photons, taus and jets and to establish the transverse energy balance in an event. The device is also sensitive to MIPs and therefore can serve to identify muons. The calorimeter itself is unchanged from Run I. However, there is significantly more material in front of the calorimeter (2-4 X_0, depending on η) and faster readout electronics were build to cope with the reduced bunch crossing time from Run I to Run II.

The Liquid Argon calorimeter is subdivided into the central calorimeter (CC) covering roughly $|\eta_{det}| < 1$ and two end calorimeters (EC) extending the coverage to $|\eta_{det}| \approx 4$. Each

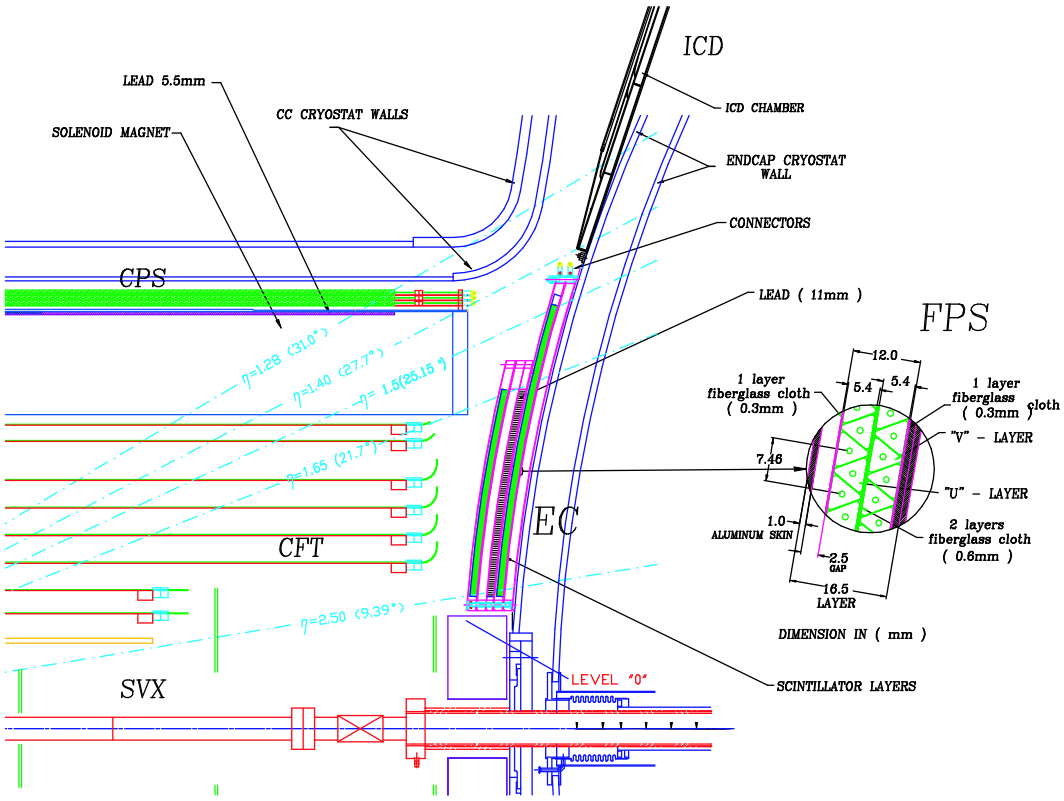

Figure 2.5: Cross-sectional view of the DØ tracking and preshower system.

calorimeter contains an electromagnetic section closest to the interaction region followed by fine grained and coarse grained hadronic sections whose module size increases with the distance from the interaction region. The active medium for all calorimeters is liquid Argon, and each of the three calorimeters is located within a cryostat that maintains the temperature at approximately 80 K. In order to achieve the same energy response for electromagnetic and hadronic particles, $e/h \approx 1$ (compensating calorimeter), different absorber plates are used at different locations. The e/π ratio was measured for charged pions in test beam data of Run I and the calorimeter was found to be nearly compensating, with $1 < e/\pi < 1.05$ for energies above 30 GeV. The electromagnetic sections (EM) use thin (3 or 4 mm) plates made from nearly pure depleted Uranium. The fine hadronic sections are made from 6 mm thick Uranium-Niobium alloy. The coarse hadronic modules contain 46.5 mm thick plates of either Copper (in the CC) or stainless steel (in the EC).

The elements are combined in a basic unit, a calorimeter cell, which contains the absorber plates, the active medium and a Copper readout pad, laminated to G10 and covered in resistive epoxy, for collecting the ionization. An electric field is established by grounding the absorber plates and holding the resistive surface of the pad at typically 1.6 kV. The electron drift time across the 2.3 mm gap is approximately 450 ns. Several such pads are connected together in depth to form a readout cell.

2.4.3 Muon System

The outermost part of the DØ detector is the muon system (Figs. 2.6 and 2.7). The detection of muons relies on their penetration power through material. Several meters of high-density material absorb almost all electrons and hadrons.

Any charged particle that penetrates this material is defined to be a muon. The DØ muon detection system serves to identify and trigger on these muons and measure their momenta and charge.

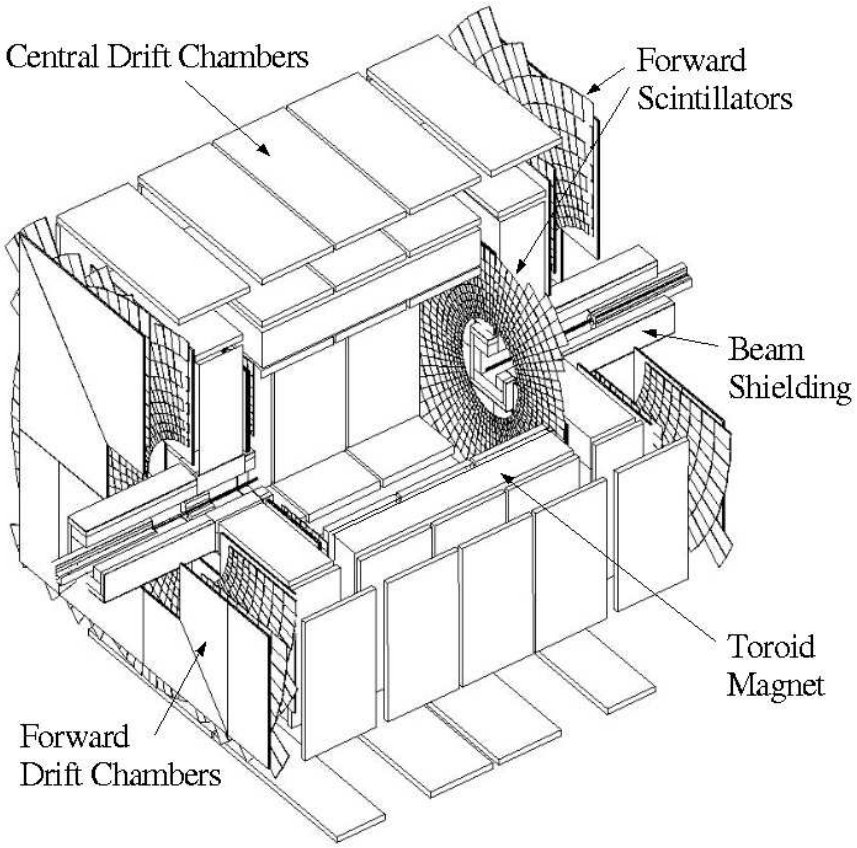

Figure 2.6: A cut-away view of the muon system.

The muon spectrometer consists of three subsystem: Proportional Drift Tubes (PDTs), Mini Drift Tubes (MDTs) and scintillation counters. The PDTs cover the region of $|\eta_{det}| < 1.0$ and the planes of MDTs extend the muon detection to $|\eta_{det}| = 2.0$. The scintillator counters are used for triggering and for the rejection of cosmic and beam related muons. Toroidal magnets with a field of 1.8 T and a special shielding complete the muon system. Each subsystem has three layers, called A, B, and C. The A layer is located between the calorimeter and the iron of the toroid magnet, the B and C layers are located outside of the iron. In the region directly below the calorimeter, only partial coverage by muon detectors is possible since the support structure for the DØ detector and readout electronics is located in this region.

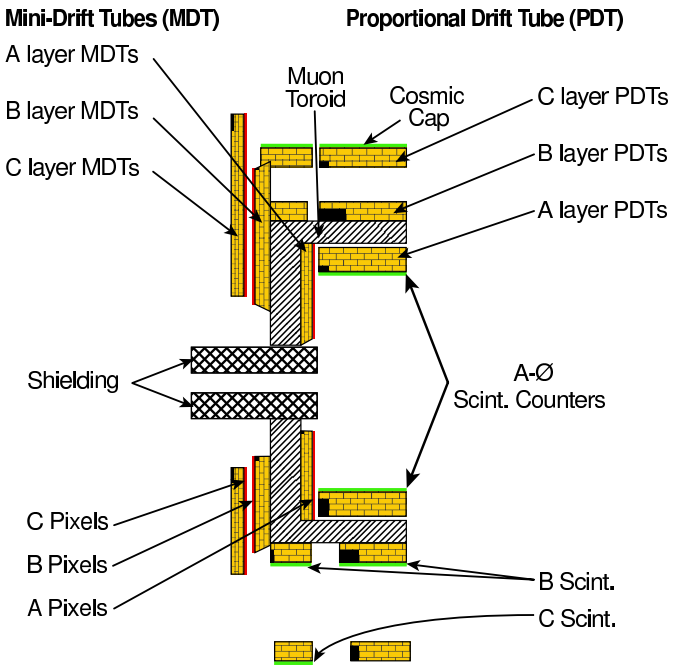

Figure 2.7: Side view of the DØ muon system with Proportional Drift Tubes (PDTs), Mini Drift Tubes (MDTs), scintillator counters, toroid magnet and shielding.

The thickness of the detector is in the range of 5-9 interaction lengths in the calorimeter, and in the range of 7-9 interaction lengths in the iron. This results in a most probable value for the energy loss of a muon in the calorimeter of 1.6 GeV, and about 1.7 GeV in the iron. The momentum measurement is corrected for this energy loss.

Finally, there is dedicated shielding around the beam pipe before entering the DØ detector. The shielding reduces the large beam-related background processes such as:

- Scattered proton and antiproton fragments that interact with the end of the calorimeter or with the beam pipe produce background in the central and forward A layer.

- Proton and antiproton fragments, mostly muons from the decays of pions created by proton and antiproton interactions upstream of the detector, interacting with the low beta quadrupole magnets produce hits in the B and C layers of the forward system.

- Beam halo interactions affect both the central and the forward muon system.

The shielding consists of layers of iron, polyethylene and lead in a steel structure, surrounding the beam pipe and the low beta quadrupole magnets. Iron is used as a hadronic and electromagnetic absorber, polyethylene is a good absorber for neutrons due to its high hydrogen content, and lead is used to absorb gamma rays.

2.5 The LHCb Experiment at LHC

The LHCb experiment [14] is a dedicated B physics experiment that is set up as a forward spectrometer for pp collisions at $\sqrt{s} = 14$ TeV at the LHC. The experiment is designed to study CP violation with unprecedented high precision in as many reconstructed B decay channels as possible and to investigate rare B decays to search and constrain new physics. Figure 2.8 shows the experimental setup of the LHCb detector.

Since the two B hadrons resulting from pp collisions are correlated in rapidity they can be detected in the same forward or backward cone. The acceptance of LHCb can then be defined through the polar angle with respect to the beam axis. With a relatively small angular coverage of 10 to 300 (250) mrad in the bending (non-bending) plane of the magnet, a large acceptance for B hadrons is achieved. The correlation of the $b\bar{b}$ pair is shown in Fig. 2.9 as function of polar angle (a) and rapidity (b). About 15% of all produced $b\bar{b}$ events fall into the acceptance of LHCb having the decay products of at least one B in the detector.

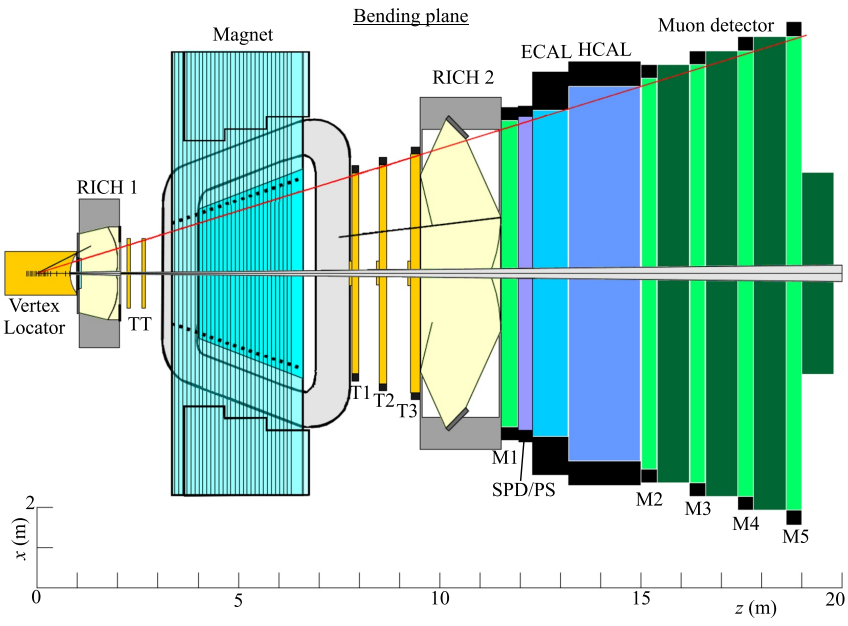

Figure 2.8: The LHCb setup with the different subdetector components shown in the horizontal (bending) plane. The detector has an overall length of 20 m and its overall dimensions are roughly 6 m $\times$ 5 m $\times$ 20 m.

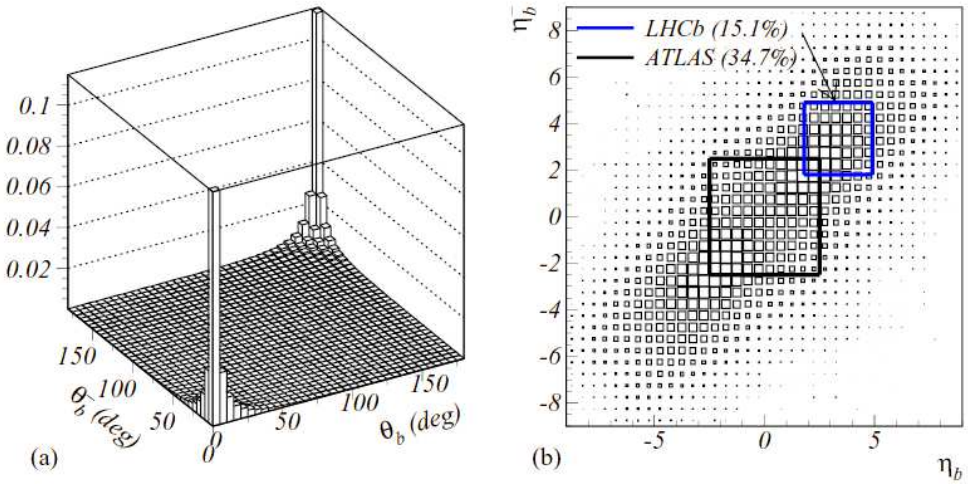

Figure 2.9: The angular correlation of the two b-hadrons is shown in terms of (a) the polar angle and (b) the pseudo-rapidity.

The luminosity at the LHCb interaction point is reduced to 2×10^{32} cm^{-2}s^{-1} by defocusing the beam with quadrupole magnets. This luminosity working point was found by optimizing obtained B yields with respect to fake background rates and the ability to distinguish single collisions from multiple collisions within the same bunch (pile-up). The moderate luminosity 2×10^{32} cm^{-2}s^{-1} results in an average number of inelastic interactions per bunch crossing of $< n >= 0.53$. The left graph of Fig. 2.10 shows the probabilities for single and multiple pp collisions as function of luminosity. The optimal luminosity is close to the point where the single interaction probability reaches a maximum. The right side of Fig. 2.10 indicates the expected number of $b\bar{b}$ events. Around the chosen luminosity point the $b\bar{b}$ rate without additional pile-up is highest. Other benefits of a moderate luminosity are lower particle multiplicities, making the particle reconstruction simpler and a lower radiation environment to which detectors and their associated readout electronics are exposed to.

The LHCb experiment comprises a vertex detector (Velo), a tracking system, two Ring Imaging Cherenkov (RICH) counters, a calorimeter system consisting of pre-shower detector, electromagnetic and hadronic calorimeters and a muon system. In the following the various LHCb subdetectors are described:

2.5.1 Vertex, Magnet and Tracking System

Charged particle tracking is provided by the Velo [15] and four tracking detector stations: one station in front of (TT) and three stations (T1-T3) behind the dipole magnet. The charged particles are bent in the B field of the magnet having a total integrated field of $\int Bdl = 4$ Tm with a main component along the z-axis. The particle momentum is measured from the deflection of the trajectory as the particles traverse the magnet. The difference between the track slope in the Velo and the track slope in the stations after the dipole magnet is inversely proportional to the particle's momentum.

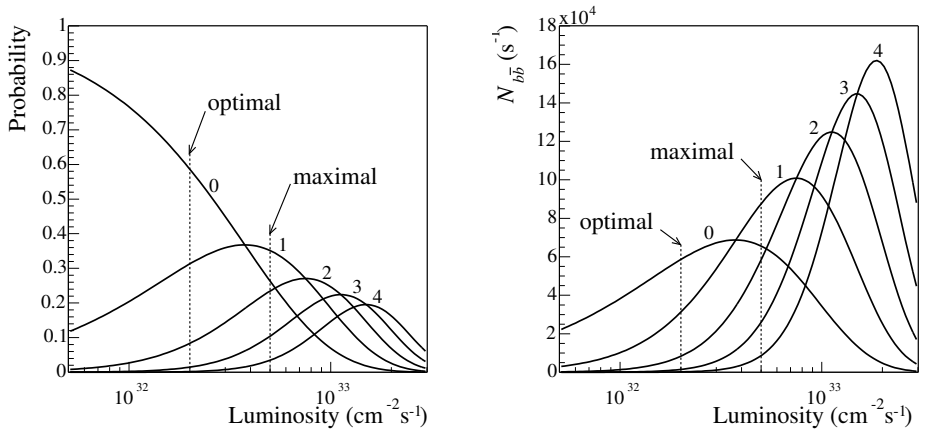

Figure 2.10: Left: Probability of single and multiple collisions per bunch crossing as function of luminosity. Right: The $b\bar{b}$ event rate with up to four pile-up events.

The Velo is installed around the interaction point and consists of 21 stations of silicon strip detectors along the beam line as can bee seen in Fig. 2.11 (a). The task of the Velo is the precise measurement of track coordinates as close a possible to the beam axis, such that primary and secondary vertices can be well separated. The impact parameter resolution of the Velo is expected to be 30 μm.

Two types of 220 μm thin silicon sensors are used in the Velo: one measures the r coordinate with circular strips centered around the beam axis (see Fig. 2.11(b)), the other measures the ϕ coordinate with straight radial strips. The r strips of the Velo detector provide a measurement of the $r-z$ projection, such that all forward going tracks with high impact parameter with respect to the primary vertex can easily be identified and exploited by the trigger system, before a full three-dimensional reconstruction of those tracks starts.

In order to provide a close measurement point to the primary vertex and thus to reduce the extrapolation errors, the sensitive area of the Velo sensors starts only 8 mm away from the beam axis. This proximity requirement implies that the sensors have to be retractable from the beam axis during beam injection, otherwise beam induced radiation background during injection would severely damage the detector. The retraction is achieved by separating the detector stations into two halves that can be moved away from the beam in the horizontal direction.

The Velo detector is separated from the primary beam vacuum by a thin aluminium foil which shields also the electronics against RF pickup. The foil has a complex corrugated shape that is optimized to minimize the amount of dead material for particles coming from the primary vertex. The whole vertex detector is then housed in a vacuum vessel with 10^{-4} mbar. Forward going particles leave the Velo through a thin wall exit window, to which the LHCb beam pipe is attached.

The LHCb tracking detectors have to provide a momentum resolution $\delta p/p$ below half a percent to give a typical B mass resolution below 15 MeV/c^2. Beside the Velo, further tracking detectors are the TT station that is placed in front of the magnet and three stations T1-T3 after the magnet. The TT station and the inner part of the three stations T1-T3 are

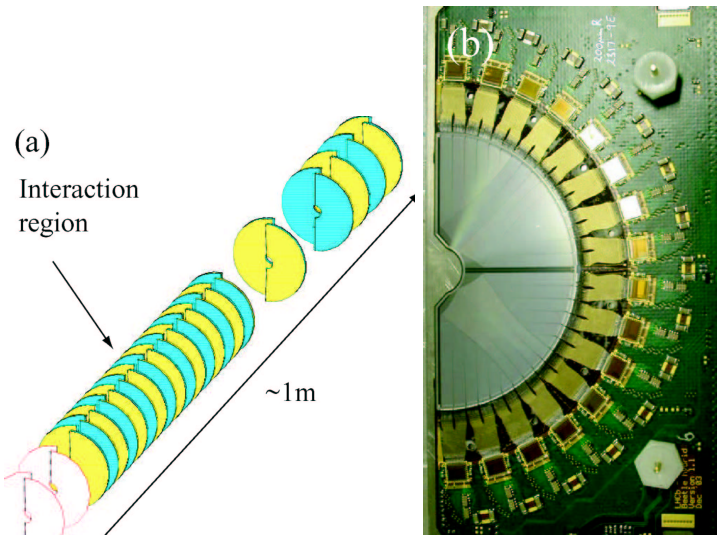

Figure 2.11: Left: Layout of the silicon detectors in the Velo, along the beam axis. Right: Photograph of one of the r-silicon sensors.

constructed from silicon microstrip sensors to face high particle occupancies. Their design and layout is further described in section 2.7. The outer part of the T1-T3 stations is equipped with 5 mm straw tubes, arranged in four double layers.

2.5.2 Particle Identification System

In LHCb charged hadrons over a large momentum range between 1 to 100 GeV/c must be identified. In particular, a $\pi - K$ separation is indispensable in the selection of many B decay channels. For instance, particle identification information that can be provided by a Cerenkov detector is essential to distinguish $B_s^0 \to D_s^{\mp} K^{\pm}$ decays from $B_s^0 \to D_s^{\mp} \pi^{\pm}$ decays.

At LHCb there is a strong correlation between the polar angle and momentum of the tracks. At wide angles the momentum spectrum is softer. The Ring Imaging Cerenkov detector (RICH) system [16] of LHCb is therefore divided into two subsystems. Low momentum particles between 1-60 GeV/c are identified by RICH1. It combines silica aerogel and C_4F_{10} fluorocarbon gas radiators with a polar acceptance from 25 to 300 mrad and is directly sealed to the vacuum vessel of the Velo detector using the beampipe as part of the gas enclosure. A magnetic fringe field between Velo and TT station exists in order to determine the momenta of particle in the Level-1 trigger. Therefore, strong constraints on the RICH1 mechanical design, in particular on an efficient shielding of the photodetectors are imposed. High momentum particles (up to 100 GeV/c) are identified by RICH2 located downstream of the magnet and tracking stations. The used radiator is CF_4.

It is expected to reach a 3σ separation between pions and kaons over a momentum between 3 and 80 GeV/c.

2.5.3 Calorimeters

The calorimeters [17] provides information on the identification of electrons, hadrons and neutral particles and is used in the earliest trigger stage. It is divided into three components: A pre-shower detector, an electromagnetic calorimeter and a hadronic calorimeter. All three subsystems are divided into two halves that can be retracted horizontally from the beam.

The pre-shower is made from a 1.5 cm thick lead converter, that is sandwiched between two scintillating planes with 16k scintillating pads. The granularity of the pads is adapted to the particle flux by choosing three different pad sizes ranging from 40.4×40.4 mm^2 in the inner region to 121.2×121.2 mm^2 in the outer region.

The electromagnetic calorimeter is built out of 3300 shashlik-type detector modules with 4 mm thick scintillating tiles alternated with 2 mm thick lead sheets. Scintillating light is captured and transported via wavelength shifting (WLS) fibers running through holes in the module to photomultipliers located at the module's end. The total depth of the electromagnetic calorimeter is 25 X_0 and the energy resolution is $10\%/\sqrt{E} \oplus 1.5\%$. Similar to the pre-shower detector, the electromagnetic calorimeter is also divided into three regions with different cell sizes.

The hadron calorimeter is a an iron/scintillator calorimeter with tile geometry. The scintillator tiles are 4 mm thick alternated with 16 mm thick iron. The scintillation light is guided through WLS fibers at the edge of the modules to photomultiplers for further readout. The total depth of the hadronic calorimeter is 5.6 hadronic interaction length, λ_I, and the energy resolution for hadrons is $80\%/\sqrt{E} \oplus 10\%$.

2.5.4 Muon System

The muons system [18] allows the reconstruction of muons for offline analysis and provides information for muon identification at high p_t at the earliest trigger level. The system consists of five stations. The first station M1 is located in front of the calorimeters, while the other four stations M2-M5 behind the calorimeter are separated by iron filters. All detectors are instrumented with multiwire proportional chambers (MWPC's), except for the innermost part of the first station, that will be equipped with triple-GEM detectors due to the higher rate. Each muon station is divided into four regions with different readout pad granularity adjusted to the particle flux.

The system achieves a typical muon identification of 94% while keeping the pion misidentification below 1%. In the trigger algorithm high p_t muons are found by a fast and standalone track reconstruction selecting particles traversing through all five stations. A 20% p_t-resolution is obtained by estimating the muon momentum from the slope between the first two muon stations assuming that the particle originated from the interaction point.

2.6 Triggers for B Physics

The most appealing features of hadron machines as tools to study B physics is their very high cross section for $b\bar{b}$ production and the access to all sorts of b-flavored hadrons. On the other hand, b events are a small fraction (0.1%-0.5%) of the overall event rate and the challenge is to devise a trigger system selective enough to suppress 'minimum bias events' by several orders of magnitude. Moreover, at higher luminosity the B event rate is several kHz making the isolation of the B decays from the even larger background rate more challenging.

An obvious choice for a mode specific trigger for $b\bar{b}$ events is to exploit the long lifetime of the B meson and its decay vertex, which is displaced from the main interaction vertex. Before silicon vertex detectors were fully established at hadron colliders an interesting trigger concept for B events was studied for SSC and LHC in the beginning of the 90ies, but never realized in a detector. It was based on optical discriminators [19] to trigger on charged particles originating from a detached vertex. The optical trigger consisted of a shell of transparent material centered on the interaction axis. The index of refraction would be chosen such that Cherenkov light emitted in the shell by charged particles originating from the interaction point is refracted out, whereas some of the light emitted by particles not pointing to the interaction point is trapped in the shell by internal reflection and emerges at the edges for further readout.

Nowadays, the identification of a secondary vertex is done with high resolution silicon detectors which are routinely and successfully operated at high energy experiments and may serve as B triggers depending on the application. Silicon detectors are described more in detail in section 2.7.

The classical B trigger for hadron colliders however, was used already at UA1 as a working horse [20] for B physics and is extensively being exploited at Tevatron for B lifetime, mixing and mass measurements. It relies on the selection of B events based on semi-leptonic or multi-leptonic B decays. In general, leptons from B decays tend to have a harder p_t spectrum than from minimum bias events or charm decays, such that a first background suppression can in principle be achieved with a lepton trigger at a certain p_t threshold. However, the cross section for b production is steeply falling with p_t and drops – for example at Tevatron – by about two orders of magnitude between a b-quark p_t of 8 GeV/c and 25 GeV/c. It is therefore desirable to set trigger thresholds as low as possible in transverse momentum to exploit the rapidly falling cross section. At low momenta the preferred choice for the leptons to trigger on are muons, since they are easily identified at the trigger level. Low momentum electrons are more difficult to identify since bremsstrahlung and photon conversion processes in a massive detector will introduce background.

Lepton triggers are either constructed as single-lepton triggers from semi-leptonic B decays or as di-lepton or multi-lepton triggers. At high enough luminosities such as at Tevatron single-muon triggers at lower p_t thresholds are dominated by background due to decays in flight and punch-through particles misidentified as muons. Their rates are high, such that p_t thresholds have to be adjusted or triggers pre-scaled during data taking. Single-muon triggers are also often augmented with other trigger elements, such as displaced tracks or vertices.

About 1% of all B mesons decay into J/ψ modes, which can be picked up by an inclusive di-lepton trigger. The J/ψ's from B decays have a falling transverse momentum spectrum of up to 20 GeV/c at Tevatron. With a di-lepton trigger one can collect large and clean samples of B decays into J/ψ with relatively low trigger thresholds. Those samples that are collected with di-muon triggers at Tevatron are used for lifetime and mass measurements, while the single muon events are exploited for mixing analysis. The big advantage of lepton triggers is that they are free from any bias due to the life time of the B meson. Such a bias can not be avoided with triggers that are selective on life time and/or decay length information.

Finally it should be noted that CDF has designed a special two-track trigger [21] that is successfully operating for B physics. The trigger requires two tracks of opposite charge with a large opening angle that are displaced from the vertex, i.e., using silicon vertex detector information. It was designed to mainly collect two-body hadronic B decays, such as $B_d^0 \rightarrow$

$\pi^+\pi^-$. The trigger has also been proven to collect multi-body B decays, such as $B_s^0 \to D_s^-\pi^+$ with a loser requirement on the opening angle and tighter impact parameter. The trigger allows to collect large samples of hadronic B decays, requiring up to 20% of the level 1 bandwidth.

In the following the trigger concepts for the DØ and LHCb experiments are described in more detail. The B trigger capabilities of Atlas and CMS are mentioned as well.

2.6.1 The DØ Trigger System

At the Tevatron, an input bunch crossing rate of 1.7 MHz must be reduced to a final data taking rate of 50 Hz, a limit that is presently given by the DØ offline reconstruction capabilities. The DØ trigger system is a three-tiered pipelined system; each tier examines the event in more detail than lower tiers and restricts the input rate of events to higher tiers.

Level 1 Trigger:
Collisions occur at a rate of 1.7 MHz. The first trigger stage (Level 1 or L1) has a pipeline, which allows to take a decision within 4.2 μs, and has a trigger accept rate of about 2 kHz. The trigger algorithm is carried out in a framework of field programmable gate arrays (FPGAs), which receive as input simple objects created in the luminosity monitor, the calorimeter and the muon system.

Level 2 Trigger:
In the second stage (Level 2 or L2), hardware engines associated with specific subdetectors process information which is then used in a global processor to determine correlations between different detectors, e.g. to match tracks and leptons. Level 2 has an accept rate of 1 kHz with a maximum dead-time of 5%, and a maximal latency of 100 μs.

Figure 2.12 illustrates the design of the DØ Level 1 and Level 2 trigger system. The components currently being commissioned are represented as hatched boxes.

Level 3 Trigger:
The third stage (Level 3 or L3) uses a collection of approximately 100 PC farm nodes to perform a partial reconstruction of the event and take a trigger decision using the full event information (complete physics objects as well as their correlations). The nominal 1 kHz input rate is reduced to a rate of 50 Hz at which data are recorded for offline analyses. The online version of the event reconstruction is optimized to fit into the timing requirements ($\sim$50 ms) at Level 3.

When an event passes the Level 2 decision, the data from the roughly 80 readout crates are sent to a single farm node, where the event reconstruction takes place. Filters can select events based on physics quantities. A single farm node handles events at a rate of 10-20 Hz. Events that pass a Level 3 filter are sent from the farm node to a collector, which in turn sends the events over Gbit/s optical Ethernet to the Feynman Computing Center, where the events are written to tape for offline analysis.

DØ Trigger Limitations:
The DØ detector has a strong capability to identify leptons over a wide range in rapidity. Consequently, the main B physics trigger at DØ are single- and di-muon triggers. The majority of the data relevant for B physics analysis are based on semi-leptonic B decays and are selected by single-muon triggers, requiring on L1 a track with at least $p_t \approx 3$ GeV/c

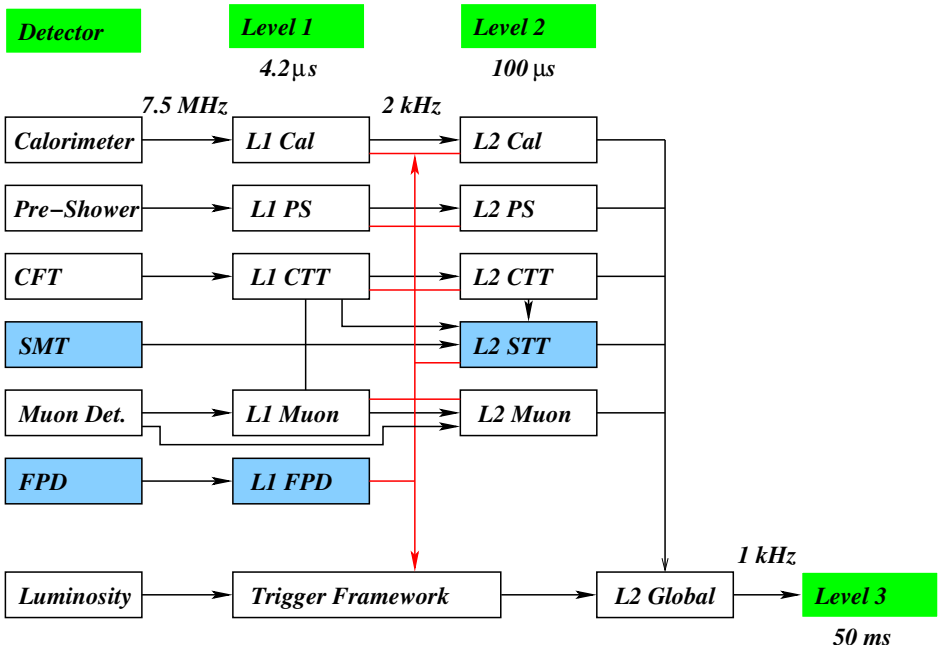

Figure 2.12: The design of the DØ Level 1 and Level 2 trigger system.

between $|\eta| < 1.6$ in the central region and $p_t \approx 2$ GeV/c in the forward region $1.6 < |\eta| < 2.0$. The track is matched at an octant level to a tight muon trigger scintillator hit. Pre-scale factors for the unbiased single-muon triggers are already effective at 2×10^{31} cm^{-2}s^{-1}. At a luminosity of 5×10^{31} cm^{-2}s^{-1} the L1-rate is 135 Hz or about 5% of the nominal L1 accept rate. At L2 a tighter requirement on the muon scintillator and PDT wire information is imposed. This reduces the rate marginally by 13%. At this stage the muon purity is essentially 100% with roughly equal fractions from charm and bottom decays. At L3 B events are selected with several algorithms that either require muon-only triggers with different p_t thresholds of 3, 4 and 5 GeV/c or additional tracks or tracks with significant impact parameters.

The di-muon triggers are generally very clean and robust against increased luminosity. However, they will be pre-scaled as well starting at a luminosity of 1×10^{32} cm^{-2}s^{-1}. The current main di-muon trigger is based on the muon system only, taking advantage of the full η-coverage of the muon system. The trigger covers several analysis that are statistics limited like the $B_s^0 \to \mu^+\mu^-$ search and has a present L3 rate of about 2 Hz.

Currently, DØ has an approximate bandwidth limit at L3 of writing 50 Hz to tape. About 10% of this rate is allocated to B physics. With this limitation the single-muon triggers have to be pre-scaled or effectively forced to run at increased muon p_t threshold. Pre-scale factors or p_t thresholds directly affect the size of the B samples hurting the B physics program severely as luminosity at Tevatron is increasing. Therefore, a proposal has been made to add another 50 Hz of L3 bandwidth mainly devoted to B physics [22] to be able to maximize the number of B physics events for the future luminosity increase at Tevatron.

2.6.2 The LHCb Trigger System

Although the LHC bunch crossing frequency is 40 MHz, the interaction rate that is visible in the LHCb detector is expected to be 16 MHz. This is partially due to empty bunches and partially due to elastic collisions that leave no track in the detector. The main strategy of the LHCb trigger [23] is to look for two signatures of B decays: the large mass of the B mesons produce decay products with high p_t, and the long B lifetime produces tracks from decay particles with high impact parameter with respect to the primary interaction vertex. The trigger is divided into three distinct levels L0, L1 and a higher level trigger HLT which process an increasing amount of information from the subdetectors.

L0 Trigger:
The purpose of L0 is to reduce the initial 16 MHz of inelastic collision to about 1.0 MHz while keeping a high efficiency for B events. The L0 is implemented as a hardware trigger residing at the detectors and has a latency of 4 μs. The 160 bunch crossings that occurred during that decision time are stored in analog pipeline memory cells. The maximum output rate for L0 is fixed to 1.1 MHz, which requires to transmit the accepted events within 900 ns to the L1 buffers. Out of the 1.1 MHz trigger rate about 100 kHz are $b\bar{b}$ events and 800 kHz $c\bar{c}$ events.

The L0 system uses information from the pile-up veto, the calorimeter and the muon systems, that is then collected in the L0 decision unit to provide the trigger decision. The subsystem information used for L0 has two distinct components: high p_t objects such as muons, electrons or hadrons from decay products of a massive B meson on the one hand and global event variables on the other hand such as number of interactions and multiplicities. The latter information is provided by the pile-up veto that consists of two silicon stations containing r sensors located upstream of the interaction point. Its purpose is to reject events with multiple collisions by histogramming the $r - z$ tracks from the hits in the two stations and calculating the corresponding z vertex information. The calorimeter trigger selects high E_t clusters of 2×2 cells in the electromagnetic and hadronic calorimeter. Clusters in the electromagnetic calorimeter are further identified as either electron, photon or π^0 using the pre-shower information. Further global event variables are the sum of the E_t in the calorimeter and the charged particle multiplicities in the pre-shower detectors. For the muon trigger a stand-alone track reconstruction from hits in the muon chambers is implemented achieving a p_t resolution of about 20% to select the two highest p_t muons for triggering.

L1 Trigger:
The L1 trigger is the first of the two software trigger systems that is running on a CPU farm with about 2000 processors shared with the HLT. The trigger exploits the long life time of the B mesons in addition to the large B meson mass as a further signature to improve the purity of the selected events. In its original design it uses information from the L0 decision unit, the Velo and the TT and has a latency of about 1 ms and an output rate of 40 kHz. So-called 2D tracks in the Velo are reconstructed using the r-sensor information only. The majority of the tracks are pointing backward to the primary interaction point which can be reconstructed with a resolution of about 60 μm along the beam line. Tracks with a high impact parameter in the range of 0.15–3 mm, and the ones matched with a high-p_t L0 muon are reconstructed in three dimensions. About eight 3D tracks are found per event and linked to hits in the TT station to measure their momenta. The magnetic field distribution allows a

momentum resolution of 20-40% depending on the momentum. The final L1 trigger decision is made by combining the information for two tracks with significant impact parameter and large p_t into a L1-variable. A simultaneous cut is applied on the logarithmic sum of the p_t and of the impact parameter significance.

A just recent development at LHCb is the implementation of very high performance router/switches for the data acquisition system at affordable costs. It allows the readout of the entire detector with full precision at the Level-0 accept rate of 1 MHz in one single data stream. The added feature of the 1 MHz detector readout makes the L1 trigger as a distinct item more or less obsolete, since L1 and higher trigger level can now be unified, residing on the same hardware system using all data available for processing.

Higher Level Trigger HLT:
The HLT performs a full reconstruction of the event, allowing events of interest to be selected in a similar fashion than in the offline selection. The latency is 50 ms and the output rate has recently been increased to 2 kHz, since the event size of approximately 25 kB is relatively small. There are four different streams in the HLT:

- **Exclusive** B stream with a rate of 200 Hz. This stream is reserved and will be tuned for the core physics program of about ten exclusively reconstructed B decays. It will also include sidebands and control channels.

- **Di-muon stream** with a rate of 600 Hz. Unbiased di-muons with a mass above 2.5 GeV/c^2 are selected and used for measurements of the lifetime uncertainties.

- D^* **stream** with a rate of 300 Hz. This allows to measure the particle identification efficiency and misidentification rates. It can also be used to exploit CP violation in the D system and for charm physics.

- **Inclusive** B with a rate of 900 Hz. This sample contains events with one high-p_t muon with large impact parameter. It will be used for systematic studies of trigger and tracking and to control detector calibration.

Typical trigger efficiencies after L0, L1 and HLT of LHCb are about 70% for $B \to J/\psi X$ decays, 30-40% for hadronic decays such as $B \to \pi\pi$ and about 35% for radiative decays such as $B_d^0 \to K^*\gamma$.

2.6.3 Triggering on B's at ATLAS and CMS

The Atlas and CMS experiments at LHC are both detectors with different acceptance, instantaneous luminosity, and physics objectives that are not equivalent to the LHCb situation. In particular, Atlas and CMS have a much broader physics program covering high p_t phenomena. A B physics program is foreseen, at least during the initial low luminosity phase of 10^{33} cm$^{-2}s^{-1}$ and eventually later at the nominal design luminosity of 10^{34} cm$^{-2}s^{-1}$. Even at the initial luminosity both experiments have to deal with important pile-up effects with almost five inelastic pp interactions in a bunch crossing leading to additional constraints for the B selection in the trigger. The triggering strategy for B physics is then based on single-muon and di-muon triggers at the lowest possible p_t threshold while still keeping the output trigger rate compatible with the acceptance rate of the next level. The trigger thresholds will

Table 2.4: Overview of trigger levels for the DØ experiment and the three LHC experiments. The numbers for Atlas and CMS refer to the inital low luminosity phase of 2×10^{33} cm^{-2}s^{-1}.

	Atlas	CMS	LHCb	DØ
Input rate 1^{st} trigger level	40 MHz	40 MHz	16 MHz	1.7 MHz
Output rate 1^{st} trigger level	75 kHz	50 kHz	1 MHz	2 kHz
Output rate HLT	200 Hz	100 Hz	2000 Hz	50(+50) Hz
Dedicated for B physics	10-15 Hz	10-15 Hz	$>$ 1.5 kHz	5(+20?) Hz

be flexible depending on the allocated bandwidth given to B physics in the experiment. A minimal muon transverse momentum of $p_t > 6-8$ GeV/c (Atlas) and $p_t > 14$ GeV/c (CMS) in the pseudorapidity range of the experiments for single muon triggers has to be applied. The di-muon triggers could run at $p_t > 3-7$ GeV/c.

The total output rates of the Atlas and CMS L1 triggers are 75 kHz and 50 kHz, respectively. In case of CMS the events are directly fed into the HLT, while Atlas employs a second trigger level which further suppresses the rate into the HLT to 2 kHz. At L2, the Atlas trigger searches for objects around the triggered muon such as a second muon, or e/γ objects in the calorimter region of interest. The HLT of Atlas is called event filter and provides full access to the events, including vertex information. Thus, exclusive B decays can then be reconstructed using mass and decay length information based on off-line algorithms. The HLT at CMS has a limited time budget and has to restrict B reconstruction to regions of interest around the muon or use only a reduced number of hits/tracks for reconstruction.

The trigger efficiencies for B decay modes at Atlas and CMS will be smaller than at LHCb. This is particularly true for radiative B decays with a photon in the final state and for hadronic channels. In cases of B decays with two muons in the final state the di-muon triggers at Atlas and CMS are rather safe and may work at higher luminosity such that potentially large signal yields over the years can be obtained.

In general, the B physics performance of Atlas and CMS will strongly depend on the allocated B physics trigger rate at all trigger levels. The trigger strategies of Atlas and CMS on single and di-muon events have to be handled rather flexible and threshold adjustments are very likely to occur. The presently foreseen total output rates of the higher level trigger are 200 Hz for Atlas and about 100 Hz for CMS. It is planned to dedicate about 10-15 Hz of this available bandwidth to B physics.

Table 2.4 gives a final summary of the trigger rates for the Atlas, CMS and LHCb experiments at LHC as well as for the DØ experiment at Tevatron. In case of DØ the numbers after the bandwidth upgrade are added.

2.7 Silicon Detectors

Initially, the development of position-sensitive semiconductor detectors was driven by the need of particle physics experiments investigating charm decays in the early 1980ies. Already at that time the experiments required devices with good position resolution of less than 100 μm and capable of working at high rates. The introduction of silicon strip detectors produced with planar technology by Kemmer [24] marked the start to a revolution in experimental

techniques that included the development of low-noise and low-power analog microelectronics for the readout of silicon detectors. Since then silicon detectors started to become common in many fixed target experiments. The first silicon detector in a challenging hadron collider environment was successfully used by CDF [25] in Run I.

Today, one of the key detector elements for a successful B physics program is a high resolution silicon vertex detector either with sensitive strips or pixels. The distinctive feature of B decays is that their life time is longer than for mesons consisting of light quarks only. With a high resolution vertex detector, B decays can then be separated by measuring tracks that are detached from the primary vertex.

A typical silicon strip detector consists of an array of long p^+n diodes on a silicon substrate that is between 250 to 500 μm thick. Typical dimensions for the pitch of the strips are 25-200 μm. The detector itself is reverse-biased to create a region depleted of electron and holes carriers over the entire substrate depth. Under irradiation of an incident particle electron-hole pairs are generated and separated by the electric field. In case of an p^+n detector the holes will move towards the segmented p^+ junction while electrons drift to the backside n^+ electrode. During the process of charge separation, the carriers will induce charges on the electrodes leading to a small current pulse that is amplified for measurement. Silicon sensors can be either single-sided with one segmented side only, or double-sided where both sides are segmented and then read out.

Two examples of typical silicon microstrip detectors that are designed for vertexing and tracking applications in particle physics are the DØ silicon microstrip tracker and the LHCb silicon tracker. Common to both detector designs is the consideration of minimal mass, i.e., to have as little material as possible in the active area. This requires the use of light-weight support materials for structural applications and a good thermal performance to remove the generated heat in the front-end chips. Both detector designs are now described in more detail.

2.7.1 The DØ Silicon Microstrip Tracker

General Layout

The DØ silicon microstrip tracker (SMT) was designed to allow for precise vertexing and three-dimensional track reconstruction over a large acceptance for higher p_t tracks up to $\eta \approx 3$. The detector consists of six barrel modules with silicon sensors parallel to the beam line, as well as twelve so-called F-disks and four sets of so-called H-disks with silion normal to the beam line. An isometric view of the SMT is shown in Fig. 2.13. The main motivation for choosing such a design was the extended $p\bar{p}$ interaction region of $\sigma \approx 25$ cm which determines the length of the device in z. With a long interaction region, it is difficult to deploy detectors such that the tracks are generally perpendicular to detector surfaces for all η. This led to a design using barrel modules interspersed with disks in the center and assemblies of disks in the forward and backward regions. The barrel detectors measure primarily the r - ϕ coordinate and the disk detectors measure r - z as well as r - ϕ. Thus, vertices for high η particles are reconstructed in three dimensions by the disks, and vertices of particles at small values of η are measured in the barrel.

Each of the six barrels consists of four main silicon layers with each layer having two staggered and overlapping sub-layers, as seen in Fig. 2.14. A radial offset of 6 mm allows adequate clearance for cooling channels and routing of the cables between sub-layers, hence reducing the inter-barrel spacing.

	Barrels	F-Disks	H-Disks
#Channels	387 072	258 048	147 456
Sensors	s/d sided	double sided	single sided
Stereo	$0°, 2°, 90°$	$\pm 15°$	$\pm 7.5°$
#Modules	432	144	96 pairs
Si area	1.3 m^2	0.4 m^2	1.3 m^2
Inner radius	2.7 cm	2.6 cm	9.5 cm
Outer radius	9.4 cm	10.5 cm	26 cm
Maximal $\|z\|$	38.4 cm	54.8 cm	120 cm

Table 2.5: Specifications of the SMT, where "s,d" means single, double sided.

The outer barrels have single-sided and double-sided 2° stereo ladders. The four inner barrels have double-sided 90° stereo and double-sided 2° stereo ladders. Each barrel is capped at high $|z|$ with a F-disk of twelve double sided wedge detectors. In the far forward and backward regions, a unit consisting of three F-disks and two external large-diameter H-disks provides tracking at $|\eta_{det}| < 3.0$. The F-disks are made of twelve wedges of double sided stereo detectors. The H-disks are made of 24 pairs of single-sided detectors glued back to back. In total there are 792,576 readout channels in the silicon detector. Table 2.5 summarizes relevant SMT design parameters.

The barrel modules and the F-disks are supported by a double-walled carbon-fiber half structure, which aids in maintaining precise alignment. The half cylinder locates the silicon detector relative to the scintillating fiber tracker and serves as support for cabling and cooling channels.

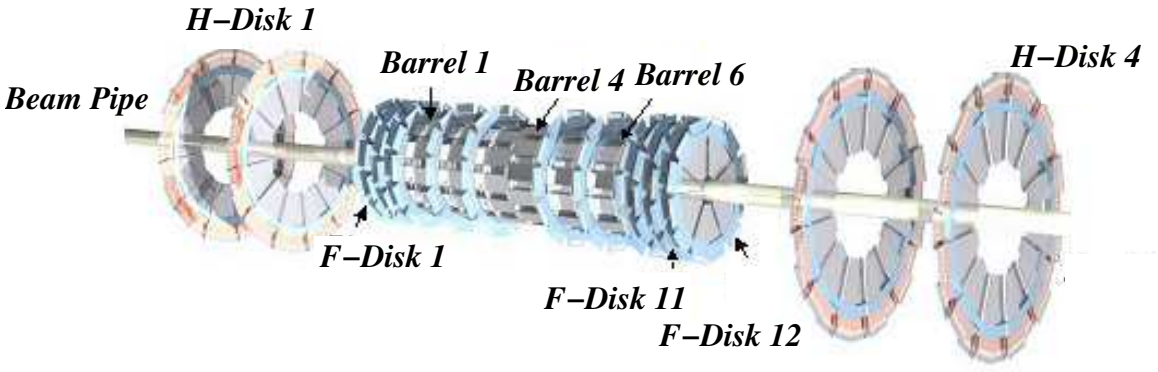

Figure 2.13: Isometric view of the DØ SMT.

The DØ SMT Module Design

The silicon modules or ladders are readout by using the SVX II chip, which is fabricated in a 1.2 μm CMOS technology. The chip features a pre-amplifier, 32-cell deep analog pipeline and a 8-bit ADC with sparsified readout. The SVX II chips and other passive components are mounted on a kapton based flex circuit (high density interconnect HDI), which - in the case of double-sided silicon - is wrapped around one silicon edge to serve both ladder surfaces.

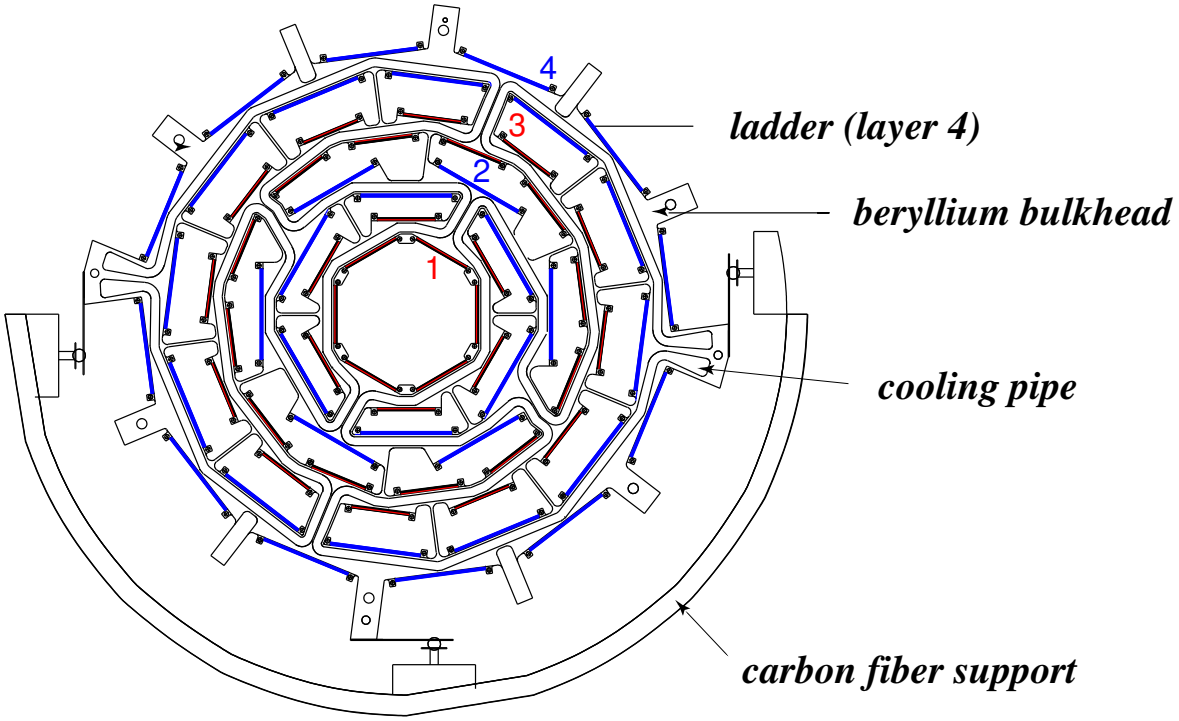

Figure 2.14: Cross section of the SMT barrel structure.

The HDIs provide for electrical connections at the ladder edges and help to reduce the gaps between the barrels to a minimum. The flexible long tail of the HDI allows the routing of the cable to the outer side of the barrel region. The four layers of the barrel and disk/barrel geometry of the silicon detector required nine different types of HDIs carrying 3, 6, 8 or 9 chips and various lengths.

The considerations of minimal mass, precise alignment and adequate thermal performance of the silicon detectors in barrels and disks have led to a design of the basic detector unit with 400 μm thick beryllium substrates glued to the silicon sensors. The basic layout of a SMT silicon ladder is shown in Fig. 2.15. The positioning of the ladder in the barrel is achieved by precisely machined notches in the beryllium substrate that fit into posts at the bulkhead surface. The HDIs are laminated onto the beryllium such that a low thermal impedance path is provided to remove the heat of the chips efficiently. In addition to the beryllium pieces, two rails, each consisting of Rohacell sandwiched in carbon/boron fiber skins are glued to the silicon ladder. The rail material has been chosen to match the thermal expansion coefficient of silicon.

The DØ SMT was assembled in the years 1998-2000 and commissioned in 2001/2002. Details on the production and testing of the DØ SMT can be found in [26].

Radiation Limitation

The DØ SMT was designed and its components tested, for an expected lifetime assuming a delivered integrated luminosity at Tevatron of 2 fb^{-1}, corresponding to a fluence of about 1.3×10^{13} 1 MeV n/cm^2 in the innermost layer. An irradiation study was carried out [27]

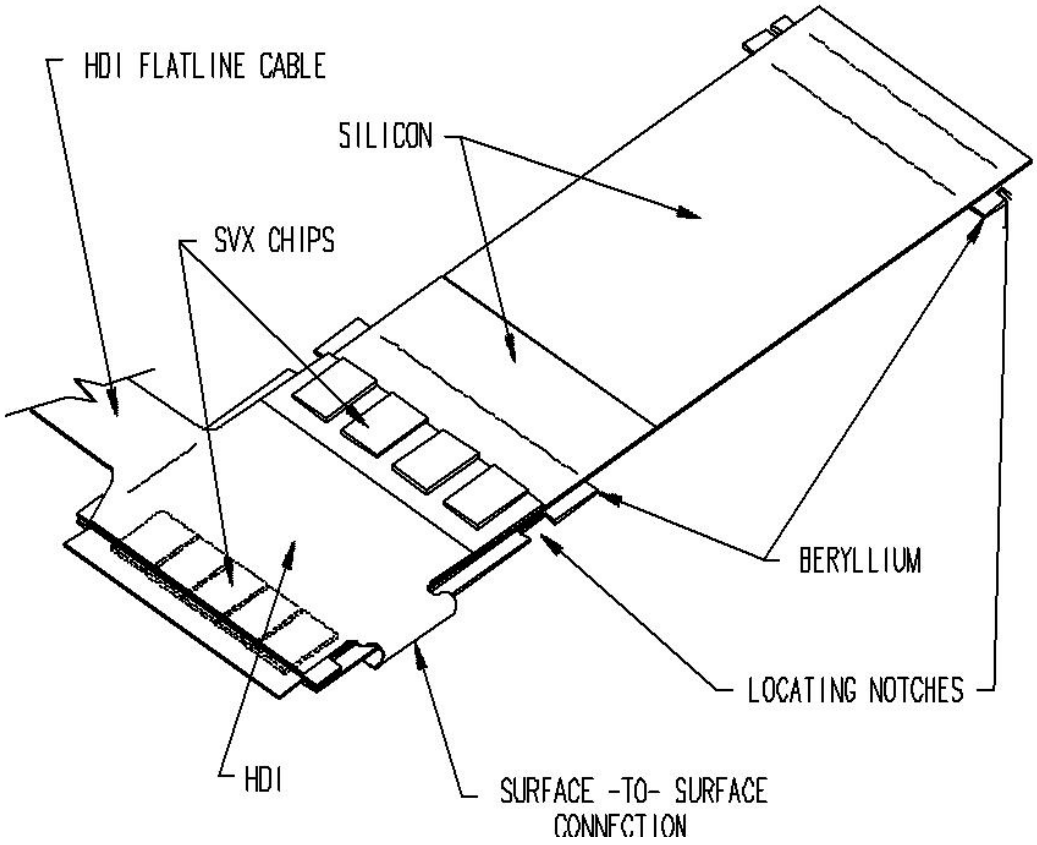

Figure 2.15: Schematic sketch of a DØ SMT barrel ladder.

aiming for predicting the lifetime of the silicon detector. In this investigation Run II spare production silicon ladders were used identical to the ones installed in the experiment. The irradiation was performed with 8 GeV protons from the Fermilab Booster up to a total fluence of 3.7×10^{13} 1 MeV n/cm^2, almost a factor 3 higher than the expected dose in Run IIa. The charge collection studies on irradiated modules revealed that the double-sided 90° silicon ladders exhibited increased sensitivity to radiation, which is likely caused by the additional PECVD insulation in between the double-metal layers. Moreover, increased noise due to micro-discharge effects has been observed and will introduce an upper limit on the total operating bias voltage. According to best estimates, it is believed that the useful lifetime of the inner layer is limited to around 3-4 fb^{-1}.

Layer 0

The extended running period of the Tevatron accelerator until 2009 makes an upgrade of the existing DØ silicon detector mandatory. A new improved design aiming for a complete replacement of the existing DØ silicon detector was therefore worked out [28] in 2002 and started production in 2003, when the director of Fermilab, Michael Witherell, terminated the silicon detector upgrade project in October 2003.

After the cancelation of the full silicon detector replacement, it was immediately decided

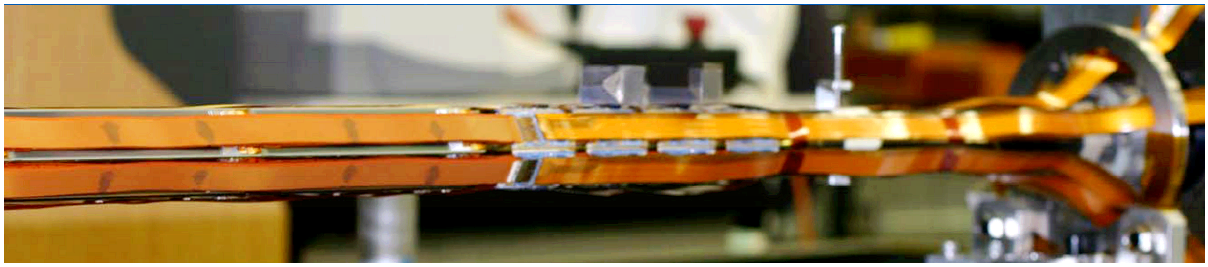

Figure 2.16: Photograph of the DØ layer 0 detector.

at DØ to construct a new inner silicon layer for insertion into the existing detector. This new detection layer (Layer 0) should mitigate the efficiency loss due to increased radiation damage in the existing inner silicon detector layer.

The technical design of this Layer 0 is documented in Ref. [29]. The new detection layer is designed to fit inside the existing DØ SMT and will utilize much of the existing infrastructure as well as the new electronics and readout designed for the canceled Run IIb detector. The new Layer 0 must be able to slide over a beam pipe and has to fit in a tightly constraint space between 30.5 mm and 44 mm in diameter. A photograph of the Layer 0 detector is shown in Fig. 2.16. In total 48 single-sided sensors with a readout pitch of 71 μm in the inner radius and 81 μm in the outer radius are used. The hybrids are located outside of the active volume and are connected to the sensors with fine-pitch interconnect cables. The Layer 0 detector has been now fully assembled and will be installed in the existing DØ detector in April 2006.

2.7.2 The LHCb Silicon Tracker

The charged particle tracking at LHCb relies on the Velo and four dedicated tracking detector stations: one station in front of and three behind the dipole magnet. The first tracking station (TT) in front of the magnet consists entirely of silicon microstrip detectors. Using the magnetic fringe field in front of the TT, this detector is part of the L1 trigger, which selects events containing particles with high p_t. In case of the other three tracking stations only the inner part (IT) is employing silicon strip devices while the outer area is covered with straw tubes. This split solution allows to better cope with the high particle densities around the beam pipe, thus keeping the occupancies tolerable.

Simulation studies have shown [30] that the track momentum resolution in LHCb is dominated by multiple scattering over a wide range of momenta. This results in a spatial resolution requirement, which can be met by silicon strip detectors with wide pitch of about 200 μm. Large readout pitch and long strips adapted to the expected hit occupancies are used throughout the Silicon Tracker (IT+TT) in order to reduce the number of readout channels and hence the costs. Due to better robustness against radiation and a simpler module design, the usage of single-sided silicon sensors was chosen. The Silicon Tracker covers a total surface area of 12 m^2 and is segmented in 336 (IT) and 128 (TT) mechanical units with about 270k channels. Some of the parameters can be found in Tab. 2.6.

The TT Station

The TT station situated in front of the magnet consists of four planar detection layers covering

	IT Station	TT Station
#Channels	128 352	143 360
Sensors	single sided	single sided
Stereo	0°, ±5°	0°, ±5°
#Modules	336	128 (half modules)
Si area	4.3 m^2	7.8 m^2

Table 2.6: Some Parameters of the two main components of the LHCb Silicon Tracker.

the entire acceptance between 15 mrad and 300 mrad in the horizontal plane. The active area is approximately 160 cm wide and 130 cm long. The four detection planes are arranged in two groups of two layers each. The first two detection layers have a strip orientation of 0° and +5° with respect to the vertical axis followed by the second group with two layers of strip orientation of -5° and 0°. All silicon sensors are kept in a common light tight, dry and thermally insulating detector housing with an ambient temperature of about 5°C provided by liquid C_6F_{14} cooling. The TT detector box is vertically split into two half stations allowing a retraction from the beam pipe. A half station of the TT detector is shown in the left part of Fig. 2.17.

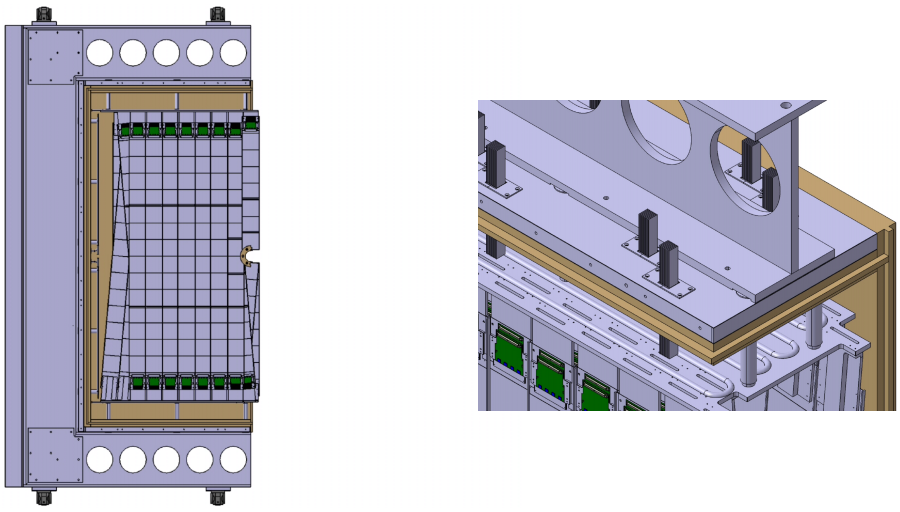

Figure 2.17: Left: The TT half station. Right: Close-up of the module positioning on the cooling plate.

Each detection plane of the TT detector is build out of 150 cm long silicon modules equipped on both ends with readout electronics situated outside the acceptance of the experiment. Each of the four detector planes consists of 14 or 16 silicon modules of full length and two half-length modules above and below the beam pipe. The modules are mounted vertically or close to vertically on cooling balconies into the detector station frame. The cooling balconies are attached to large cooling plates located at the top and bottom of the station. The right part of Fig. 2.17 shows a close-up of the mounted modules in the station.

The basic construction unit during the assembly is a half-length module consisting of seven silicon sensors plus two or three readout hybrids located at the end of the half module.

The sensors and readout hybrids are hold together by two carbon fiber rails that are glued along the sensor and hybrid edges. The seven sensors of a half module are segmented into either a 4-3 or a 4-2-1 readout grouping with maximum active strip length of 36 cm. The half modules with the finer grouping of 4-2-1 are situated around the beam pipe. For the 4-3 (4-2-1) half modules, one (two) flexible interconnect cables on polyimide basis route the silicon analogue signal from the sensors to the readout hybrids. Figure 2.18 shows a drawing of a 4-3 half module. More details to the design and production of the TT detector can be found in Ref. [31].

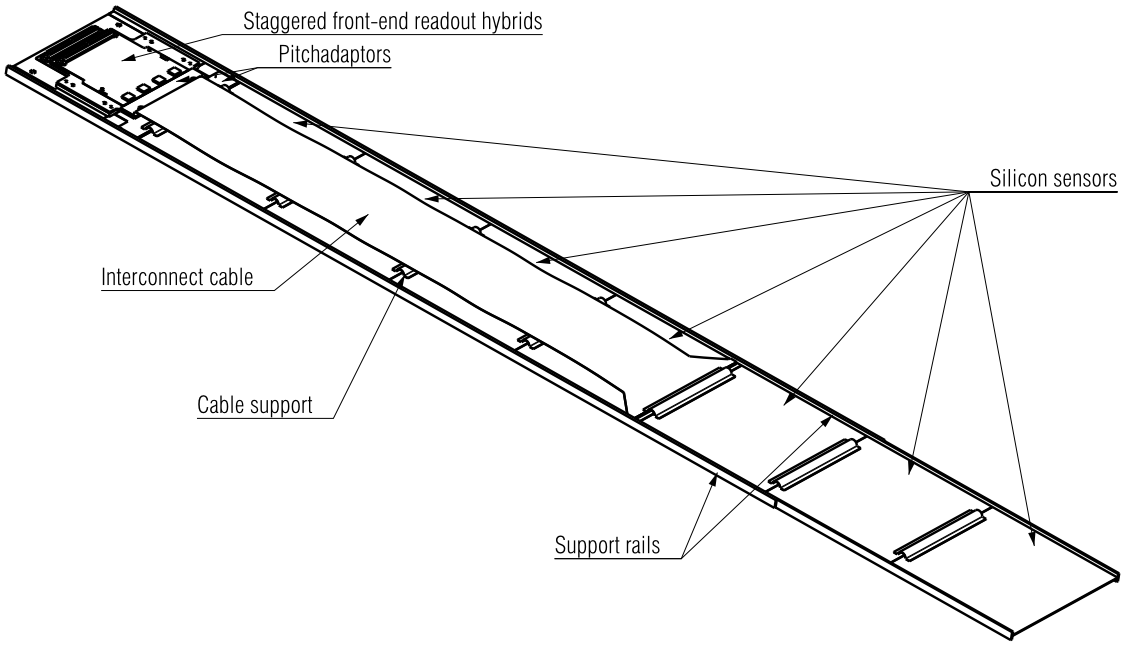

Figure 2.18: Drawing of a 4-3 half module.

The IT Stations

Although the IT covers only few percent of the total area of the tracking stations behind the magnet, about 20% of all tracks are passing through the IT. Due to increased particle fluxes the IT has to cover a larger area in the bending plane of the magnet. Each of the three IT station comprises of four independent detector boxes, which are arranged in a cross-shaped way around the beam pipe as is is shown in the left part of Fig. 2.19. One detector box has four detection layers of silicon planes with strips oriented in 0°, $\pm 5^\circ$ and 0° relative to the vertical axis. The silicon planes are enclosed in a light-tight and thermally insulating housing. As in the TT station, liquid cooling provides an operation temperature of 5°C in the IT detector boxes.

The sensitive planes of one detector box are assembled in a modular fashion. The basic building units are silicon ladders with either 11 cm (one sensor) or 22 cm (two sensors) long and 7.8 cm wide active area. The front-end electronics is located on a hybrid at the end of the ladder. A carbon fiber composite sandwich serves as support for sensors and hybrid. The

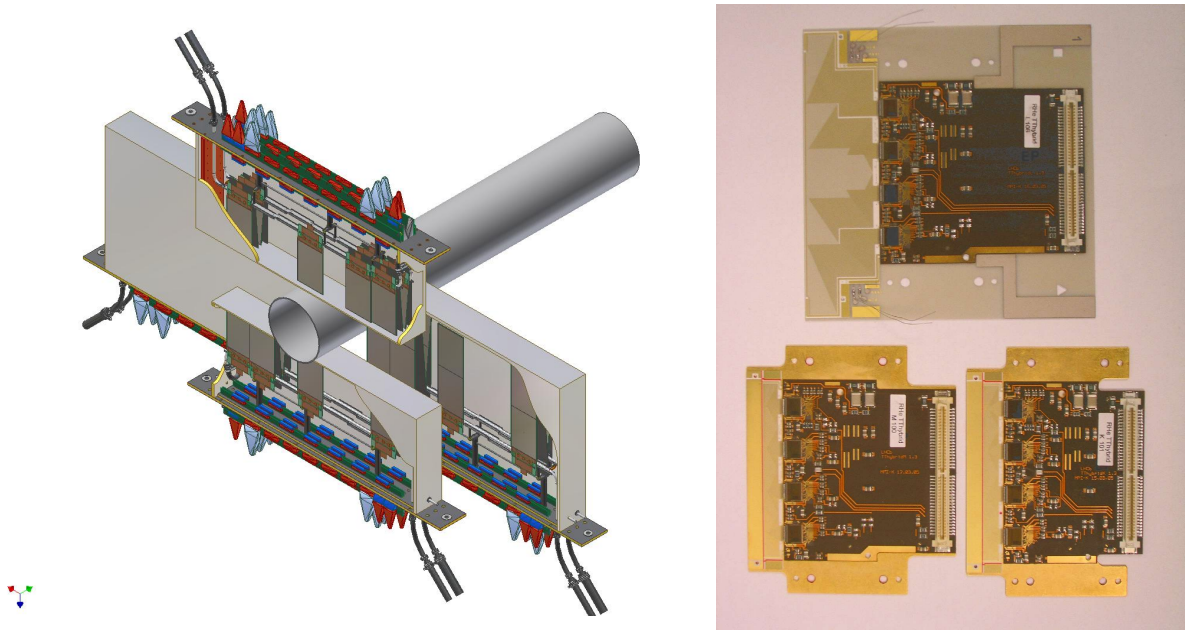

Figure 2.19: Left: An IT station consisting of four detector boxes that are located in a cross-shaped way around the beam pipe. Right: The three different hybrids for the TT modules.

28 ladders per detector box are mounted via small aluminum balconies to cooling rods, which provide the cooling passage for the liquid coolant.

The IT & TT Detector Readout

Each IT & TT detector module is read out by integrated circuits, the Beetle chips [32] that are located on front-end hybrids at the end of the detector modules. Data are then further shipped with low mass cables to service boxes located outside the detector acceptance. The Beetle chip is a 128-channel ASIC device for 40 MHz sampling and multiplexed deadtimeless readout that is manufactured in a 0.25 μm CMOS process and was irradiation tested up to 40 MRad. The chip features for each channel a low-noise charge-sensitive preamplifier, an active CR-RC pulse shaper with a minimum rise time of about 13 ns well below the LHC requirements and an analogue pipeline with a programmable latency of up to 160 sampling times. Upon a trigger the corresponding signals stored in the pipeline are readout within 900 ns.

The hybrid packages for the IT and TT detectors consist of the Beetle chips mounted together with passive electronic components on a flexible printed circuit board (PCB) and of ceramic pitch adapters to match the silicon sensor pitch to the pitch of the Beetle input pads. The complete package is attached to heat spreader substrates that provide a low thermal impedance path to further cooling plates. The right part of Fig. 2.19 shows a photograph of the three hybrid variants for the TT detectors. The hybrid of the lowest level is the largest one and is laminated to a ceramic substrate. The four Beetle chips of the lowest level are connected through a separate pitch adapter to the silicon sensors. The two types of the upper levels are laminated to copper plates and have pitch adapters that connect the Beetle chips to polyimide interconnect cables, which are glued to the pitch adapters. The interconnect

cables route the analogue signals from distant silicon sensors to the hybrid. Copper spacers with a height of 2.5 mm are used for separating the hybrid layers in the hybrid stack. More information to the hybrid design and assembly of IT & TT can be found in Ref. [33].

3 Flavor-Changing Neutral Currents and Rare B Decays

3.1 A brief History of B Physics

The fifth quark in the Standard Model is the bottom- or beauty-quark, in short notation the b-quark. Its existence was established in 1977 at Fermilab [34] in proton-nucleon collisions by the observation of the meson ground state $\Upsilon(1S)$ consisting of a bound b and $\bar{b}$ quarks. The Columbia-Fermilab-Stony Brook collaboration (CFS) at Fermilab observed a large resonant signal of about 770 events on top of a steeply falling background due to Drell-Yan processes of approximately 350 events in the $p + \text{nucleon} \to \mu^+\mu^- X$ reactions. Subsequent e^+e^- annihilation experiments [35] at DESY and Cornell confirmed the observations, determined its mass and width and established later the quantum numbers $J^{PC} = 1^{--}$ of the $b\bar{b}$ bound state nature of the Υ-family of resonances.

The existence of B mesons [36] was first verified in 1980 by the observation of leptons from the decay $\Upsilon(4S)$ into a pair of $B\bar{B}$ mesons with a lepton momentum spectrum expected from B meson semi-leptonic decays. A few years later, charged $B^{\pm}$ and neutral B_d^0 mesons were explicitly reconstructed and their life times measured. The first evidence for particle antiparticle mixing for neutral B mesons came from the hadron collider experiment UA1 [37] in the same sign di-lepton channel in 1987. However, the interpretation of their data was masked by the circumstance that their measurements were not able to distinguish the B_d^0 from the B_s^0 system. Shortly after, the Argus experiment at DESY observed unambiguously [38] the first $B_d^0 - \bar{B}_d^0$ mixing moving indirect mass bounds on the top quark by more than a factor of two. In 1993, the first rare B decay was experimentally established [39] by measuring the exclusive decay rate of the electroweak penguin process $B \to K^*\gamma$ at CLEO. Finally, CP violation has been firmly established in $B_d^0 \to J/\psi K_S$ decays [40] in impressive agreement with CKM predictions.

Since the epochal discovery of the b quark in 1977 many experiments at Cornell, DESY, Fermilab, SLAC, KEK and CERN studied the fundamental properties of b-flavored hadrons in the successive decades. The most extensive studies were done at e^+e^- colliders, but valuable information about B decays has also been obtained at hadron colliders such as the SPS and Tevatron machines.

3.2 Theoretical Framework for B Physics

3.2.1 The CKM Matrix and the Unitarity Triangle

An important target of particle physics is the determination of the unitary 3×3 Cabibbo-Kobayashi-Maskawa (CKM) matrix [41]. The CKM matrix connects the weak eigenstates (d', s', b') and the corresponding mass eigenstates d, s, b:

$$\begin{pmatrix} d' \\ s' \\ b' \end{pmatrix} = \begin{pmatrix} V_{ud} & V_{us} & V_{ub} \\ V_{cd} & V_{cs} & V_{cb} \\ V_{td} & V_{ts} & V_{tb} \end{pmatrix} \begin{pmatrix} d \\ s \\ b \end{pmatrix} = V_{CKM} \begin{pmatrix} d \\ s \\ b \end{pmatrix} \tag{3.4}$$

Many parameterizations of the CKM matrix have been proposed in the literature. The parametrization favored by the Particle Data Group [8] is

$$V_{CKM} = \begin{pmatrix} c_{12}c_{13} & s_{12}c_{13} & s_{13}e^{-i\delta_{13}} \\ -s_{12}c_{23} - c_{12}s_{23}s_{13}e^{i\delta_{13}} & c_{12}c_{23} - s_{12}s_{23}s_{13}e^{i\delta_{13}} & s_{23}c_{13} \\ s_{12}s_{23} - c_{12}c_{23}s_{13}e^{i\delta_{13}} & -c_{12}s_{23} - s_{12}c_{23}s_{13}e^{i\delta_{13}} & c_{23}c_{13} \end{pmatrix}, \tag{3.5}$$

with $c_{ij} = \cos\theta_{ij}$ and $s_{ij} = \sin\theta_{ij}$. The real angles θ_{ij} may be chosen such that $0 \leq \theta_{ij} \leq \pi/2$, and the phase δ_{13} such that $0 \leq \delta_{13} < 2\pi$. In this parametrization the CKM matrix is the product of three complex matrices, of which only one has a non-zero phase. This has the advantage that each of the rotation angles (θ_{12}, θ_{23}, θ_{13}) relates to the mixing of two specific generations. The non-zero value of the phase (δ_{13}) causes CP violation in the weak interactions.

In the standard parametrization the hierarchy of the strengths of the quark transitions mediated through charged current interactions is reflected by:

$$s_{12} = 0.22 \gg s_{23} = \mathcal{O}(10^{-2}) \gg s_{13} = \mathcal{O}(10^{-3}) \tag{3.6}$$

If new parameters λ, A, ρ and η are introduced by imposing the relations

$$\lambda \equiv s_{12} \approx 0.22\,, \qquad A \equiv s_{23}/\lambda^2\,, \qquad \rho + i\eta \equiv s_{13}e^{i\delta_{13}}/A\lambda^3\,. \tag{3.7}$$

the so-called Wolfenstein parametrization of the CKM is derived:

$$V_{CKM} = \begin{pmatrix} 1 - \frac{1}{2}\lambda^2 & \lambda & A\lambda^3(\rho - i\eta) \\ -\lambda & 1 - \frac{1}{2}\lambda^2 & A\lambda^2 \\ A\lambda^3(1 - \rho - i\eta) & -A\lambda^2 & 1 \end{pmatrix} + \mathcal{O}(\lambda^4)\,. \tag{3.8}$$

It corresponds to an expansion in powers of the small quantity $\lambda = 0.22$, and is very useful for phenomenological applications.

The unitarity of the CKM matrix is described by

$$V_{CKM}^\dagger \cdot V_{CKM} = \hat{1} = V_{CKM} \cdot V_{CKM}^\dagger \tag{3.9}$$

leading to a set of nine equations, consisting of three normalization relations and six orthogonality relations. The latter can be represented as six triangles in the complex plane, all having the same area $2A_{CP} = \lambda^6 A^2 \eta = \mathcal{O}(10^{-5})$. However, in only two of them, all three sides are of comparable magnitude $\mathcal{O}(\lambda^3)$, while in the remaining ones, one side is suppressed relative to the others by two or four powers of λ. The orthogonality relations describing the non-squashed triangles are given by:

$$V_{ud}V_{ub}^* + V_{cd}V_{cb}^* + V_{td}V_{tb}^* = 0 \qquad \text{(1st and 3rd column)} \tag{3.10}$$

$$V_{ub}^*V_{tb} + V_{us}^*V_{ts} + V_{ud}^*V_{td} = 0 \qquad \text{(1st and 3rd row)} \tag{3.11}$$

At leading order λ, these relations agree with each other and yield:

$$(\rho + i\,\eta)A\lambda^3 + (-A\lambda^3) + (1 - \rho - i\,\eta)A\lambda^3 = 0. \tag{3.12}$$

3.2.2 FCNC and the GIM Mechanism

In its broadest definition, a flavor-changing neutral current (FCNC) transition is an interaction process that induces via the coupling of a neutral boson a change in the flavor of the quark or the lepton. In the SM, flavor-changing neutral currents (FCNC) are forbidden at lowest order (tree level) but proceed at higher order through loop induced processes. FCNC processes such as particle-antiparticle mixing, certain rare and radiative meson decays and CP violating decays have played an important role in constructing and building the SM. In general FCNC processes are classified as $\Delta F = 1$ transitions where the flavor F of a meson is changed by one unit, or as $\Delta F = 2$ processes, which modify the flavor number by two units, such as meson-antimeson transitions.

The picture of particle physics that was valid about 1970 had only three light quarks u, d and s. The three quarks could mix with each other governed by the Cabibbo [41] angle θ_C. Weak decays of pions, kaons and muons were related through this Cabibbo universality.

As a consequence of this picture large quark transitions $s \rightarrow d$ would occur. These transitions take place because the weak interaction eigenstate d' is an admixture of strong interaction eigenstates d and s:

$$d' = d\cos\theta_C + s\sin\theta_C \tag{3.13}$$

As a result the weak neutral current J^0_{NC} is given by:

$$J^0_{NC} = u\bar{u} + d'\bar{d'} + s'\bar{s'} = u\bar{u} + d\bar{d}\cos^2\theta_C + s\bar{s}\sin^2\theta_C + (s\bar{d} + \bar{s}d)\cos\theta_C\sin\theta_C \tag{3.14}$$

The term $(s\bar{d} + \bar{s}d)\cos\theta_C\sin\theta_C$ is a measure of the size of direct flavor-changing neutral currents in $s \rightarrow d$ transitions and in the three-quark picture not particularly suppressed. This consequence however, was in strong contradiction to experimental observations. The first searches for FCNC were carried out [42] on kaon decays looking for signals from $K^+ \rightarrow \pi^+e^+e^-$ and $K^+ \rightarrow \pi^+\nu\bar{\nu}$ decays already in the years 1964-1970. Very strong upper limits on the branching ratios of the order of 10^{-6} were obtained and caused most people to believe that flavor changing neutral currents did not exist in nature.

In 1970 Glashow, Iliopoulos and Maiani (GIM) [43] introduced a new quantum number, the charmness, to cancel the unobserved FCNC transitions. The yet unobserved charm quark c completed the second family generation and the four quarks were now arranged in two doublets (u, d') and (c, s') with

$$d' = d\cos\theta_C + s\sin\theta_C \tag{3.15}$$

$$s' = -d\sin\theta_C + s\cos\theta_C. \tag{3.16}$$

The weak neutral current has now an additional contribution such that the FCNC term in Eq. 3.14 cancels exactly at tree level. As a result, there is no longer the possibility of FCNC at lowest order in the SM consistent with the experimental finding. However, it turned out that leading order (and higher order) FCNC contributions to such processes are still possible and occur in so-called box or penguin diagrams giving rise to small and rare FCNC transitions that were indeed observed in the past.

Historically, the small measured mass difference of the K_S and K_L mesons and the absence of FCNC transitions in $K_L \rightarrow \mu^+\mu^-$ allowed in the GIM model a quantitative prediction [44] of the mass of the new charm quark before it was actually discovered by teams at SLAC [45]

and BNL [46] in 1974. There are further examples that nicely demonstrate how FCNC processes have significantly shaped the SM. For instance, the observation that large FCNC processes were absent in B decays ruled out "top-less" models, i.e., models without top quark in the beginning of the 80ies. The large $B^0 - \bar{B}^0$ mixing that was first observed at ARGUS [38] suggested that the top mass has to be much larger than in the 30-40 GeV/c^2 mass range which was claimed by the experiment UA1 at that time.

Given these historical examples with their theoretical consequences, a motivation to study further rare FCNC decays in the b-quark sector is obvious. FCNC processes are probing virtual particles in the loop and can thus discern new physics. Hence, with a study of FCNC at low energy much about high mass scales can be learned.

3.2.3 Box and Penguin Diagrams

FCNC decays are absent in the SM at tree level. At one loop level the new FCNC transitions that now appear can be summarized by a set of basic triple and quartic effective vertices. In the literature they are referred to as box diagrams with exchange of two W bosons and penguin[2] diagrams, respectively. Examples of such box and penguin diagrams are shown in Fig. 3.20(b)-(f). For instance, the box diagram of Fig. 3.20(e) is responsible for $K^0 - \bar{K}^0$ and $B^0 - \bar{B}^0$ mixing.

Penguin diagrams can be separated in gluonic (Fig. 3.20(b)) and electroweak penguins (Fig. 3.20(c)). The effective vertices can be calculated by using elementary vertices and propagators, and effective Feynman rules can be derived. The higher order in the gauge couplings contributes to the suppression of these diagrams. Their relative importance depends on the mass of the internal fermion lines, which explains the importance of the contribution of the top quark, and on the relevant CKM matrix element.

It is instructive to understand why FCNC transitions of s and b decays are so interesting. Since FCNC are proceeding through box- or penguin diagrams, a loop factor $g^2/16\pi^2 \sim 10^{-2}$ suppresses its decay. In addition, due to the GIM mechanism the transition rates at higher order follow a (suppressing) mass difference δm_i dependence that is of quadratic $\delta m_i^2/M_W^2$ and logarithmic $\log \delta m_i^2/M_W^2$ forms. FCNC transitions for all down-type (s and b) quarks are sensitive to the mass difference of the up-type (u, c and t) quarks in the loop and vice versa. Were all up-type (down-type) quark masses equal, FCNC decays would disappear at higher loop. In more detail, the condition for a complete cancelation of FCNC terms due to the GIM mechanism are the unitarity of the CKM matrix and exact flavor symmetry ensuring the equality of quark masses of a given charge.

In nature however, there is a quark mass hierarchy $m_u < m_d \ll m_s \ll m_c < m_b \ll m_t$, such that the large top mass $m_t > M_W \gg m_c, m_u$ relaxes the GIM suppression and drives the down-type quark FCNC, giving rise to $b \to s$, d and $s \to d$ processes. The sizes of the CKM matrix elements lead then to transition rates that are largest for $b \to s\,(\sim \lambda^2)$ with experimental accessible branching ratios of 10^{-5}. The decay $b \to d\,(\sim \lambda^3)$ is suppressed by another factor λ and finally $s \to d\,(\sim \lambda^5)$ rare K decays have branching ratios of 10^{-10}.

For up-type quarks, FCNC decays are much more suppressed due to the small intermediate

[2]The original term penguin goes back to J. Ellis. It is said, that he lost a bet during a game of darts. His penalty required to use the word "penguin" in his next journal article. In his paper [47] on b quark decays he associated the famous diagrams with penguins. The similarity between the diagram and a cartoon of a penguin is shown in Fig. 3.21.

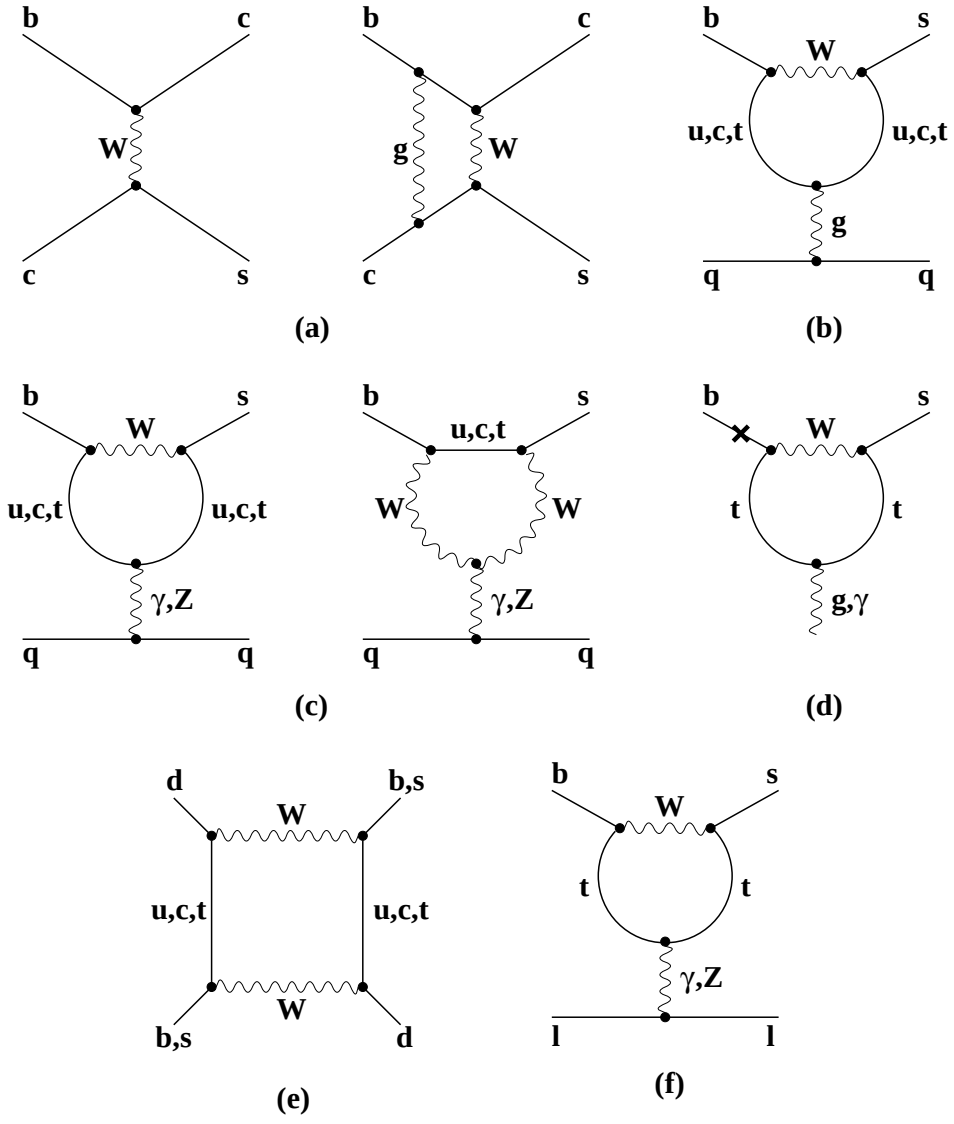

Figure 3.20: Feynman diagram representations of box and penguin processes.

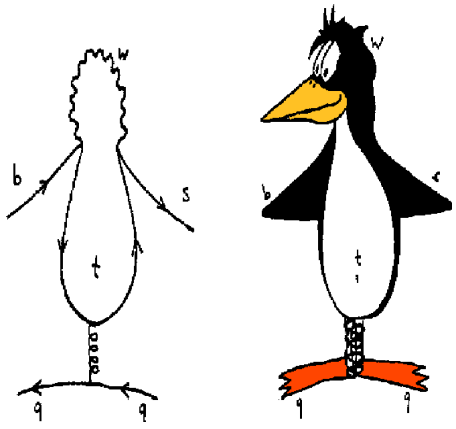

Figure 3.21: Cartoon of a penguin.

masses of d, s and b quarks with $m_d, m_s, m_b \ll M_W$ entering the loop, making the GIM mechanism more effective. For example, the rare charm decay $c \to u\gamma$ has a GIM mass suppression of 10^{-18}, since the internal quarks are s and d. With QCD corrections however, the charm decay is softened to 10^{-8}. Moreover, the known structure of the CKM matrix is less favorable than in K and B decays: The CKM matrix elements of $c \to s$ and $t \to b$ transitions are large. The converse is true for s and b: the life times are prolonged by the smallness of V_{us} and V_{cb} and/or V_{ub}.

3.2.4 Low Energy effective Hamiltonians

The basic challenge in calculating branching ratios or other observables of rare hadron decays is related to strong interacting particles. Even if the QCD effective coupling at short distance is sufficiently small to apply the framework of perturbative QCD calculations, the fact that a meson is a bound $q\bar{q}$ state forces to consider QCD at long distances as well, where only non-perturbative methods with less predictive power are applicable.

The operator product expansion (OPE) combined with the renormalization group approach allows to divide the problem into two parts: a short-distance part that is under control of perturbative QCD, and a long-distance part. The OPE introduces local operators which are generated by QCD and electroweak interactions and are governing "effectively" the decay in question. Based on the operators, a low-energy effective Hamiltonian $\mathcal{H}_{eff}$ is then obtained, that yields the transition matrix elements from an initial hadronic state i to a final state f:

$$< f|\mathcal{H}_{eff}|i >= \frac{G_F}{\sqrt{2}} \lambda_{CKM} \sum_k C_k(\mu) < f|Q_k(\mu)|i > \tag{3.17}$$

Here, G_F is the Fermi constant, λ_{CKM} is a CKM factor and μ is an appropriate renormalization scale. The local operators are denoted as Q_k and C_k stands for the Wilson coefficients, that are calculated by perturbative methods. The Wilson coefficients C_k can be considered as scale-dependent couplings related to the vertices described by Q_k.

The scale μ separates the physics contributions in a short-distance part (coming from a scale larger than μ) that is absorbed into C_k and the long-distance component (scales lower than μ) contained in the hadronic matrix element $< f|Q_k(\mu)|i >$. For B decays the scale μ is chosen to be at the order of a few GeV, i.e., around the mass of the b-quark. With the help of the renormalization group equations, information from the hadronic matrix elements at scales much higher than μ are transformed into C_k. Since the full amplitude can not depend on the scale μ the μ-dependence of matrix elements and Wilson coefficients must cancel. In general this cancelation works only, if many operators due to operator mixing under renormalization are involved. Basically, there are infinitely many terms in the OPE, but higher dimension operators yield contributions suppressed by powers of μ^2/M_W^2. Therefore, when calculating a decay amplitude, terms with $\mathcal{O}(\mu^2/M_W^2)$ and higher can be neglected.

A set of basic operators entering the OPE can be specified at short distance, i.e., without knowing the difficult non-perturbative part. Those operators are driving the weak decay and are depicted as diagrams in Fig. 3.20. The following six classes of operators are playing the dominant role in the phenomenology of weak decays:

Current–Current (Fig. 3.20a):

$$\begin{aligned} Q_1 &= (\bar{s}_{L\beta}\gamma_\mu c_{L\alpha})\,(\bar{c}_{L\alpha}\gamma^\mu b_{L\beta}) \\ Q_2 &= (\bar{s}_L\gamma_\mu c_L)\,(\bar{c}_L\gamma^\mu b_L) \end{aligned}$$

QCD–Penguins (Fig. 3.20b):

$$\begin{aligned} Q_3 &= (\bar{s}_L\gamma_\mu b_L)\sum_{q=u,d,s,c,b}(\bar{q}\gamma^\mu q) \\ Q_4 &= (\bar{s}_{L\alpha}\gamma_\mu b_{L\beta})\sum_{q=u,d,s,c,b}(\bar{q}_{L\beta}\gamma^\mu q_{L\alpha}) \\ Q_5 &= (\bar{s}_L\gamma_\mu b_L)\sum_{q=u,d,s,c,b}(\bar{q}_R\gamma^\mu q_R) \\ Q_6 &= (\bar{s}_{L\alpha}\gamma_\mu b_{L\beta})\sum_{q=u,d,s,c,b}(\bar{q}_{R\beta}\gamma^\mu q_{R\alpha}) \end{aligned}$$

Electroweak–Penguins (Fig. 3.20c):

$$\begin{aligned} Q_{3Q} &= \frac{3}{2}\,(\bar{s}_L\gamma_\mu b_L)\sum_{q=u,d,s,c,b}e_q\,(\bar{q}_R\gamma^\mu q_R) \\ Q_{4Q} &= \frac{3}{2}\,(\bar{s}_{L\alpha}\gamma_\mu b_{L\beta})\sum_{q=u,d,s,c,b}e_q(\bar{q}_{R\beta}\gamma^\mu q_{R\alpha}) \\ Q_{5Q} &= \frac{3}{2}\,(\bar{s}_L\gamma_\mu b_L)\sum_{q=u,d,s,c,b}e_q(\bar{q}_L\gamma^\mu q_L) \\ Q_{6Q} &= \frac{3}{2}\,(\bar{s}_{L\alpha}\gamma_\mu b_{L\beta})\sum_{q=u,d,s,c,b}e_q\,(\bar{q}_{L\beta}\gamma^\mu q_{L\alpha}) \end{aligned}$$

Magnetic–Penguins (Fig. 3.20d):

$$Q_7 = \frac{e}{16\pi^2}m_b\bar{s}_{L\alpha}\sigma^{\mu\nu}b_{R\alpha}F_{\mu\nu}$$

$$
\begin{aligned}
Q_8 &= \frac{g}{16\pi^2} m_b \bar{s}_{L\alpha} \sigma^{\mu\nu} T^a_{\alpha\beta} b_{R\beta} G^a_{\mu\nu} \\
Q_{7'} &= \frac{e}{16\pi^2} m_s \bar{s}_{R\alpha} \sigma^{\mu\nu} b_{L\alpha} F_{\mu\nu} \\
Q_{8'} &= \frac{g}{16\pi^2} m_s \bar{s}_{R\alpha} \sigma^{\mu\nu} T^a_{\alpha\beta} b_{L\beta} G^a_{\mu\nu}
\end{aligned}
$$

$\Delta F = 2$ ($\Delta S = 2$ **or** $\Delta B = 2$) **Operators (Fig. 3.20e):**

$$
\begin{aligned}
Q(\Delta S = 2) &= (\bar{s}_L \gamma_\mu d_L)(\bar{s}_L \gamma^\mu d_L) \\
Q(\Delta B = 2) &= (\bar{b}_L \gamma_\mu d_L)(\bar{b}_L \gamma^\mu d_L)
\end{aligned}
$$

Semi–Leptonic Operators (Fig. 3.20f):

$$
\begin{aligned}
Q_9 &= \frac{e^2}{16\pi^2} (\bar{s}_L \gamma_\mu b_L)(\bar{l} \gamma^\mu l) \\
Q_{10} &= \frac{e^2}{16\pi^2} (\bar{s}_L \gamma_\mu b_L)(\bar{l} \gamma^\mu \gamma_5 l) \\
Q_{9'} &= \frac{e^2}{16\pi^2} (\bar{s}_R \gamma_\mu b_R)(\bar{l} \gamma^\mu l) \\
Q_{10'} &= \frac{e^2}{16\pi^2} (\bar{s}_R \gamma_\mu b_R)(\bar{l} \gamma^\mu \gamma_5 l) \\
Q_{\nu\bar{\nu}} &= \frac{\alpha_{em}}{4\pi} (\bar{s}_L \gamma_\mu b_L)(\bar{\nu}_L \gamma^\mu \nu_L)
\end{aligned}
$$

Here, the subscripts L and R refer to left- and right-handed components of the fermion fields. The quark colour indices are represent by α and β and are omitted for colour singlet currents. $F_{\mu\nu}$ and $G^a_{\mu\nu}$ are the electromagnetic and strong interaction tensors and e_q is the electric charge of the relevant quark. The above set of operators is characteristic for any consideration of the interplay of QCD and electroweak effects. Since the ratio $\alpha/\alpha_s \sim 10^{-2}$ of the QED and QCD couplings is very small, it is naively expected that electroweak penguins should play a minor role in comparison with QCD penguins. This would actually be the case if the top quark was not heavy, but the Wilson coefficients of the electroweak operators receives a large contribution from top quark loops at the electroweak scale.

The calculation of the rare decay rates involves then three distinct steps: First, the determination of the initial conditions of the Wilson coefficients at the electroweak scale. Secondly, the evolution by means of the renormalization group equations of the C_k down to $\mu = \mathcal{O}(m_b)$ and finally, the evaluation of the hadronic matrix elements of the effective operators at $\mu = \mathcal{O}(m_b)$, including both perturbative and non-perturbative QCD corrections.

3.3 FCNC and New Physics

Although the SM is in overwhelming agreement with so many precision data and has passed many experimental tests and challenges in the past, it is very likely to be only an effective theory valid at a low energy. As an effective theory the SM is a good approximation up to some scale Λ to the deeper and yet unknown theory of fundamental interactions. Such a more complete model should among other things include gravity, allow for gauge coupling unification and provide a dark matter candidate as well as explain an efficient mechanism for baryogenesis.

An effective theory can be described by a Lagrangian

$$\mathcal{L}(M_W) = \mathcal{L}_{SM}^{\text{Higgs}} + \mathcal{L}_{SM}^{\text{gauge}} + \mathcal{L}_{SM}^{\text{Yukawa}} + \frac{1}{\Lambda}\mathcal{L}^{(5)} + \frac{1}{\Lambda^2}\mathcal{L}^{(6)} + \cdots . \tag{3.18}$$

There are good theoretical reasons to assume that the cut-off scale Λ lies close to the mass of the electroweak scale M_W. Then, the power suppression due to higher dimensional operators in $\mathcal{L}^{(5,6)}$ is not too strong to produce sizeable effects in low-energy processes provided that they do not compete with tree-level SM contributions. Thus, one should look for SM process that are absent at tree-level, but are finite and calculable at higher order quantum theory. Due to their large suppression in the SM, FCNC decays are ideal places to look for evidence of higher-dimensional operators and hence for new physics. The FCNC transitions are also calculable in terms of quark masses and elements of the CKM matrix.

Many extensions to the SM that include new interactions or new particles can introduce modified or new FCNC decays, which have to be confronted with existing experimental data. While constructing such models it has to be ensured that they pass tight experimental tests since data on FCNC processes provide already strong constraints. In the following a list of possible extensions to the SM are given that may affect FCNC interactions.

1. Supersymmetry and multi-Higgs doublets
   This is a broad and the most important class of extensions to the SM and will be further discussed in detail.

2. Extra quark models
   These are models [48] with an addition of an isosinglet down-type vector-like quark b' to the SM. The models naturally arise as a low-energy limit of grand unified theories and lead to FCNC tree processes.

3. Fourth generation models
   Quarks t' from a possible fourth generation [49] can lead to FCNC through box-diagrams.

4. Anomalous WWZ couplings
   Such anomalous couplings affect mainly all electroweak penguin diagrams and can be induced, for instance, by non-universal Z bosons, which result from an extra $U(1)$ symmetry [50]. In case of this new $U(1)$ symmetry FCNC tree level contributions are induced by $Z - Z'$ mixing.

5. Extended Technicolor models
   In technicolour models, there is no fundamental Higgs scalar particle. Instead, additional scalar particles (techni-particles) are introduced to connect the technicolour condensate to the ordinary fermions. In several extended technicolor models FCNC effects are predicted [51] by new Z couplings and new four-fermi operators.

6. Leptoquark models
   Leptoquarks carrying lepton and quark flavor numbers can mediate FCNC decays of mesons at tree level [52].

7. Extra Dimensions
   The idea of extra dimensional (ED) models [53] is that extra compactified space-like

dimensions at a scale larger than the Planck scale of $\sim 10^{-33}$ cm exist. This idea leads to exciting perspectives for particle phenomenology, cosmology and string theory. In universal ED models, SM particles are allowed to travel in all available extra dimensions. Such a higher-dimensional theory can be described as an effective theory in four dimensions which contains an infinite tower of Kaluza-Klein modes of the higher dimensional field. Each boson line in FCNC diagrams will now involve several Kaluza-Klein modes. An enhancement of FCNC decays depends on the compactification scale and the number of extra dimensions.

In the SM only one Higgs doublet is required to spontaneously break the electroweak symmetry and to give masses to leptons and quarks. It had always been obvious that the Higgs boson of the SM could not have flavor-changing couplings since the couplings to fermions to the Higgs field define the fermion mass eigenstates and thus defines also the notion of flavor [54]. However, there is no strong motivation for this minimal Higgs sector. Most extensions in the SM, e.g. supersymmetry, have a more complicated Higgs sector. The simplest extension of the SM consists then of adding a second Higgs doublet, such that the physical eigenstates comprise of three neutral and two charged Higgs scalars. It was realized very early, that models with more than one Higgs-doublet could lead to large FCNC processes on tree-level, since the fermion mass eigenstates can in principle be different from the Higgs interaction eigenbasis. However, such large Higgs-mediated FCNC are in contradiction to experimental data and have to be carefully avoided in all realistic models with extended Higgs sector. The solution to this problem was the introduction of the principle of natural flavor conservation [55], that requires that all quarks of a given charge couple to one single Higgs doublet H_i, eliminating FCNC process at tree level. In case of models with two Higgs doublets (2HDM) there are now three configurations possible: In the type-I 2HDM all the quarks couple to the first doublet H_1 and none to the second one H_2, while in the type-II 2HDM the down-type right-handed quark singlets couple to H_1 and the up-type right handed quark singlet to H_2 only. The most general type-III 2HDM model allows a coupling of each right-handed fermion singlet type to both doublets, such that natural flavor conservation is not obeyed in general.

3.4 Introduction to Supersymmetry

3.4.1 General Overview

Assuming the SM Higgs mechanism of electroweak symmetry breaking one is faced with the question of the mass hierarchy: Why is M_W so much smaller than the Planck scale M_P? The latter scale is the only candidate for a fundamental mass scale, at which gravity is expected to become as strong as the electroweak interaction. The problem with that is that universal scalar masses like the Higgs mass receive quadratically divergent quantum corrections $\delta_{M_H^2} = \mathcal{O}(\alpha/\pi)\Lambda^2$ from radiative loops involving, e.g., scalars and fermions. This would push the radiative corrections of the scalars to much larger values than the physical value of $M_{H,W}$ itself, a behavior which is considered as very unnatural, since unlike fermions or gauge bosons scalar masses are not protected by any symmetry.

Supersymmetry (SUSY) solves this hierarchy problem by introducing a symmetry that links bosons and fermions together and stabilizes the Higgs sector against divergent loop corrections. Every particle in the SM has now a supersymmetric partner differing in spin by

1/2. Quarks, leptons and neutrinos have as counterparts the spin-0 squarks, sleptons and sneutrinos; the partner of the gluon is the spin-1/2 gluino; and the partners of the charged (neutral) vector bosons and Higgs bosons are the spin-1/2 charginos (neutralinos). Often the latter can be approximately separated into the spin-1/2 bino and wino gaugino partners of the U(1) B and SU(2) W gauge fields and the higgsino partners of the Higgs field. In other cases these states are strongly intermixed. Supersymmetry features a special Higgs sector. In the minimal supersymmetric model (MSSM) a two-doublet Higgs-sector exists, whose physical eigenstates comprise of two CP-even scalars (h^0, H^0), a CP-odd scalar (A^0), and a charged Higgs pair ($H^{\pm}$).

SUSY can not be realized as an exact symmetry in nature, since sparticle with the same masses than their SM counterparts have not been observed. Hence, SUSY must be broken at a certain scale such the sparticle masses become heavier. If soft supersymmetry breaking is realized, then the elimination of the quadratic divergences for the Higgs mass is still realized.

In supergravity models, SUSY is assumed to be broken in a hidden sector consisting of fields that interact with usual particles and their superpartners only via gravity. SUSY breaking is communicated to the visible sector via gravitational interactions and soft SUSY breaking sparticle masses are generated. Without further assumptions, the scalar masses can be arbitrary leading to flavor changing processes in conflict with experiment.

The minimal supergravity model (mSUGRA) framework [56] postulates that at some high scale, which is frequently taken to be the grand unified scale M_{GUT}, all scalar fields have a common SUSY breaking mass m_0, all gauginos have a mass $m_{1/2}$, and all soft SUSY breaking trilinear couplings have a common value A_0. Electroweak symmetry breaking is assumed to occur radiatively, which fixes the superpotential parameter μ. The highly predictive mSUGRA model is completely specified by the parameter set:

$$m_0,\ m_{1/2},\ A_0,\ \tan\beta,\ \mathrm{sign}(\mu).$$

Here, $\tan\beta$ represents the ratio of the vacuum expectation value for the two Higgs fields. The first three quantities above are defined at a high, grand unified energy scale and the others at the electroweak scale. The weak scale SUSY parameters that enter the computation of sparticle masses and couplings required for phenomenological analyses can be obtained via renormalization group evolution between the scale of grand unification and the weak scale. The small numbers of input parameters makes mSUGRA to the best studied supersymmetric framework with high predictive power that can be rigorously tested at low energy scales.

Another theoretical mechanism for a potential SUSY breaking is minimal gauge-mediated SUSY (mGMSB), where the hidden sector couples to messenger particles. These models feature the SUSY breaking to be a low-energy phenomena if the messenger scale is low. In such cases the gravitino can be an ultra-light supersymmetric particle.

There is possibly an exact discrete symmetry of SUSY, called R-parity, such that SM particles have $R = +1$ while the sparticle partners have $R = -1$. The new quantum number R-parity was introduced to avoid lepton and baryon number violating process leading to severe contradiction to tight experimental constraints such as the lower limit on the proton life time. If R parity is an exact symmetry, then any physical process must always involve an even number of sparticles, and the lightest supersymmetric particle (LSP), in supergravity models the neutralino χ_1^0, will be stable against decay to SM particles. This has the desirable feature, that a neutralino as LSP represents a very attractive candidate for dark matter.

3.4.2 The Higgs Penguin

Unbroken SUSY belongs to the class of type-II 2HDM, i.e., all matter multiplets with one weak isospin charge $T_3 = 1/2$ couple only to the first Higgs doublet H_u, while the other multiplet with $T_3 = -1/2$ couple to the other doublet H_d. This so-called holomorphic structure is a natural realization in R-parity conserving SUSY models at tree-level. After breaking SUSY however, this natural separation of the two Higgs doublets does not exist anymore and a coupling of H_u to down-like fermions at one loop level is induced. The direct consequence is that the down-type Yukawa coupling matrices and down-type quark mass matrices are no longer diagonalized by the same transformation and flavor violating couplings of the neutral Higgs bosons h, H and A emerge. In that respect, the effective low-energy theory of SUSY is a type-III 2HDM. Although the FCNC contributions from the neutral Higgs bosons are expected to be loop-suppressed relative to the tree-diagram, i.e., as small or even smaller than SM flavor-changing transitions, its suppression can be partially compensated if $\tan\beta$ is sufficiently large. It was first realized in Ref. [57], that the enhanced FCNC SUSY interactions at large $\tan\beta$ can significantly alter the neutral Higgs boson couplings and can generate a variety of flavor-changing processes including $B_s^0 - \bar{B}_s^0$ mixing and certain decay rates such as $B_s^0 \to \ell^+\ell^-$. The interesting feature of this enhancement is that the flavor-violating couplings do not decouple for large supersymmetric particle masses. Thus, they remain finite even for very large values of SUSY mass parameters and represent an unique way to discover SUSY if squark masses are at the multi-TeV scale, where they may escape detection in direct searches.

There are several distinct sets of SUSY sources for the one-loop coupling of this so-called Higgs penguin [58]. All diagrams that appear in the SUSY Higgs penguin graph are shown in Fig. 3.22. The name Higgs penguin was chosen to denote $f - H - f'$ processes with fermion transitions $f \to f'$.

In the general MSSM, two classes of FCNC Higgs couplings can principally be distinguished: minimal and non-minimal flavor violation. In the MSSM with minimal flavor-violation (MFV), the sfermion mass matrices are flavor-diagonal in the same basis as the quark and lepton mass matrices. Then, the only source of FCNC is the CKM matrix as in the SM. The main corrections to the SUSY Higgs penguin arise from the self-energy diagrams of Fig. 3.22(g,j). Down-type quarks can couple to H_u via a chargino and up type squark loop which is enhanced by $\tan^2\beta$ with respect to the SM and represents the dominant contribution. Other contributions with the charged Higgs boson are also present, but are subdominant since they are scaling with $\tan\beta$ only.

Non-minimal or general flavor-changing occurs when the sfermion mass matrices are non flavor-diagonal in the same basis as the quark and lepton mass matrices. When the sfermion mass matrices are diagonalized, flavor-changing gluino-squark-quark and neutralino-sfermion-fermion couplings are introduced. Such a general flavor violation is present in most general MSSM, and can lead to large flavor-changing effects in strong contradiction to experiments. This phenomena is called the SUSY flavor problem and has to be solved in any realistic MSSM scenario.

Since the general MSSM framework with sparticle mass matrices as well as soft SUSY breaking coupling matrices is too broad and complex, it is rather difficult to make definite predictions for FCNC processes in general flavor violating SUSY. The situation is in sharp contrast in highly predictive and constrained SUSY scenarios such as the mSUGRA model,

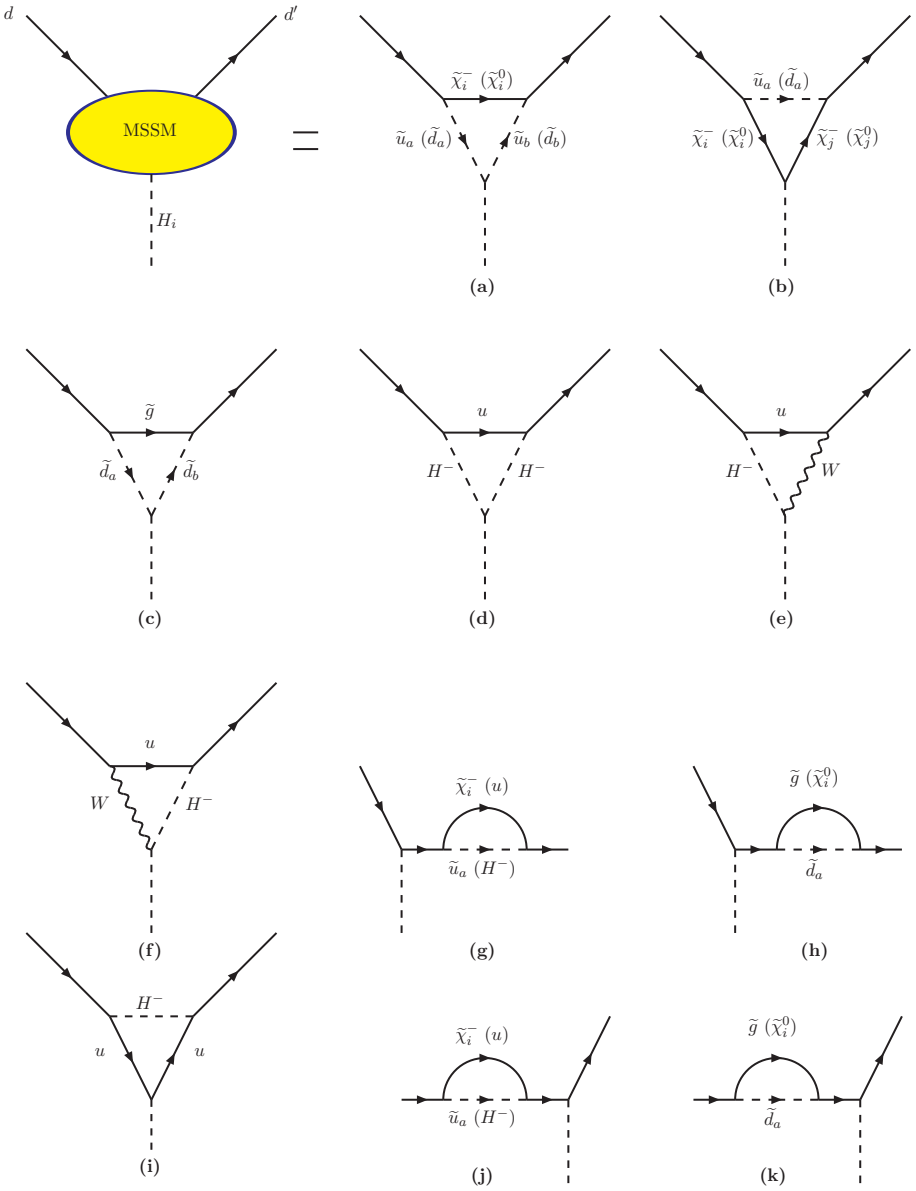

Figure 3.22: General SUSY contributions to the Higgs penguin (taken from Ref. [58]). The blob in the top left graph illustrates the MSSM Higgs penguin $f - H - f'$ with flavor-violating transitions between the fermions f and f'.

which minimizes the number of parameters to only a few.

4 Overview of Rare B Decays

In the following sections the most important FCNC B decays are discussed. The SM calculations on their branching ratios and the experimental results – if available – are presented and possible implications due to new physics is described.

By definition the presented B decays are rare, since they do not proceed through the dominant $b \to c$ transition. Their branching ratios vary from 10^{-13} to 10^{-6}. There are several golden channels in which the hadronic physics, i.e., long-distance effects can be disentangled such that very clean tests of the SM are possible. Moreover, there are also several observables, which make precision flavor physics possible in the near future.

If the quark level transition of the FCNC B decay contains a quark in the final state, inclusive and/or exclusive calculations and measurements are possible. The inclusive decays can be calculated perturbatively up to power corrections, using quark-hadron duality and the optical theorem by summing over all final states. Schematically, the decay width is given by

$$\sum_{X_q} \langle B|Q|X_q\rangle\langle X_q|Q^\dagger|B\rangle = \sum_{p} \langle B|Q|p\rangle\langle p|Q^\dagger|B\rangle \tag{4.19}$$

where X_q is any final hadronic state consisting a bound quark q and the sum over p represents the sum over quarks and gluons.

In view of precision tests of the flavor sector of the SM inclusive rare B decay channels, in which over the final hadronic state X_q is summed, play the most crucial role. The inclusive rates can be well approximated by partonic rates plus non-perturbative corrections that are subdominant thanks to the heavy quark expansion $\mathcal{O}(1/m_b)$. The matrix element is then usually written as an expansion in terms of $1/m_b$. To first order, the hadronic matrix element $\langle X_q|Q|B\rangle$ corresponds to the matrix element of the free quarks $\langle q|Q|b\rangle$, which can be calculated perturbatively. Corrections due to virtual and real gluons need to be added. Power corrections ($\mathcal{O}(1/m_b^2)$) describe the difference between initial b-quarks and B mesons and may cause some changes to the decay rates depending on the FCNC process.

Calculations for exclusive states are on general theoretical grounds more difficult to perform than their inclusive counterparts. On the experimental side however, it is easier to measure exclusive decays, in particular if only one hadron is present in the final state. There has been substantial theoretical progress in the last years by applying analytical methods and lattice QCD to determine exclusive matrix elements. Nevertheless, the theoretical uncertainty on the amplitude level for exclusive decays is around 15-20%. The largest source is typically the normalization of the hadronic form factors. This error might be avoided by using appropriate ratios or differential distribution.

4.1 $B \to X_{d,s}\gamma$

The inclusive decay $B \to X_s\gamma$, also called radiative penguin, with X_s indicating any hadronic final state containing a s quark, played a very important role in the phenomenology of rare B decays. Historically, the first exclusive radiative penguin decay in the B sector that were discovered, were $B \to K^*\gamma$ and $B^\pm \to K^{*\pm}\gamma$ FCNC transitions by the CLEO collaboration in 1993 [39]. Their observations triggered an extensive experimental and theoretical program to study those decays in detail.

The effective Hamiltonian of $B \to X_s\gamma$ is given by

$$\mathcal{H}_{eff} = -\frac{4G_F}{\sqrt{2}} V_{ts}^* V_{tb} \sum_{j=1}^{8} C_j(\mu) Q_j(\mu) \tag{4.20}$$

with the basis for this decay consisting of the first eight operators in the expansion. The effective Hamiltonian is mostly dominated by the magnetic dipole transition operator Q_7. The matrix element calculation rate has been calculated [59] up to next-to-leading-log (NLL) accuracy with higher order electroweak corrections [60]. The long-distance effects and non-perturbative $\mathcal{O}(1/m_b)$ contributions are well under control in the total rate. The dominant short-distance QCD corrections enhance the partonic decay rate by a factor of more than two. At NLL the theoretical SM branching ratio is predicted to be [60]

$$\mathcal{B}(B \to X_s\gamma)_{SM} = (3.73 \pm 0.30) \times 10^{-4}, \tag{4.21}$$

where the full photon energy spectrum is included. The uncertainty in the calculations reflects mostly higher order corrections. In view of the accurate measurements that are expected in the next years, the NNLO calculations are presently pursued.

It is a great success of the SM that the current world average measurement [9]

$$\mathcal{B}(B \to X_s\gamma)_{exp} = (3.39^{+0.30}_{-0.27}) \times 10^{-4} \tag{4.22}$$

is in excellent agreement to the theoretically predicted rate. This world average value is dominated by CLEO, Belle and Babar results. The remarkable consistency has led to several tight constraints on models of new physics [61]. For instance, in type-II 2HDM models, the mass of the charged Higgs boson is bound to be above 350 GeV/c^2, if no destructive interference terms occur [62]. Many SUSY models, however, may have a destructive amplitude that may cancel the constructive part. Nevertheless, the inclusive $b \to s\gamma$ result limits the magnitude of the C_7 Wilson coefficient and serves as an important input to the constrains of other measurements.

The precise theoretical calculations of the inclusive mode $B \to X_s\gamma$ does not hold in exclusive radiative decays such as $B \to K^*\gamma$ which makes about 12% of the inclusive rate. Due to the hadronic transition from a B to a K^* meson, hadronic form factor are necessary, which solely account for a 10-15% uncertainty in the branching ratio.

Recently the Belle collaboration reported for the first time the observations of CKM-suppressed $b \to d\gamma$ transitions [63] by measuring $B \to (\rho, \omega)\gamma$ decays. By using the ratio of $\mathcal{B}(B \to \rho^0\gamma)/\mathcal{B}(B \to K^*\gamma)$ the CKM matrix element $|V_{td}/V_{ts}|$ can be extracted even before $\Delta M_s/\Delta M_d$ is measured. The obtained results are in a good agreement with the predictions from the SM and a fit to the unitarity triangle [64]. An improved measurement of the decay rate $b \to d\gamma$ will help to reduce the currently allowed region of the CKM Wolfenstein parameters ρ and η. It is also important with respect to new physics, because its CKM suppression ($|V_{td}/V_{ts}|^2$) in the SM might not hold in extended models which allow general flavor violation.

There are also many possible radiative penguin decays that occur in the B_s^0 and $B_c^\pm$ meson systems as well as in b-flavored baryons. A study of these decays would contribute to the general knowledge of $b \to s\gamma$ transitions and a systematic exploration of exclusive $b \to s\gamma$ transitions in the B_s^0, $B_c^\pm$ and Λ_b systems will be definitively part of the future LHCb

physics program. None of these decays have been measured so far and experimental limits exist only on two decays. The 90% C.L. upper limits of exclusive radiative penguin decays were obtained by LEP [65] for the B_s^0 decay and at Tevatron [66] for the Λ_b penguin decay:

$$\mathcal{B}(B_s^0 \to \phi\gamma)_{exp} < 1.2 \times 10^{-4} \quad (4.23)$$

$$\mathcal{B}(\Lambda_b \to \Lambda\gamma)_{exp} < 1.3 \times 10^{-3} \quad (4.24)$$

The SM values are

$$\mathcal{B}(B_s^0 \to \phi\gamma)_{SM} = (4.2 \pm 2.0) \times 10^{-5} \ \ [67] \quad (4.25)$$

$$\mathcal{B}(\Lambda_b \to \Lambda\gamma)_{SM} = 0.2 - 1.5 \times 10^{-5} \ \ [68] \quad (4.26)$$

The $B_c^\pm$ meson system offers beside $b \to s\gamma$ decays, as in $B_c^\pm \to D_s^*\gamma$, also the interesting FCNC transitions $c \to u\gamma$. This could allow on a long-term scale the investigation of flavor-violating up-type quark transitions at LHC, which are experimentally completely unexplored. The decaying $B_c^\pm$ system is well suited for such $c \to u\gamma$ studies, since perturbative calculations are in principle possible. The same transitions in charmed meson decays are normally overwhelmed by long-distance contributions.

4.2 $B \to X_s\ell^+\ell^-$

The decays $B \to X_s\ell^+\ell^-$ offer a phenomenology that is richer than $B \to X_s\gamma$ transitions with more than one interesting observable. The lepton pair in the final state allows to calculate kinematical quantities that are considered as good probes of new physics.

The decay $B \to X_s\ell^+\ell^-$ receives short-distance contributions from W-box, from electromagnetic and Z^0-penguin diagrams. The operators contributing to the effective Hamiltonian are the current-current operators (Q_1, Q_2), the QCD-penguin operators $(Q_3, \ldots, Q_6)$, the magnetic penguin operators $(Q_{7\gamma}, Q_{8\gamma})$ and the semi-leptonic Z^0 and γ penguin operators (Q_{9V}, Q_{10A}). The effective Hamiltonian is

$$\mathcal{H}_{eff} = -\frac{4G_F}{\sqrt{2}} V_{ts}^* V_{tb} \sum_{j=1}^{10} C_j(\mu) Q_j(\mu). \quad (4.27)$$

The joint effort of several groups has allowed to calculate all necessary coefficients and matrix elements for the two main kinematical distributions at NNLL accuray: the forward-backward asymmetry [69] A_{FB} shown in Fig. 4.23 and the di-lepton mass spectrum [70] presented in Fig. 4.24.

The forward-backward asymmetry A_{FB} for leptons as a function of the squared di-lepton mass $m^2_{\ell^+\ell^-} = q^2$ is defined as

$$A_{FB}(q^2) = \frac{\displaystyle\int_0^1 \frac{d^2\Gamma}{dx dq^2}\, dx - \int_{-1}^0 \frac{d^2\Gamma}{dx dq^2}\, dx}{\displaystyle\frac{d\Gamma}{dq^2}}, \quad (4.28)$$

where $x \equiv \cos\theta$ parameterizes the angle between the ℓ^+ and the B meson in the di-lepton center-of-mass frame. Assuming only a vector (V) or axial-vector (A) structure of the leptonic current as in the SM, the measure of A_{FB} represents a direct test of the $V - A$ interference.

The forward-backward asymmetry preserves three main feature of short-distance physics:

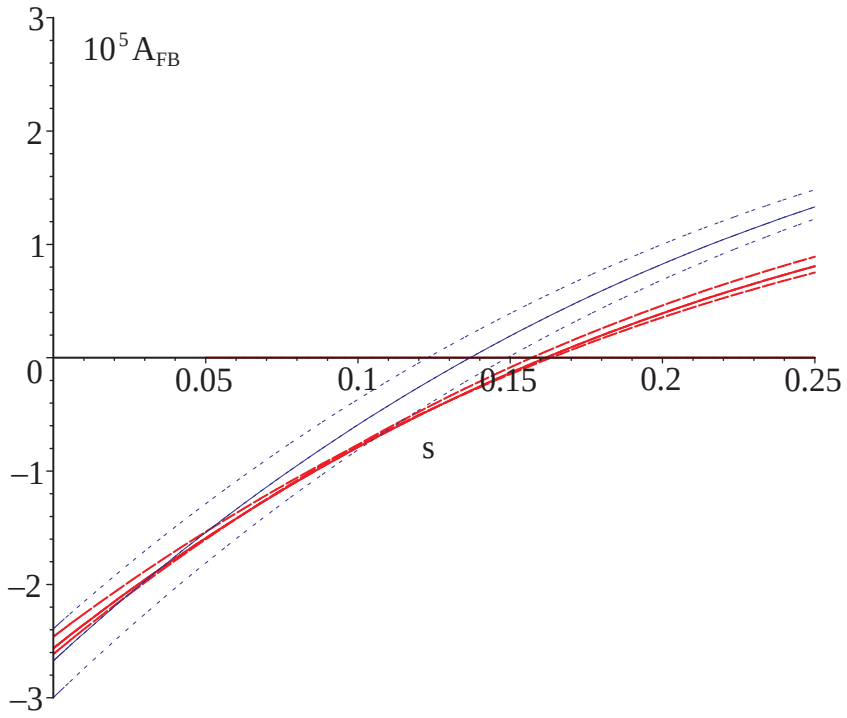

Figure 4.23: The A_{FB} spectrum for inclusive $B \to X_s \ell^+ \ell^-$ decays within the SM as function of $s = q^2/m_b^2$. The three thick lines denote the NNLL perturbative calculation for two choices of the renormalization scale $\mu = 5$ (full), $\mu = 2.5$ and $\mu = 10$ GeV (dashed). The dotted curves are the corresponding NLL results. The figure is taken from Ref. [71].

- The position q_0^2 of the zero of $A_{FB}(q^2)$ in the low q^2 regions. The value q_0^2 for which the differential forward-backward asymmetry vanishes, is one of the precise predictions in flavor physics. For inclusive decays it is calculated to NNLL accuracy to be $q^2_{0,NNLL} = (3.90 \pm 0.25)$ GeV^2. The experimental measurement of q_0^2 could allow a determination of C_7/C_9 at the 10% level.

- The sign of $A_{FB}(q^2)$ around the zero. This is fixed unambiguously in terms of the relative sign of C_9 and C_{10}. Within the SM one expects $A_{FB}(q^2 > q_0^2) > 0$ for B_d^0 mesons.

- The relation $A_{FB}[B_d^0](q^2) = -A_{FB}[\bar{B}_d^0](q^2)$ which follows from the CP-odd structure of A_{FB} and holds at the 10^{-3} level in the SM.

In addition to non-perturbative corrections due to the finite size of the b-quark mass, long-distance contributions arise from the process $b \to s\,(c\bar{c}) \to s\,\ell^+\ell^-$, with both resonant (mainly J/ψ and $\psi(2S)$) and continuum intermediate $(c\bar{c})$ states. The long-distance contributions are generated by the current-current operators Q_1 and Q_2. In the di-lepton invariant mass regions around the J/ψ and $\psi(2S)$ resonances, the decay is largely dominated by the long-distance

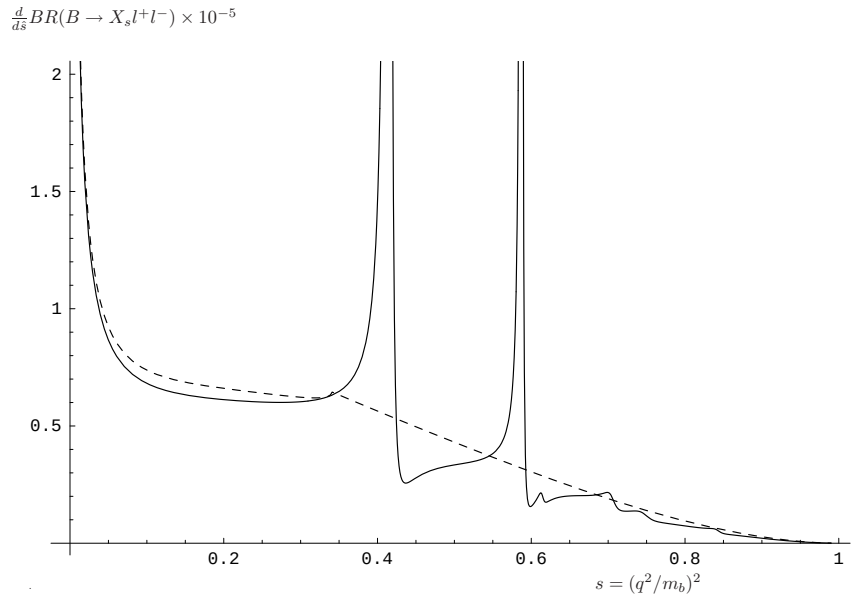

Figure 4.24: The di-lepton spectrum for inclusive $B \to X_s \ell^+ \ell^-$ decays within the SM. The dotted line denotes the NNLL perturbative calculation, while the full line includes an estimate of the long-distance $c\bar{c}$ effects. The figure is taken from Ref. [71]

contributions, while the short-distance contributions takes over away from the resonances. The branching fraction of the long-distance decay is about two to three orders of magnitude larger than the short-distance decay. For the calculation of the non-resonant branching fraction the long-distance processes have to be excluded because of a failure of quark-hadron duality. For most final states, the long-distance decay $B \to X_s\, J/\psi$ is well established (with the J/ψ usually seen via its decay to two muons), and the main interest lies in the observation of the short distance processes.

There are two windows for a reliable perturbative evaluation of short-distance physics in the di-lepton mass spectrum $q^2 = m^2_{l^+l^-}$: a low-q^2 region between 1 and 6 GeV/c^2 and a high q^2 region above 14.4 GeV/c^2.

The advantage of the low-q^2 region is the reliable q^2 spectrum and the small $1/m_b$ corrections. Here, the decay rate is sensitive to the interference of C_7 and C_9. The disadvantage however, is the difficulty to perform a fully inclusive measurement, since the cuts on the di-lepton energy and/or hadronic system are stringent. On the other hand, the main advantage of the high-q^2 region is an easier inclusive measurement, albeit at a lower rate. The branching ratio is mainly sensitive to $|C_{10}|^2$. However, $1/m_b$ corrections are here more important leading to a less reliable q^2 spectrum.

As a final result, the Wilson coefficients C_7, C_9 and C_{10} can be in principle completely determined in $B \to X_s \ell^+ \ell^-$ transitions. The measurement of the branching fraction of the radiative penguin decay strongly constraints the magnitude of the effective Wilson coefficients C_7 but not its sign. The latter could, however, be changed due to non-Standard Model contributions without changing the branching fraction of $B \to X_s \ell^+ \ell^-$. The determination of the sign of C_7 (as well as the sign of C_9 and C_{10}) in $B \to X_s \ell^+ \ell^-$ relies on precise mea-

surements of the distribution of the squared di-lepton momentum and the forward-backward asymmetry in these decays.

The inclusive decay $B \to X_s \ell^+ \ell^-$ were first measured by the Belle collaboration [72] and confirmed by the BaBar collaboration [73], using electrons (e) and muons (μ) as leptons in the final states. Both analysis methods are semi-inclusive, i.e., the final state X_s is obtained by summing up all final states with one kaon (K^+ or K^0_S) and up to four pions, of which one pion was allowed to be a π^0. This experimentally defined set of final state covers for approximately 53% of the full inclusive signal. If the contribution of the modes containing a K^0_L is taken to be equal to that containing a K^0_S, the missing states that remain unaccounted for represent $\sim 30\%$ of the total rate. Both experimental results are shown in Table 4.7 and are compatible with each other. The statistical significance of the observed $B \to X_s \ell^+ \ell^-$ signal is 5σ each. The branching fraction results are for a di-lepton mass range above $m_{\ell^+\ell^-} > 0.2$ GeV/c^2 and are interpolated in the J/ψ and ψ' regions that are removed from the analysis, assuming no interference with these charmonium states.

The measurements agree well with the Standard Model predictions calculated at NLO including long distance contributions. Table 4.7 gives an overview over the theoretical predictions and the measurements from the B factories for the branching fractions with a lower cut of 0.2 GeV/c^2 on the di-lepton invariant mass. With this requirement, the effect of the $q^2 = 0$ pole becomes insignificant, giving almost equal branching fractions for the electron and muon modes.

Table 4.7: Standard Model branching fraction predictions for the decays $B \to X_s \ell^+ \ell^-$ and experimental measurements for $m_{\ell^+\ell^-} > 0.2$ GeV/c^2.

	SM prediction $\mathcal{B} \times 10^6$	Belle [74] $\mathcal{B} \times 10^6$	Babar [73] $\mathcal{B} \times 10^6$
$\ell = e,\ \mu$	4.6 ± 0.8 [75]	$4.11 \pm 0.83\,^{+0.85}_{-0.81}$	$5.6 \pm 1.5 \pm 0.6 \pm 1.1$
$\ell = e$	6.89 ± 1.01 [76]	$4.04 \pm 1.30\,^{+0.87}_{-0.83}$	$6.0 \pm 1.7 \pm 0.7 \pm 1.7$
$\ell = \mu$	4.15 ± 0.70 [76]	$4.13 \pm 1.05\,^{+0.85}_{-0.81}$	$5.0 \pm 2.8 \pm 0.6 \pm 1.0$
$\ell = \tau$	0.26 ± 0.05 [77]	-	-

4.2.1 Exclusive B Decays

The decays $B \to K \ell^+ \ell^-$ and $B \to K^* \ell^+ \ell^-$, induced by $b \to s \ell^+ \ell^-$ transitions at quark level, are experimentally easier to measure than the inclusive processes $B \to X_s \ell^+ \ell^-$. The uncertainties on the SM predictions are dominated by the errors on hadronic form factors and are much larger than in corresponding inclusive decays. The SM predictions for different form factor calculations are shown in Tab. 4.8. The calculations by Ali *et al.* used the Light Cone-QCD sum rule approach, while Melikhov *et al.* used the quark model. As the branching fractions obtained with different form factor calculations differ, it is difficult to determine fundamental parameters of the SM, such as CKM elements, from exclusive decays.

Experimental results on exclusive decays are mainly coming from the B-factories. The Belle collaboration reported in 2002 the first observation of $B \to K \ell^+ \ell^-$ decays [80] and

Table 4.8: Branching fractions for $B \to K^{(*)}\,\ell^+\ell^-$ predicted in the framework of the Standard Model.

Mode	Predicted branching fraction $\mathcal{B} \times 10^6$	
	Ali *et al.* [78]	Melikhov *et al.* [79]
$B \to K\ell^+\ell^-$	$0.57^{+0.16}_{-0.10}$	0.42 ± 0.09
$B \to K^*e^+e^-$	$2.3^{+0.7}_{-0.4}$	1.4 ± 0.5
$B \to K^*\mu^+\mu^-$	$1.9^{+0.5}_{-0.3}$	1.0 ± 0.4

in 2003 the first observation of $B \to K^*\ell^+\ell^-$ decays [81]. Shortly after, also the BaBar collaboration reported on measurements of these exclusive decays [82]. In Tab. 4.9, the most recent measurements as taken from the HFAG averaging report [9] are summarized.

Table 4.9: Measurements of the branching fractions for $B \to K^{(*)}\,\ell^+\ell^-$.

Mode	Measured branching fraction $\mathcal{B} \times 10^6$	
	Belle	BaBar
$B \to K\ell^+\ell^-$	$0.55^{+0.075}_{-0.070} \pm 0.027$	$0.34 \pm 0.07 \pm 0.03$
$B \to K^*\ell^+\ell^-$	$1.65^{+0.23}_{-0.22} \pm 0.11$	$0.78^{+0.19}_{-0.17} \pm 0.12$

In addition to the measurements of branching fractions, the Belle collaboration reported in [83] the first measurement of the forward–backward asymmetry as a function of q^2 for $B \to K^*\ell^+\ell^-$. Within their limited statistical precision, the measured asymmetry is consistent with the SM as well as with both signs of C_7. In a more recent publication [84] the Belle collaboration now directly fits the ratio of Wilson coefficients, namely C_9/C_7 and C_{10}/C_7. The available data sample, corresponding to 386 million $B\bar{B}$ pairs, amounts finally to 113.6 ± 13 $B \to K^*\ell^+\ell^-$ decays. The Belle experimental finding is that the sign of $C_9 \cdot C_{10}$ has to be negative at a 95% CL. The sign of $C_7 \cdot C_{10}$ however, could not yet be determined.

Exclusive modes based on $b \to s\ell^+\ell^-$ quark transitions are also possible in other b-hadronic systems such as the B_s^0, $B_c^\pm$ mesons or in b-flavored baryons. A search for the decay $B_s^0 \to \phi\mu^+\mu^-$ is presently conducted at Tevatron. The SM value for $\mathcal{B}(B_s^0 \to \phi\mu^+\mu^-)$ was calculated in Ref. [85] excluding long-distance effects from charmonium resonances and found to be 1.6×10^{-6} with about 30% uncertainties mostly due to hadronic form factors. Including the long-distance contributions enhances the branching fraction of $B_s^0 \to \phi\mu^+\mu^-$ by almost a factor of three, depending on the exact modeling of the charmonium states [86].

The decay $B_s^0 \to \phi\mu^+\mu^-$ was also studied [87] in 2HDM models and possible enhancements in certain parameters regions depending on $\tan\beta$ and the mass of the charged Higgs boson are possible. Currently, the best experimental (preliminary) limit on this decay is obtained by the DØ experiment using 300 pb^{-1} of data [88]. The limit at a 90% C.L. is given by 3.2×10^{-6} if normalized to the world average value of the branching ratio of $B_s^0 \to J/\psi\phi$ decays. The $b \to s\mu^+\mu^-$ transitions in B_s^0 mesons lead also to $B_s^0 \to \eta(\eta')\mu^+\mu^-$ decays. The SM branching ratio was estimated [85] to be 3.1×10^{-7} only. Experimentally, this decay is

more complicated to measure due to the detection of the η meson which has γ's as decay products in the final state.

Finally, a new testing ground for $b \to s\ell^+\ell^-$ decays can be opened up by exclusive decay modes of b-baryons. A three-body decay of spin-1/2 baryons allows the construction of several new observables which are triple-products correlating spin and momenta of the final state particles. These observables offer a rich phenomenology for CP violating effects and new physics [89]. A good candidate decay to study is $\Lambda_b \to \Lambda\mu^+\mu^-$, which is experimentally completely unexplored. The decay has been theoretically studied in Ref. [90] and its branching fraction was calculated to be $2-3\times10^{-6}$. A strategy to search for this decay at Tevatron is outlined in chapter 5.

4.3 $B \to X_{s,d}\,\nu\bar{\nu}$

The decays $B \to X_{s,d}\,\nu\bar{\nu}$ are theoretically the cleanest decays in the field of rare B decays. However, they are experimentally difficult to access due to the non-detected neutrinos. A measurement of such type of decays is only possible at e^+e^- annihilation machines, where a well-defined initial state with beam energy constraint exists. It is rather hopeless to make any efforts at a hadron collider. The FCNC decays are dominated by the Z^0-penguin and box-diagrams involving top quark exchange. The main difference to $b \to s\ell^+\ell^-$ is that no photonic penguin is present. The decay $B \to X_{s,d}\,\nu\bar{\nu}$ has a very similar structure in the Hamiltonian than the celebrated golden channel $K_L \to \pi^0\nu\bar{\nu}$. Because of the absence of the photon penguin diagram, the non-perturbative contributions to $B \to X_{s,d}\nu\bar{\nu}$ are small and under full control. The SM calculation [91] yields for the branching ratio:

$$\mathcal{B}(B \to X_s\nu\bar{\nu})_{SM} = (3.7 \pm 0.7) \times 10^{-5} \tag{4.29}$$

The corresponding decay $B \to X_d\nu\bar{\nu}$ is suppressed by $|V_{td}/V_{ts}|^2$. It is well-known that a measurement of the ratio $\mathcal{B}(B \to X_d)\nu\bar{\nu})/\mathcal{B}(B \to X_s\nu\bar{\nu})$ represents theoretically the best way to directly measure $|V_{td}/V_{ts}|^2$, since there is almost no theoretical uncertainty.

The only existing inclusive bound on $B \to X_s\nu\bar{\nu}$ comes from an ALEPH analysis [92]:

$$\mathcal{B}(B \to X_s\nu\bar{\nu})_{exp} < 6.4 \times 10^{-4}\,(90\%\ \text{C.L.}) \tag{4.30}$$

This bound was already used to constrain new physics contributions [93] containing lepto-quarks and R_p-violating SUSY.

A limit on an exclusive decay mode has been presented in the channel $B^+ \to K^+\nu\bar{\nu}$ by Babar [94] and Belle [95]. The measurement of such a decay through the exclusive K^+ channel is experimentally the simplest, since there is only one measurable charged track out of the three-body final state, that characterize the signal. In order to identify the signal, the other B in the event has to be fully reconstructed and its tracks masked, so that the search signature consists then of only one charged kaon in the remaining event. Presently, the best upper limit from Belle is

$$\mathcal{B}(B \to K^+\nu\bar{\nu})_{exp} < 3.5 \times 10^{-5}\,(90\%\ \text{C.L.}) \tag{4.31}$$

which is only an order of magnitude higher than the predicted [96] value of

$$\mathcal{B}(B \to K^+\nu\bar{\nu})_{SM} < 3.8^{+1.2}_{-0.6} \times 10^{-6} \tag{4.32}$$

As usual, the exclusive channels are subject to larger hadronic uncertainties.

The experimental technique to reconstruct the other B and to exploit a well-defined $B\bar{B}$ system at the moment of production demonstrates one of the clear advantages of B factories over hadron colliders, if it comes to searches for partially invisible decays such as $B \to K^+\nu\bar{\nu}$.

4.4 $B^0_{d,s} \to \ell^+\ell^-$

The decays $B^0_{d,s} \to \ell^+\ell^-$ are dominated in the SM by the Z^0-penguin (also called vertical or annihilation penguin) and box diagrams involving top quark exchanges, as shown in Fig. 4.25. After the $B \to X_{d,s}\nu\bar{\nu}$ decays they are the theoretically cleanest rare B decays due to the simplicity of the hadronic matrix element.

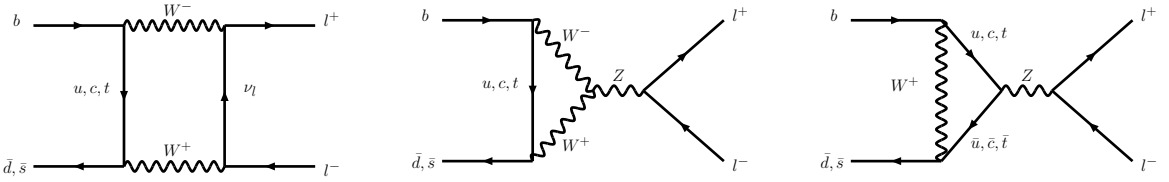

Figure 4.25: Decay processes contributing to $B_{s,d} \to \ell^+\ell^-$ in the Standard Model.

The effective Hamiltonian is given by

$$\mathcal{H}_{\text{eff}} = -\frac{4G_{\text{F}}}{\sqrt{2}} V^*_{tb}V_{tq}[C_{10}Q_{10} + C_S Q_S + C_P Q_P] \tag{4.33}$$

where q stands either for a s-quark for the B^0_s or a d-quark in the case of the B^0_d, and the two operators Q_S (scalar) and Q_P (pseudoscalar) are defined as

$$\begin{aligned} Q_S &= \frac{e^2}{16\pi^2}\bar{q}_{L\alpha} b_{R\alpha}(\bar{\ell}\ell) \\ Q_P &= \frac{e^2}{16\pi^2}(\bar{q}_{L\alpha} b_{R\alpha})(\bar{\ell}\gamma_5\ell). \end{aligned}$$

The diagrams in Fig. 4.25 contribute only to the Wilson coefficient C_{10}. There is no contribution from a photonic penguin because of the photon's pure vector coupling to leptons. In the SM, there are also contributions to the Wilson coefficient C_S from a SM Higgs penguin and to the Wilson coefficient C_P from the would–be neutral Goldstone boson penguin [97], but these terms in the decay amplitude are suppressed by a factor of m_b^2/M_W^2 relative to the dominant contributions and can be ignored. The terms C_S and C_P have been kept for completeness because they can be significant in some extensions of the SM due to the $\tan\beta$-enhanced Higgs-penguin contributions.

The Wilson coefficients are evaluated at a high energy scale $\sim \mathcal{O}(M_W)$ and then propagated to the low scale $\sim \mathcal{O}(m_b)$, where the hadronic matrix elements of the operators are evaluated. This propagation in general leads to QCD corrections enhanced by large logarithms of the ratio of the two scales, which must be re-summed. The operator Q_{10} has zero anomalous dimension because it is a $(V-A)$ quark current, which is conserved in the limit of vanishing quark masses. Therefore, the renormalisation group evolution of C_{10} is straightforward. The operators Q_S and Q_P have the same form as a quark mass term and thus have

the anomalous dimension of a quark mass. In the SM and many extensions, C_S and C_P are proportional to m_b. The running of these Wilson coefficients is therefore properly taken into account by replacing $m_b(M_W)$ with $m_b(m_b)$ in C_S and C_P.

Evaluating the hadronic matrix elements, the resulting branching ratio for $B^0_{q=s,d}$ is

$$\begin{aligned}\mathcal{B}(B^0_q \to \ell^+\ell^-) &= \frac{G_F^2\alpha^2 m^3_{B^0_q}\tau_{B^0_q} f^2_{B^0_q}}{64\pi^3}|V^*_{tb}V_{tq}|^2\sqrt{1-\frac{4m^2_\ell}{m^2_{B^0_q}}} \\ &\times\left[\left(1-\frac{4m^2_\ell}{m^2_{B^0_q}}\right)\left|\frac{m_{B^0_q}}{m_b+m_q}C_S\right|^2+\left|\frac{2m_\ell}{m_{B^0_q}}C_{10}-\frac{m_{B^0_q}}{m_b+m_q}C_P\right|^2\right], \qquad (4.34)\end{aligned}$$

where $\tau_{B^0_q}$ is the B^0_q lifetime, $f_{B^0_q}$ is the B^0_q decay constant, normalized according to the pion decay constant $f_\pi = 132$ MeV.

The SM decay amplitude is given by the Wilson coefficient

$$C_{10} = -Y(x_t)/\sin^2\theta_W = -4.2. \qquad (4.35)$$

The function $Y(x_t)$ represents the dependence on the top mass ($x_t = m_t^2/M_W^2$) and is given by

$$Y(x_t) = \eta_\gamma \cdot Y_0(x_t) \qquad (4.36)$$

$$Y_0(x_t) = \frac{x_t}{8}\left[\frac{x_t-4}{x_t-1}+\frac{3x_t}{(x_t-1)^2}\ln x_t\right] \qquad (4.37)$$

where η_Y summarizes the NLO corrections with $\eta_Y \approx 1.012$.

Purely leptonic decays are helicity-suppressed by a factor m_l^2, as, by conservation of angular momentum, the spin-less B^0 forces both the lepton and the anti-lepton to be in the same helicity state. This means that the largest SM branching ratio is obtained for the leptonic decay into τ's. It should be noted that the decays $B^0_{d,s} \to \tau^+\tau^-$ are unique to the B system and do not appear in K decays at all. This might be a particularly interesting feature if enhanced couplings to third generation fermions appear.

The leading order of the Z-penguin and box diagram contribution in the SM to the leptonic decay was first calculated in Ref. [98] and then in Ref. [99] including QCD corrections. The latest and presently most precise SM calculations [100][3] for the various branching fractions are given in Table 4.10, where the uncertainties are dominated by non-perturbative uncertainties of the hadronic matrix element. The calculation of Ref. [100] has reduced the theoretical uncertainty of the SM prediction compared to earlier calculations considerably. However, it is important to note that specific input values of $\Delta M_d = (0.503 \pm 0.006)/\text{ps}$ and $\Delta M_s = (18.0 \pm 0.5)/\text{ps}$ were used. The most recent experimental upper limits are given in Table 4.11.

Table 4.11 contains a limit for $B^0_s \to \tau^+\tau^-$. It should be noted that this bound is a byproduct of the LEP I search for $B^- \to \tau^-\bar{\nu}$ and was achieved under certain assumptions. There exists no direct experimental limit for this B^0_s decay, while a limit on the corresponding $B^0_d \to \tau^+\tau^-$ decay was already obtained [104] at e^+e^- machines.

Since the ratio of the decay constants $f_{B^0_d}$ and $f_{B^0_s}$ can be calculated reliably by non-perturbative methods such as lattice QCD, the ratio

[3] In Ref. [100] only the SM prediction for the decay $B^0_{d,s} \to \mu^+\mu^-$ is given. The SM predictions for the other leptonic decays $B_{d,s} \to \ell^+\ell^-$ have been calculated in a similar way using the master equation of Ref. [100].

Table 4.10: Standard Model branching fraction predictions for the decays $B^0_{d,s} \to \ell^+\ell^-$ according to the master equation of Ref. [100].

	$\mathcal{B}(B^0_d \to \ell^+\ell^-)$	$\mathcal{B}(B^0_s \to \ell^+\ell^-)$
$\ell = e$	$(2.40 \pm 0.34) \times 10^{-15}$	$(8.15 \pm 1.29) \times 10^{-14}$
$\ell = \mu$	$(1.00 \pm 0.14) \times 10^{-10}$	$(3.42 \pm 0.54) \times 10^{-9}$
$\ell = \tau$	$(2.90 \pm 0.41) \times 10^{-8}$	$(9.86 \pm 1.55) \times 10^{-7}$

Table 4.11: Experimental upper limits for the decays $B^0_{d,s} \to \ell^+\ell^-$ at a 90% CL.

	$\mathcal{B}(B^0_d \to \ell^+\ell^-)$	$\mathcal{B}(B^0_s \to \ell^+\ell^-)$
$\ell = e$	$< 6.1 \times 10^{-8}$ [101]	$< 5.4 \times 10^{-5}$ [102]
$\ell = \mu$	$< 3.2 \times 10^{-8}$ [103]	$< 1.2 \times 10^{-7}$ [103]
$\ell = \tau$	$< 3.1 \times 10^{-3}$ [104]	$< 5.0 \times 10^{-2}$ [93]

$$\frac{\mathcal{B}(B^0_s \to \mu^+\mu^-)}{\mathcal{B}(B^0_d \to \mu^+\mu^-)} = \frac{\tau(B^0_s) m_{B^0_s} f^2_{B^0_s} |V_{ts}|^2}{\tau(B^0_d) m_{B^0_d} f^2_{B^0_d} |V_{td}|^2} \tag{4.38}$$

will provide an important and very useful measurement of $|V_{ts}|^2/|V_{td}|^2$ with a smaller theoretical uncertainty than the individual branching ratio measurements. Due to the CKM-suppression factor of $|V_{td}|^2/|V_{ts}|^2 \approx 0.04$, the B^0_d-decays are expected to be smaller than the corresponding B^0_s-decays.

The limits on the branching ratios $B^0_d \to \ell^+\ell^-$ and $B^0_s \to \ell^+\ell^-$ can be compared to the values expected in the SM. Currently the 90% CL limit on $B^0_s \to \mu^+\mu^-$ is only a factor of 35 larger than the SM branching ratio, while the limit on $B^0_d \to \mu^+\mu^-$ is approximately 320 times larger. A search for electrons in the final state of the leptonic $B^0_{d,s}$ decay does not even come close to the SM value, neither with existing nor with future experimental facilities. Due to the abundance of B^0_s mesons at hadron colliders and the much easier experimental identification of muons than of taus, it is rather obvious why a search for the decay $B^0_s \to \mu^+\mu^-$ is presently the preferred choice of probing the SM. More details to the experimental search strategies are presented in chapter 5.

4.4.1 Enhancements due to New Physics in $B^0_{d,s} \to \ell^+\ell^-$ Decays

The helicity suppression of $B^0_{d,s} \to \ell^+\ell^-$ gives the leptonic decays a special and designated role in the search for new physics, because it is very sensitive to new helicity-flipping interactions from scalar and pseudoscalar FCNC interactions that appear in models with an extended Higgs-sector, like in the 2HDM and in the MSSM at high $\tan\beta$ and are mediated through diagrams of the Higgs penguin. In other rare B decays that are not helicity-suppressed

such scalar FCNC interactions are smaller. This unique feature of $B^0_{d,s} \to \ell^+\ell^-$ is vastly emphasized in the recent literature [105] characterizing the leptonic B decay as a gold-plated mode whose decay rate can be significantly altered if new physics is present. Therefore, an attempt is made to give an overview of the new physics sensitivity of $B^0_{d,s} \to \ell^+\ell^-$.

For most of the models that are considered here, some estimations on the decay rates of $B^0_{d,s} \to \ell^+\ell^-$ for certain model parameters were done in literature. It should be also stressed that the decay rate is not the only interesting observable that is sensitive to new physics contributions. In Ref. [106] a lepton polarization asymmetry from $B^0_{d,s} \to \ell^+\ell^-$ decays is constructed that is a good probe of scalar and pseudoscalar-type interactions as well and can be used for further investigations once the leptonic decay is measured.

General type-II 2HDM:
In the limit of large $\tan\beta$ the 2HDM contributions for the decay $B_{d,s} \to \ell^+\ell^-$ are significant. The Wilson coefficients C_S and C_P receive contributions from the box and penguin diagrams involving W and H^+ bosons. There are also contributions due to fermion self-energy diagrams with a neutral Higgs boson exchange. In this model there are no new contributions to C_{10}, which therefore retains its SM value. The obtained Wilson coefficients in the type-II 2HDM are

$$C_S = C_P = \frac{m_l}{2M_W^2} \tan^2\beta \frac{\log r}{r-1} \tag{4.39}$$

with $r = M^2_{H^+}/m_t^2$. The dependence on the masses of the neutral Higgs bosons from penguin and self-energy diagrams drops out without invoking any relations between the mixing angle and the Higgs masses.

The branching fraction at high $\tan\beta$ depends then only on two 2HDM parameters, the charged Higgs mass M_{H^+} and $\tan\beta$, with the branching fraction growing like $\tan^4\beta$ [107]. The predicted value for $\mathcal{B}(B_s \to \mu^+\mu^-)$ as a function of M_{H^+} and for various values of $\tan\beta$ is shown in Fig. 4.26. For large $\tan\beta$ and small M_{H^+}, the 2HDM contribution dominates, enhancing the branching fraction significantly. As the 2HDM contribution becomes smaller due to decreasing $\tan\beta$ or increasing M_{H^+} the branching fraction drops, eventually falling below the SM prediction due to destructive interference. The type-II 2HDM contribution to $B^0_s \to \mu^+\mu^-$ is somewhat complementary to contributions to $b \to s\gamma$, because of a different $\tan\beta$ dependence. While the former depends very strongly on $\tan\beta$, the latter is almost independent.

Minimal Supersymmetry MSSM:
At large $\tan\beta$ the leading supersymmetric contribution to the $B^0_s \to \mu^+\mu^-$ decay from the Higgs-penguin depends mainly on a few parameters, namely the CP-odd Higgs mass m_A, $\tan\beta$, the soft supersymmetric breaking trilinear coupling and the masses of the two scalar superpartners of the top quark. The Wilson coefficients C_S and C_P of Eq. 4.34, that are completely neglected in the SM have to be taken into account because of the MSSM Higgs penguin. The scalar and pseudoscalar Wilson coefficients $C_{S,P}$ grow like $\tan^3\beta$ and are roughly $(m_b^2/M_W^2)\tan^3\beta$ times bigger than C_{10} and therefore dominate for large values of $\tan\beta$. Other electroweak SUSY box and Z-penguin contributions grow with at most two powers of $\tan\beta$ and are thus subdominant in this region. These considerations give

$$\mathcal{B}(B^0_s \to \mu^+\mu^-) \propto V_{tb}^2 V_{ts}^2 m_\mu^2 m_t^2 m_b^2 \frac{\tan^6\beta}{m_A^4} \tag{4.40}$$

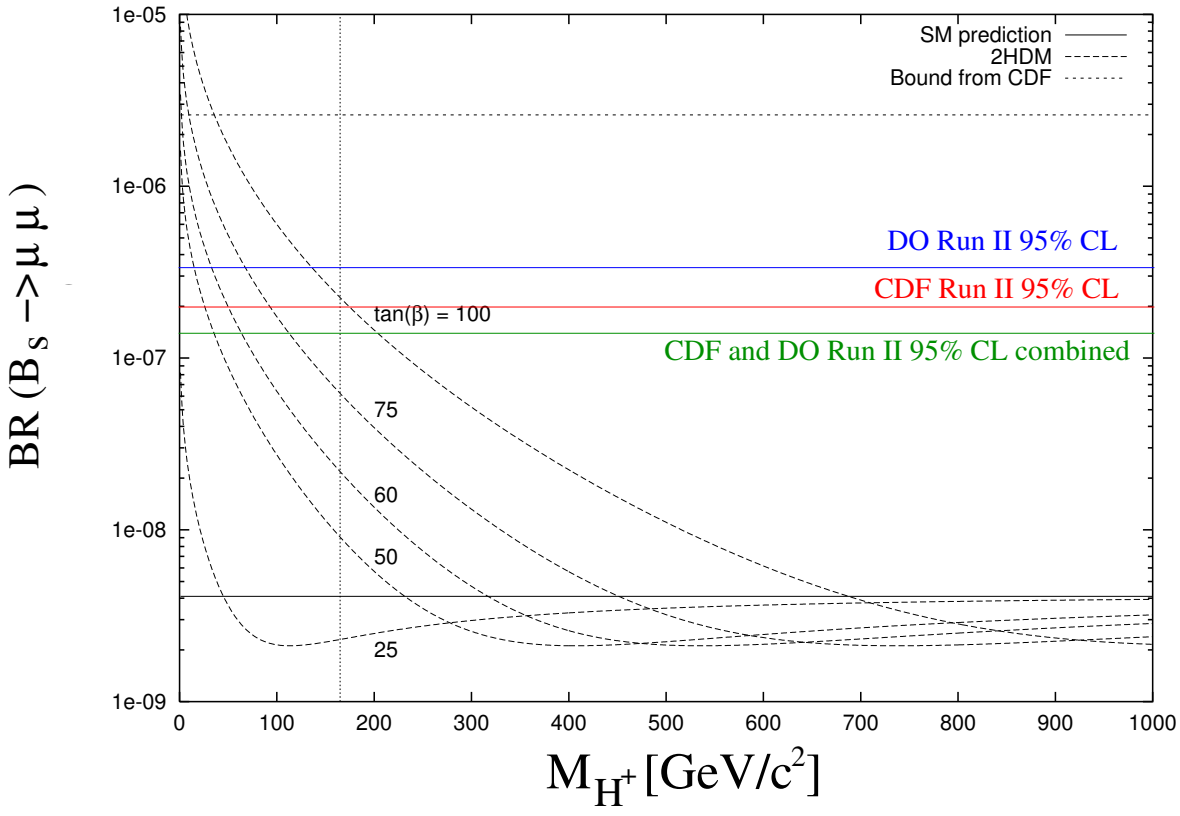

Figure 4.26: The branching fraction $\mathcal{B}(B_{s^0} \to \mu^+\mu^-)$ in the 2HDM as a function of the charged Higgs mass M_{H^+} and various values of $\tan\beta$ [107]. For comparison the SM prediction and the current experimental limits are shown. The vertical line is the lower bound on M_{H^+} that is obtained in the type-II 2HDM from $b \to s\gamma$ decays.

which could lead to significant enhancements [108] compared to the SM, even if the MSSM with minimal flavor violation (MFV) is considered in which the CKM matrix is the only source of flavor violation. As the mass of the pseudoscalar Higgs mass m_A increases, $\mathcal{B}(B_s^0 \to \mu^+\mu^-)$ can not exceed certain values. In a MSSM parameter scan [109] an upper limit for $\mathcal{B}(B_s^0 \to \mu^+\mu^-)$ was determined and parameterized as

$$\mathcal{B}(B_s^0 \to \mu^+\mu^-) < 5 \times 10^{-7} \left(\frac{\tan\beta}{50}\right)^6 \left(\frac{650\ \text{GeV}}{m_A}\right)^4 + 1.0 \times 10^{-8} \qquad (4.41)$$

Hence, an observation of $B_s^0 \to \mu^+\mu^-$ would then immediately yield an upper bound on the heaviest mass in the MSSM Higgs sector for all $\tan\beta \leq 50$ if MFV applies.

The $B_s^0 \to \mu^+\mu^-$ decay was also studied [110] in several constrained SUSY models, in which the soft supersymmetry breaking mechanism is further specified such that only a few free parameters are left to describe the complete phenomenology. For instance, in minimal gauge mediated SUSY breaking models (mGMSB) and minimal anomaly-mediated SUSY breaking model (mAMSB) there are no massive contributions to $B_s^0 \to \mu^+\mu^-$ over a wide parameter range. An observation of the decay with $\mathcal{B}(B_s^0 \to \mu^+\mu^-)$ at about 2×10^{-8}

would immediately rule out most classes of such models, if constraints from $B \to X_s\gamma$ and direct search bounds on sparticles and Higgs bosons are additionally imposed. A search for $B_s^0 \to \mu^+\mu^-$ decays is able to provide important information on the SUSY breaking mediation mechanism, independent of results from direct SUSY particle searches at high energy colliders.

Minimal Supergravity mSUGRA:
The $B_{d,s}^0 \to \mu^+\mu^-$ decay was studied in mSUGRA models by various authors in Refs. [111]. For not too large values of M_0, $M_{1/2} \leq 500$ GeV/c^2 the branching fraction for $B_s^0 \to \mu^+\mu^-$ can be approximated by

$$\mathcal{B}(B_s^0 \to \mu^+\mu^-) \approx 10^{-6} \cdot \tan^6\beta \frac{M_{1/2}^2 \mathrm{GeV}^4}{(M_{1/2}^2 + M_0^2)^3} \tag{4.42}$$

outside the vicinity of $M_{1/2} = 0.4M_0$. A parameter scan in mSUGRA for $\mathcal{B}(B_s^0 \to \mu^+\mu^-)$ is shown in Fig. 4.27. Especially for $\mu < 0$ the branching fraction in mSUGRA models can become very large.

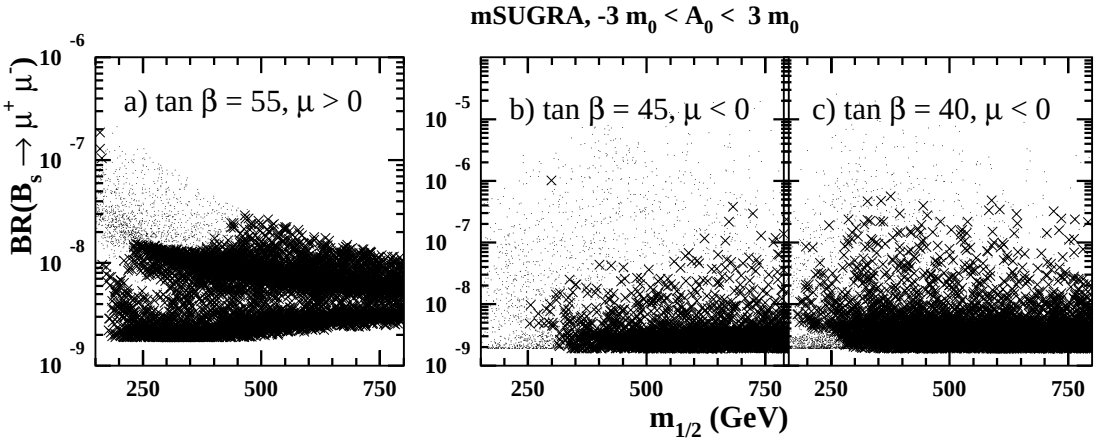

Figure 4.27: The branching fraction $\mathcal{B}(B_s^0 \to \mu^+\mu^-)$ for a scan in mSUGRA parameter space. Each cross (dot) indicates a model where $\mathcal{B}(b \to s\gamma)$ is within (outside) the experimentally allowed region. The left pot shows the mSUGRA scan for $\mu > 0$, while the right two graphs are for $\mu < 0$. The figure is taken from Ref. [112].

The decay $\mathcal{B}(B_s \to \mu^+\mu^-)$ features in mSUGRA a very interesting correlation with $(g-2)_\mu$, the anomalous magnetic momentum of the muon. An enhancement of the leptonic decay is correlated with a sizeable positive shift of $(g-2)_\mu$ with respect to its SM value. Such an excess has been actually observed [113]. Taking into account e^+e^- collision data in order to calculate the $\pi^+\pi^-$ spectral functions for the hadronic vacuum polarization for the magnetic moment of the muon, the measurement corresponds to a 2.6σ deviation [114] from the SM predicted value. In the context of mSUGRA interpretation, this anomaly favors $\mu > 0$.

It was shown that both $\mathcal{B}(B_s^0 \to \mu^+\mu^-)$ and the deviation from $(g-2)_\mu$ to its SM value grow with $\tan\beta$ and decrease with increasing $M_{1/2}$ in mSUGRA. If this explanation for the

$(g-2)_\mu$ excess holds and is due to a large value of $\tan\beta \sim 50$, one would expect $\mathcal{B}(B_s^0 \to \mu^+\mu^-)$ to be enhanced as well, giving possibly rise to an observable signal at Tevatron. The enhancement however, is diminished for smaller values of $M_{1/2}$ and moderate value of $\tan\beta$.

Dark Matter Implications of $\mathcal{B}(B_s^0 \to \mu^+\mu^-)$:
One very attractive feature of R_p conserving SUSY is that its lightest supersymmetric particle (LSP) - in supergravity models assumed to be the neutralino - is a viable candidate for a weakly interacting massive particle (WIMP), i.e., a dark matter candidate. Model-independent WIMP searches are carried out by trying to directly detect elastic WIMP-nucleon scattering inside a large target volume.

Neutralinos can annihilate through a variety of channels, including through the exchange of CP-even or odd Higgs bosons, charginos, neutralinos, sfermions and gauge bosons depending on model assumptions. At high $\tan\beta$ and for not too heavy Higgs masses, the neutralino annihilation through s-channel Higgs exchange into fermion pairs is likely the dominant contribution for the total dark matter annihilation cross section. This cross section might be used to calculate the thermal relic dark matter abundance $\Omega_\chi h^2$ due to neutralinos present today. This calculated supersymmetric relic density can then be contrasted with precision data [115] from the WMAP satellite that confirmed with greater accuracy the cosmological model and hence the present dark matter density of the universe.

It was shown in Ref. [116] that there is a correlation between the neutralino dark matter scattering cross section of neutralinos on nucleons $\sigma_{\tilde{\chi}p}$ and $B_s^0 \to \mu^+\mu^-$ within supergravity models. Contributions to the inelastic scattering between neutralinos and nucleons arise from t-channel Higgs boson and s-channel squark exchanges. In the large $\tan\beta$ limit, heavy neutral Higgs-boson exchange becomes important again. As in the $B_s^0 \to \mu^+\mu^-$ decay, the neutralino annihilation rate increases towards large $\tan\beta$ and decreases towards larger values of m_A. The enhancement of $\sigma_{\tilde{\chi}p}$ is roughly linear in $\tan\beta$.

On the left side in Fig. 4.28, the correlation between $\sigma_{\tilde{\chi}p}$ and $\mathcal{B}(B_s^0 \to \mu^+\mu^-)$ within the mSUGRA model is shown for various values of the universal Higgs mass parameter and for $\tan\beta = 10$, 35 and 55, respectively. For large $\tan\beta$, there is a strong correlation between the two observables.

In supergravity extensions of mSUGRA the restriction on the universal mass parameter for the Higgs sector can be further relaxed by assuming different masses for the two Higgs doublets H_u and H_d:

$$m_{H_u}^2 = m_0^2\ (1+\delta_{H_u}), \quad m_{H_d}^2 = m_0^2\ (1+\delta_{H_d}), \tag{4.43}$$

The correlation between $\sigma_{\tilde{\chi}p}$ vs. $\mathcal{B}(B_s^0 \to \mu^+\mu^-)$ for two parameter sets of δ_{H_u} and δ_{H_d} is shown in the center and on the right side of Fig. 4.28. The current experimental limit on $\mathcal{B}(B_s^0 \to \mu^+\mu^-)$ already puts a strong constraint on $\sigma_{\tilde{\chi}p}$ in the large $\tan\beta$ region, even stronger than the direct search limit from CDMS, if non-universal supergravity models are assumed.

The implication of constraints from $B_s^0 \to \mu^+\mu^-$ at large $\tan\beta$ on the upward going muon flux from dark matter annihilation at the core of the sun or earth was studied in Ref. [118] within the framework of supergravity models. One of the promising channels for an indirect neutralino detection are energetic neutrinos that are produced from annihilation processes of trapped neutralinos in sun or earth. Those annihilation neutrinos can pass through sun or earth and could be detected in neutrino telescopes through their conversion

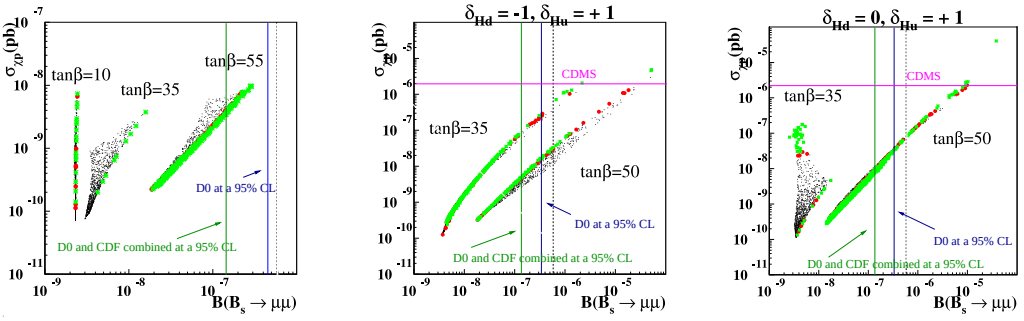

Figure 4.28: $\sigma_{\tilde{\chi}p}$ vs. $\mathcal{B}(B_s^0 \to \mu^+\mu^-)$ within mSUGRA with universal Higgs mass parameters (left side) and non-universal Higgs mass parameters (center and right side) for various values of $\tan\beta$ [116]. The black dots are for $\Omega_\chi h^2 \geq 0.13$ (greater than 2σ of the preferred density of WMAP data), red dots for $0.095 \leq \Omega_\chi h^2 \leq 0.13$ (within 2σ of WMAP data) and green dots for $\Omega_\chi h^2 \leq 0.095$ (less than 2σ of WMAP data). Also indicated is the combined Tevatron limit [103] as vertical line. The experimental bound on $\sigma_{\tilde{\chi}p}$ from CDMS [117] is also shown in the center and right plot.

to muons via charged-current interactions with material near the detector. There are several experiments that published upper limits on upward-going muon fluxes such as Super-K [119] and Amanda [120] and further detectors such as Antares, IceCube and Nestor are planned and being constructed.

Figure 4.29 shows the expected muon flux result from earth and sun for a supergravity parameter scan with non-universal Higgs mass parameters for $\tan\beta = 35$ and $\tan\beta = 50$. The red points are excluded by the current upper limit of $B_s^0 \to \mu^+\mu^-$. The present upper limit from Super-K and the expected sensitivity of Amanda-II is also shown. In particular at large $\tan\beta$, there is a strong constraint from the existing upper limit of $B_s^0 \to \mu^+\mu^-$ on the upward muon flux, if non-universal supergravity models are considered. The impact of the upper bound of the leptonic B decay becomes more significant than the upper limits on the muon flux from Super-K and Amanda-II.

In conclusion, an enhancement of the decay $B_s^0 \to \mu^+\mu^-$ at high $\tan\beta$ is closely linked to a larger neutralino dark matter cross section within a large class of supergravity models. The investigation of the leptonic decay provides valuable information to supersymmetric dark matter complementary to direct search experiments. Within extended supergravity models at large $\tan\beta$, the implications of bounds on $B_s^0 \to \mu^+\mu^-$ on the direct detection of dark matter through elastic WIMP-nucleus collisions and on upward-going neutrino fluxes are significant.

The Correlation between ΔM_s and $B_s^0 \to \mu^+\mu^-$ in MFV SUSY:

The Higgs penguin generates at large $\tan\beta$ new FCNC transitions in the MSSM. The same interactions are also effective in $B_s^0 - \bar{B}_s^0$ mixing, as was pointed out in Ref. [121]. It leads to an increase of $\mathcal{B}(B_s^0 \to \mu^+\mu^-)$ while decreasing the $B_s^0 - \bar{B}_s^0$ mass difference ΔM_s relative to the SM expectation if MFV models are considered. This correlation was studied and analyzed in Ref. [121] and is particularly interesting, since both quantities are becoming more and more constrained at Tevatron over the next years.

In MSSM models that obey MFV, the mass difference ΔM_s of the B_s^0 mesons can be

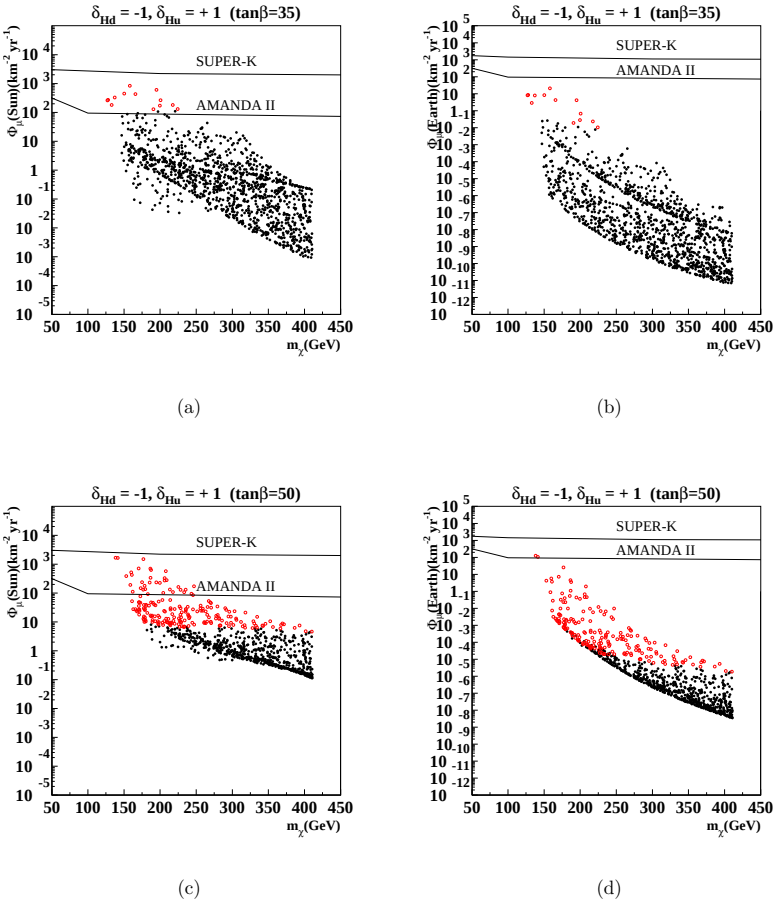

Figure 4.29: The muon flux from the sun (left two plots) and from the earth (right two plots) as function of the neutralino mass m_χ in non-universal Higgs mass scenarios with $\delta_{H_d} = -1$, $\delta_{H_u} = +1$ and $\tan\beta = 35$ and $\tan\beta = 50$. The red points are excluded by the current upper limit of $B_s^0 \to \mu^+\mu^-$. The figure is taken from Ref. [118].

altered from its SM value ΔM_s^{SM} by three contributions: box-diagrams with top quark and charged Higgs bosons, box diagrams with charginos and squarks, and finally contributions from double Higgs penguins. At large $\tan\beta$ the double Higgs penguin ΔM_s^{DP} giving $\mathcal{O}(\tan^4\beta)$ corrections is the dominant modification to ΔM_s, but charged Higgs box contributions can be also significant. The correlation between ΔM_s and $B_s^0 \to \mu^+\mu^-$ is given [121] by:

$$\mathcal{B}(B_s^0 \to \mu^+\mu^-) = 10^{-6} \times \left(\frac{\tan\beta}{50}\right)^2 \left(\frac{200\ \text{GeV/c}^2}{M_A}\right) \left(\frac{|\Delta M_s^{DP}|}{2.12\ \text{ps}^{-1}}\right). \tag{4.44}$$

The correlation is shown in Fig. 4.30.

If the experimental value for ΔM_s will turn out to be larger than the SM value, then there are no substantial enhancements for $\mathcal{B}(B_s^0 \to \mu^+\mu^-)$ in SUSY models with MFV possible. If ΔM_s is measured to be less than the SM prediction, then $\mathcal{B}(B_s^0 \to \mu^+\mu^-)$ is also increased.

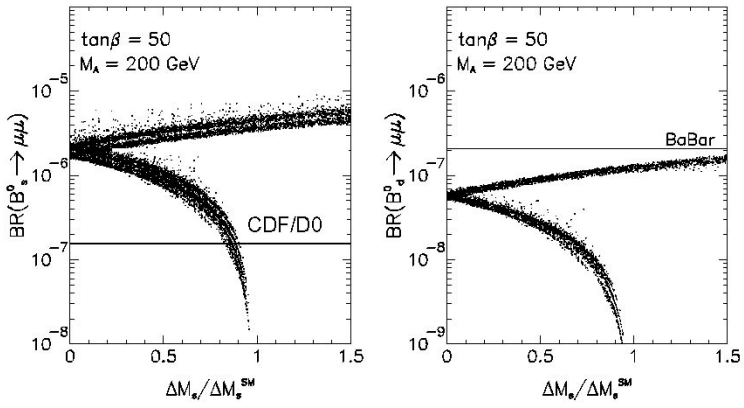

Figure 4.30: Correlation plot between $\Delta M_s/\Delta M_s^{SM}$, i.e., the change of ΔM_s relative to its SM value and $B^0_{d,s} \to \mu^+\mu^-$ in the MSSM with MFV for $\tan\beta = 50$ and $M_A = 200$ GeV/c^2. The left (right) graph shows $B^0_s \to \mu^+\mu^-$ ($B^0_d \to \mu^+\mu^-$) and the current combined Tevatron (Babar) limit. The upper branch of points would correspond to a special parameter space region in MSSM, that is already ruled out by Tevatron.

General Flavor Violation and $B^0_s \to \mu^+\mu^-$:
General flavor violating (GFV) MSSM allows additional sources of flavor and CP violation beyond the SM CKM matrix leading to a highly non-trivial flavor structure in the quark sector. Simple relations such as $\mathcal{B}(B^0_s \to \mu^+\mu^-)/\mathcal{B}(B^0_d \to \mu^+\mu^-) \approx V^2_{ts}/V^2_{td}$ do not hold anymore in GFV models. The correlation between $\mathcal{B}(B^0_s \to \mu^+\mu^-)$ and ΔM_s is also more complex than in models with MFV. GFV models can be constrained from CP violation measurements or from the measurement of any deviation in an observable that relates $b \to s$ to $b \to d$ transitions via the CKM matrix elements of the SM. Together with $b \to s\gamma$ constraints and the limit on ΔM_s, the existing limit of $\mathcal{B}(B^0_s \to \mu^+\mu^-)$ has already been used to place bounds on GFV parameters [122]. In this study, additional flavor violation δ^d_{XY} (with X, $Y = L$, R) in the soft SUSY breaking Lagrangian was parameterized in the down-type quark matrix. Figure 4.31 shows the limits on the flavor-violating $\delta^d_{X,Y}$ parameters vor varying $\tan\beta$. As expected, the decay $B^0_s \to \mu^+\mu^-$ starts to constrain GFV models at large $\tan\beta$. However, in case of $\delta^d_{R,R}$ an impact of $B^0_s \to \mu^+\mu^-$ is already notable at lower values of $\tan\beta$ of about 30.

Grand Unified Theories:
The minimal SO_{10} supersymmetric model based on the SO(10) Lie group [123] is one candidate for a grand unified theory (GUT). In this model, quarks and leptons and their supersymmetric partners of one family reside in the **16** dimensional representation, while the two Higgs doublets of the MSSM reside in one **10** dimensional representation. It is assumed that the coupling obey a hierarchical mass matrix for the first two generations and their mixing with the third generation, due to effective higher dimensional operators. Soft SUSY breaking parameters are a universal gaugino mass $M_{1/2}$, a universal squark and slepton mass

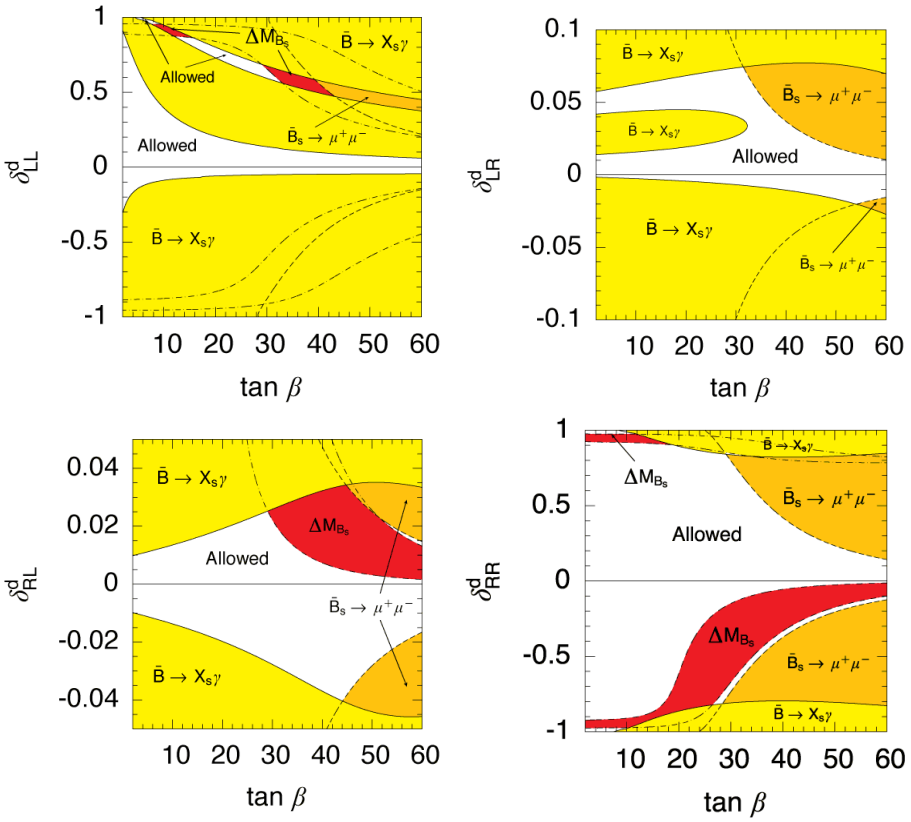

Figure 4.31: Contour plot showing the current limits on some GFV parameters $\delta^d_{X,Y}$ as function of $\tan\beta$ and for a mass of the pseudo-scalar Higgs of $m_A = 500$ GeV/c^2. The constraints from the observables $B \to X_s\gamma$, ΔM_s and $B^0_s \to \mu^+\mu^-$ are indicated. The figure is taken from Ref. [122].

m_{16}, a universal scalar Higgs mass m_{10}, and a universal parameter A_0. In addition there is the soft SUSY breaking Higgs mass parameter μ. All these parameters are independent and low-energy measurements can be used to constrain these parameters. In the minimal SO_{10} model of Ref. [123], the cosmological dark matter density $\Omega_\chi h^2$ and $\mathcal{B}(B^0_s \to \mu^+\mu^-)$ both depend on m_A and $\tan\beta$ and are used to further derive model constraints.

In Fig. 4.32 contours of constant χ^2-values for $m_{16} = 3$ TeV/c^2 and $m_A = 500$ GeV/c^2 (left plot) and $m_A = 700$ GeV/c^2 (right plot) obtained from a parameter scan are shown. The red (light shaded) regions are excluded by $m_{\chi^+} < 104$ GeV/c^2 (below and to the left of the solid black curve), $m_h < 111$ GeV/c^2 (on the right) and by $\Omega_\chi h^2 > 0.129$. To the right of the thick broken black line one has $m_h < 114.4$ GeV/c^2 which is the LEP exclusion limit on the Higgs mass. The green (darkest shaded) band corresponds to the preferred 2σ range $0.094 < \Omega_\chi h^2 < 0.129$, while the white regions below it correspond to $\Omega_\chi h^2 < 0.094$. The region excluded by the DØ experimental bound on $\mathcal{B}(B^0_s \to \mu^+\mu^-) < 5.0 \times 10^{-7}$ at 95% C.L. is marked in dark blue (dark shaded), while the region affected by the new preliminary CDF bound $\mathcal{B}(B^0_s \to \mu^+\mu^-) < 2.0 \times 10^{-7}$ at 95% is marked in light blue (light shaded). Contours

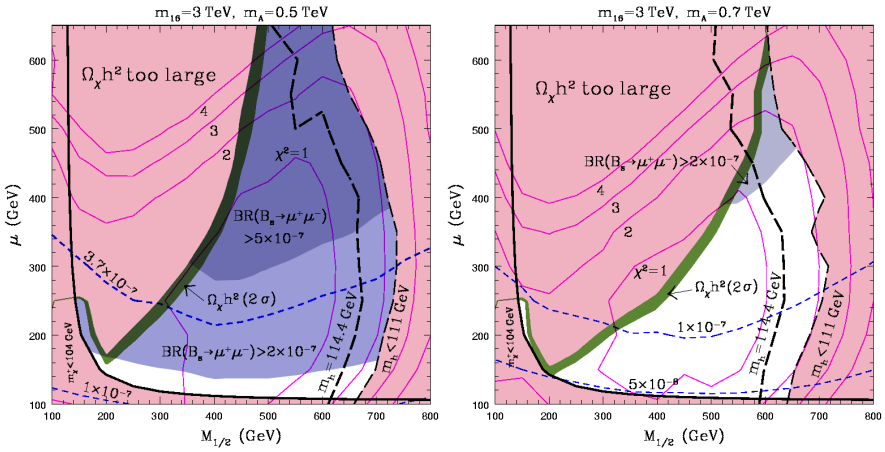

Figure 4.32: Contours of constant χ^2 for $m_{16} = 3$ TeV/c^2 and $m_A = 500$ GeV/c^2 (left side) and 700 GeV/c^2 (right side), indicating the allowed region for $B_s^0 \to \mu^+\mu^-$ [123].

of constant $\mathcal{B}(B_s^0 \to \mu^+\mu^-)$ are given by the blue dashed lines.

The branching ratio $\mathcal{B}(B_s^0 \to \mu^+\mu^-)$ depends on the value of the CP-odd Higgs mass m_A and scales as m_A^{-4}. For $m_A = 500$ GeV/c^2 and for allowed values of $\Omega_\chi h^2$ (Fig. 4.32 (left)) the branching ratio $\mathcal{B}(B_s^0 \to \mu^+\mu^-)$ is below the published DØ bound, but is almost excluded by the combined Tevatron result [103]. Increasing the CP-odd Higgs mass to $m_A = 1.25$ TeV/c^2 shifts the allowable $B_s^0 \to \mu^+\mu^-$ decay rate down to $\mathcal{B}(B_s^0 \to \mu^+\mu^-) > 10^{-8}$.

It is an interesting feature of the minimal SO_{10} model of Ref. [123], that large regions of parameter space lead to predictions of observable rates for $B_s^0 \to \mu^+\mu^-$ at the Tevatron. The projected Tevatron sensitivity for $B_s^0 \to \mu^+\mu^-$ at the end of Run II will be large enough to either find evidence or rule out most of the parameters space of the minimal SO_{10} model.

Other Models of New Physics:

If R_p is broken, SUSY contributions to $B_s^0 \to \mu^+\mu^-$ appear at tree-level and might lead to considerably large effects, even if $\tan\beta$ is small. In Ref. [124] limits on R_p violating couplings from the absence of FCNC decays of B mesons were derived.

The decay $B_s^0 \to \mu^+\mu^-$ was also analyzed [125] in extended technicolor models. In technicolor models new scalars are introduced that couple the technicolor condensate to fermions. Additional contributions to $B_s^0 \to \mu^+\mu^-$ arise from charged scalar technipions in the Z penguin diagram modifying the Wilson coefficient C_{10}. Enhancements of $\mathcal{B}(B_s^0 \to \mu^+\mu^-)$ of up to a factor of 5 relative to the SM value are still possible.

The impact on rare B and K decays due to the addition of one universal extra dimension to the SM was analyzed in Ref. [126]. Generally, universal extra dimension models allow the SM fields to propagate in all available dimensions. The simplest extension of the SM adds then one universal extra dimension with only one additional compactification parameter $1/R$. The decay $B_s^0 \to \mu^+\mu^-$ will then proceed via the same box and penguin diagrams as in the SM. However, each boson line will now involve several Kaluza-Klein modes. Adding only one universal extra dimension at a compactification scale of $1/R = 200$ GeV leads to an enhancement of $B_s^0 \to \mu^+\mu^-$ of about 70%, more than for other rare B and K decays that

were studied. If non-universal extra-dimensions are allowed, the calculations of Kaluza-Klein towers for B decays diverge [127].

4.5 Further Radiative B Decays

The $B^0_{d,s} \to \gamma\gamma$ decays are double radiative decays with the experimental signature of only two photons in the final state. The decay on quark level is described by $b \to s\,(d)\gamma\gamma$ transitions, which are very closely connected to the $b \to s\,(d)\gamma$ decay. In fact, the effective Hamiltonians of the two decays are identical with the magnetic penguin operator Q_7 being the most important one. The leading contribution to $B^0_{d,s} \to \gamma\gamma$ comes then from $b \to s\,(d)\gamma$ transitions with an additional second photon emitted from the s-quark constituent. The decay mode offers an interesting study of non-trivial QCD dynamics related to the decaying B meson together with a completely non-hadronic final state. In addition, the two photons can be in a CP-even of CP-odd final state allowing in principle to study CP violating phenomena without any involved hadron. The long-distance contributions to this decay are due to $B \to V\gamma$ decays with a light vector meson V, followed by a $V \to \gamma$ conversion. They are suppressed by Λ_{QCD}/m_b and are estimated to be below 5% [128].

The SM calculation [129] for the double radiative decays are in the range of

$$\begin{aligned} \mathcal{B}(B^0_s \to \gamma\gamma)_{SM} &= 0.5 - 4 \times 10^{-6} \\ \mathcal{B}(B^0_d \to \gamma\gamma)_{SM} &= 1.5 - 9 \times 10^{-8} \end{aligned}$$

and have large uncertainties due to non-perturbative inputs in the hadronic matrix elements. In principle it is possible to determine $|V_{td}/V_{ts}|^2$ if the ratio of the two decays is measured. The present experimental limits at a 90% C.L. are given by

$$\begin{aligned} \mathcal{B}(B^0_s \to \gamma\gamma)_{exp} &< 1.48 \times 10^{-4}\ [130] \\ \mathcal{B}(B^0_d \to \gamma\gamma)_{exp} &< 0.54 \times 10^{-6}\ [131] \end{aligned}$$

and were obtained by L3 (Belle) in case of the B^0_s (B^0_d) decay.

The decay can be enhanced in MSSM with contributions from SUSY particles that appear in the loops such as charged Higgs and up quarks, or charginos and up scalar squarks. In most cases the existing tight constraints from $b \to s\gamma$ also apply for $b \to s\gamma\gamma$. In R_p violating SUSY scenarios however, several diagrams can contribute to $B^0_s \to \gamma\gamma$ which are irrelevant in $b \to s\gamma$ decays [132] and can lead to enhancements of up to 16 with respect to the SM decay.

The decay $B^0_{d,s} \to \nu\bar{\nu}$ is a completely invisible decay and is forbidden in the SM due to helicity conservation of the massless neutrinos. The only existing bound is for the decay $B^0_d \to \nu\bar{\nu}$ with $\mathcal{B}(B^0_d \to \nu\bar{\nu}) < 2.2 \times 10^{-4}$ at a 90% C.L. The limit was obtained by Babar [133] and is only possible to achieve, if a well-defined initial state of $B^0_d\bar{B}^0_d$ exists, such that the other B in the event can be completely reconstructed.

If an extra real photon is emitted from the charged b or light quark line, the helicity suppression does not exist anymore and the decay occurs via loop diagrams at a finite rate. The governing Wilson coefficients for the $b \to s(d)\gamma\nu\bar{\nu}$ transition are the same as in $b \to$

$s(d)\nu\bar{\nu}$ decays such that new physics contributions would alter this decay in a similar way. The most recent SM calculation [134] for the branching ratio of $B^0_{d,s} \to \nu\bar{\nu}\gamma$ yields:

$$\begin{aligned} \mathcal{B}(B^0_s \to \nu\bar{\nu}\gamma)_{SM} &= 1.8 - 7.5 \times 10^{-6} \\ \mathcal{B}(B^0_d \to \nu\bar{\nu}\gamma)_{SM} &= 0.7 - 4.2 \times 10^{-8} \end{aligned}$$

The large uncertainties arise from unknown non-perturbative input, that is necessary to describe the constituent quark momentum distribution. The only existing experimental limit is again from Babar [133] with $\mathcal{B}(B^0_d \to \nu\bar{\nu}\gamma) < 4.7 \times 10^{-5}$ at a 90% C.L.

Another class of radiative leptonic decays are $B^0_{d,s} \to \ell^+\ell^-\gamma$ decays, which are called leptonic Dalitz decays. As in the previous case, the additional photon emission breaks the helicity suppression, such that $\mathcal{B}(B^0_{d,s} \to e^+e^-\gamma)$ is even larger than its pure leptonic counterpart $\mathcal{B}(B^0_{d,s} \to e^+e^-)$. The SM calculations [135] are obtained by attaching a photon line to any of the internal or external quark lines of $b \to s\ell^+\ell^-$, such that the short-distance structure is very similar. The results for the SM calculations of the $B^0_{d,s} \to \ell^+\ell^-\gamma$ decays are shown in Tab. 4.12. Compared to the result of $B_{d,s} \to \ell^+\ell^-$ from Tab. 4.10, the electron channel in the Dalitz decay is now significantly enlarged, while the muon mode has roughly the same branching ratio values.

Table 4.12: Standard Model branching fraction predictions for the decays $B^0_{d,s} \to \ell^+\ell^-\gamma$ according to [135].

	$\mathcal{B}(B^0_d \to \ell^+\ell^-\gamma)$	$\mathcal{B}(B^0_s \to \ell^+\ell^-\gamma)$
$\ell = e$	1.5×10^{-10}	7.1×10^{-9}
$\ell = \mu$	1.8×10^{-10}	8.3×10^{-9}
$\ell = \tau$	6.2×10^{-10}	1.6×10^{-8}

As in $b \to s\ell^+\ell^-$ transitions, the Dalitz decay suffers from long-distance effects due to charmonium resonances. The sensitivity of this decay to new physics was studied in Ref. [136] and is very similar to $b \to s\ell^+\ell^-$ decays. The branching ratio might be enhanced depending on certain values for $\tan\beta$ and the mass of the charged Higgs. In addition to the branching ratio, the forward-backward asymmetry and the photon energy would give valuable information to the underlying structure of the effective Hamiltonian, once this decay is precisely measured. So far, no experimental limit on a leptonic Dalitz decay for B mesons exist.

Finally, there is also the double Dalitz decay $B^0_{d,s} \to \ell^+\ell^-\ell'^+\ell'^-$, which proceeds through $B^0_{d,s} \to \gamma^*\gamma^*$ transitions. The SM branching ratios for B^0_s decays were calculated in Ref. [137] and are presented in Tab. 4.13.

The branching ratios for the double Dalitz B decays are very small and might even not be detectable at LHC. In case of B^0_s mesons irreducible background would come from $B^0_s \to \phi\phi$ decays with ϕ mesons decaying into lepton pairs. This background however, is suppressed relative to the double Dalitz by more than one order of magnitude.

Table 4.13: Standard Model branching fraction predictions for the double Dalitz decays $B_s^0 \to \ell^+\ell^-\ell'^+\ell'^-$.

	$\mathcal{B}(B_s^0 \to \ell^+\ell^-\ell'^+\ell'^-)$
$\ell, \ell' = e^\pm, e^\pm$	3.6×10^{-10}
$\ell, \ell' = e^\pm, \mu^\pm$	1.1×10^{-10}
$\ell, \ell' = \mu^\pm, \mu^\pm$	3.5×10^{-10}

4.6 $B_{d,s}^0 \to \ell^+\ell'^-$

The decays $B_{d,s}^0 \to \ell^+\ell'^-$ with $\ell^+\ell'^- = (e^\pm\mu^\mp, \mu^\pm\tau^\mp, e^\pm\tau^\mp)$ are all lepton flavor violating processes and hence forbidden in the SM. Although the SM conserves lepton number, the observation of neutrino oscillations and hence a non-zero neutrino mass implies that lepton number must be violated. The small neutrino mass values are best explained via the seesaw mechanism, which involves super-heavy singlet (right-handed) Majorana neutrinos. The heavy neutrino interactions give also rise to lepton-violating processes in Higgs penguin diagrams of supersymmetric seesaw models [138] or in Left-Right models with heavy neutrinos [139]. Within such models, lepton-violating radiative decays such as $\ell^\pm \to \ell'^\pm\gamma$ or $\ell^+ \to \ell'^+\ell'^+\ell'^-$ can be related to $B_{d,s}^0 \to \ell^\pm\ell'^\mp$ decays.

The experimental bounds on lepton flavor violating processes from lepton radiative decays $\ell^\pm \to \ell'^\pm\gamma$ and from $B_{d,s}^0 \to \ell^\pm\ell'^\mp$ decays are listed in Tab. 4.14:

Table 4.14: Experimental limits on lepton flavor violating decays.

Decay	Limit at 90% C.L.	Experiment
$\mu \to e\gamma$	1.2×10^{-11}	MEGA [140]
$\tau \to \mu\gamma$	3.1×10^{-7}	Belle [141]
$B_s^0 \to e^\pm\mu^\pm$	6.1×10^{-6}	CDF [142]
$B_d^0 \to e^\pm\mu^\pm$	1.7×10^{-7}	Belle [143]
$B_d \to e^\pm\tau^\pm$	1.1×10^{-4}	CLEO [144]
$B_d \to \mu^\pm\tau^\pm$	3.8×10^{-5}	CLEO [144]

At high $\tan\beta$, lepton violation processes and $B_s^0 \to \mu^+\mu^-$ decays are connected through the Higgs-penguin. The single Higgs-penguin $\ell - H - \ell'$ as presented in Fig. 3.22 may lead to lepton flavor violating decays into lepton pairs $\ell\ell'$. For instance, the τ decay into three leptons $\tau \to (e, \mu)\ell\ell$ belongs to this class. Its amplitude however, is mass-generation mechanism dependent. Consequently, quark and lepton flavor violating processes such as $B_{d,s}^0 \to \ell^+\ell'^-$ are then dominated by double Higgs-penguin contributions at large $\tan\beta$.

In the studies of Ref. [138], it was found that existing bounds on $\tau^\pm \to \mu^\pm\gamma$ together with $B_s^0 \to \mu^+\mu^-$ restrict the branching ratios of new processes such as $B_s^0 \to \mu^\pm\tau^\mp$ and

$\tau \to \mu\mu\mu$ to less than 4×10^{-9} and 4×10^{-10}, respectively. This means, that they become only interesting if they can be experimentally probed at the 10^{-9} level or lower. The Higgs-mediated lepton flavor-violation in the rare decays $B^0_{d,s} \to e^\pm \mu^\mp$ is highly constrained by the experimental $\mu^\pm \to e^\pm \gamma$ limit and may push $\mathcal{B}(B^0_{d,s} \to e^\pm \mu^\mp)$ to be less than 10^{-15}, such that a dedicated search for $B^0_{d,s} \to e^\pm \mu^\mp$ at present and future colliders is of little theoretical interest.

5 Experimental Search Strategies at Hadron Colliders

This chapter describes the details of two experimental searches for FCNC B decays that were carried out at Tevatron. The projected reach towards the end of the Tevatron physics program in the year 2009 is presented and the expectations for the upcoming LHC illustrated. Based on the theoretical discussions in the previous chapter an experimental strategy for a systematic FCNC program starting at Tevatron and developing into the LHC era is sketched.

5.1 General Considerations

5.1.1 Search and Analysis Techniques

The rare B decays that were presented in the last chapter have typically small branching fractions with large backgrounds in a hadron collider environment. The task of a search analysis consists then mainly of discriminating between signal and background events as much as possible in order to identify the rare decay. Other analysis issues that are closely related to this task are selecting discriminating variables that are best adopted to the problem, identifying regions of interest in data to search for the signal and/or reducing the dimensionality of the data without losing much discrimination power to simpler optimize the analysis.

Data that are taken at particle physics experiments are intrinsically multi-variate. This means, that one recorded event in a detector, if it is signal or background, involves several measured quantities or features. To obtain the best possible results, it is therefore necessary to make maximal use of information in the data and hence to employ multi-variate analysis methods [145]. In contrast to an analysis that is based on successive cuts on several feature variables, a multi-dimensional approach is better suited to find the optimal discrimination between signal and background processes. Such a multi-variate analysis evaluates the multi-dimensional feature space to identify the best discrimination variables or can find linear independent components in data to reduce the dimensionality of the problem.

A multi-variate discrimination method tries to minimize the probability of misclassification, i.e., that a background event is falsely classified as signal event or vice versa. Mathematically, most multi-variate methods try to approach the Bayes discriminant r that is defined for two signal and background classes given a set of event variables $\mathbf{x}$ as follows:

$$r(\mathbf{x}) = \frac{p(s|\mathbf{x})}{p(b|\mathbf{x})} = \frac{p(\mathbf{x}|s)p(s)}{p(\mathbf{x}|b)p(b)} \tag{5.45}$$

Here, $p(\mathbf{x}|s)$ and $p(\mathbf{x}|b)$ are the conditional class probabilities, i.e., probability density functions for signal and background, respectively, and $p(s)$ and $p(b)$ are the prior distributions. It has been shown that the Bayes discriminant r is optimal in a sense of minimizing the error rate. The problem of signal and background discrimination in multi-variate analysis reduces then to the problem of approximating the function r and many different multi-variate techniques are finally trying to estimate r or functions of r. Multi-variate methods that are often used in data analysis include Fisher linear discrimination, artificial neural networks and probability density estimations based on kernel methods.

There is probably no single multi-variate method that is superior to the others. It is recommended that several methods should be applied and tested and their performances evaluated. For an overview of several multi-variate methods see Ref. [145].

5.1.2 Blind Analysis

A blind analysis is a measurement that is performed without looking at the answer during the process of analyzing data. It is the optimal way in search analysis to reduce or even eliminate the experimenter's bias, i.e., the unintended influencing of a result in a certain direction. Blind analysis techniques are common in bio-medical research for many decades and have now been established in particle physics for rare signal searches as well. In case of the rare B decays, the mass of the decaying B is well known. One of the easiest implementations of a blind analysis consists then of a hidden signal region around the known B mass, which is not examined before all the analysis is completed. Any events in the signal region are kept hidden, before the analysis method, selection cuts and background estimations are fixed. After the cuts are finalized, the box can then be opened and examined.

5.1.3 Normalization of the Rare Decay

In order to calculate a branching ratio or an upper limit the decay has to be normalized to a known cross section or to a known decay. At a hadron collider, the normalization to a cross section is more complicated, since several trigger and selection efficiencies have to be determined. An simpler method is to chose a known B decay which has a very similar decay topology than the signal channel and to apply the same selection cuts to signal and normalization channel. The advantage is that most of the selection efficiencies tend to cancel in the ratio and only a reduced number of systematic uncertainties will enter into the final result. A branching ratio or its upper limit can then be simply evaluated by normalizing all measured events or the obtained upper event limit relative to the known decay.

5.1.4 Discriminating Variables

In order to suppress the overwhelming background and to select the signal events of interest discriminating cuts have to be applied and optimized. Such variables are typically based on distinct features of the B mesons and exploit their long lifetime, the relative hard b-quark fragmentation into a b-flavored hadron and constrain the decay products to a common (secondary) vertex. Figure 5.33 represents a pictogram to visualize the topology of the simple leptonic B decay into two muons. Several variables that are useful for the selection of B events are now discussed.

Once a primary and secondary vertex in the event is found, the decay length vector $\vec{l}_{vtx}$ is defined as a 3-dimensional vector pointing from the primary vertex to the secondary vertex. A so-called **pointing angle** α can then be constructed as the angle between the momentum vector of the B candidate and the decay length vector $\vec{l}_{vtx}$. This angle is well-defined and used as an important consistency check between the direction of the decay axis and the flight direction of the B candidate. If the tracks that are used to build the B candidate originate from the decay of a parent particle B_s^0, the vector $\vec{l}_{vtx}$ should point into the same direction as the momentum vector $\vec{p}(B)$ of the B candidate.

As previously stated, the long lifetime of B mesons allows the use of the decay length as a strong rejection criteria against non-b induced background and combinatoric background, e.g. two fake muons that happen to form a good vertex. The displacement of the B decay vertex from the primary interaction vertex can be defined as a 2-dimensional quantity, i.e., as a transverse decay length L_{xy}, or as a full 3-dimensional quantity. In case of two dimensions

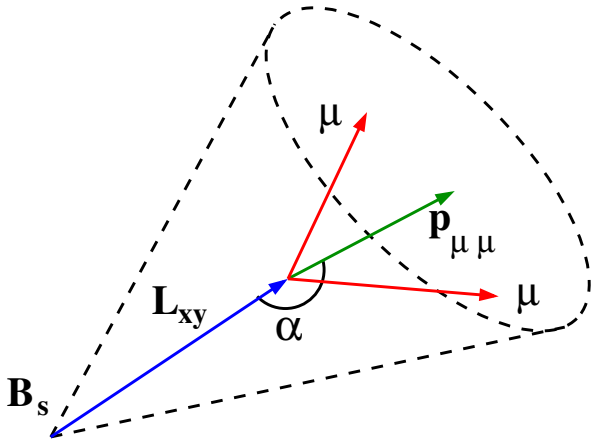

Figure 5.33: Pictogram for visualization of the discriminating variables for the decay $B_s^0 \to \mu^+\mu^-$.

the transverse decay length L_{xy} is then the projection of the 2-dimensional decay length vector $\vec{l}_{xy}$ on the transverse momentum of the B candidate:

$$L_{xy} = \frac{\vec{l}_{xy} \cdot \vec{p}_T^B}{p_T^B}. \tag{5.46}$$

The generalization to the full three dimensional decay length L_{3D} is straightforward. The decay length is related to the proper decay time in the B rest frame by $L = \beta\gamma c\tau$ with the boost factor $\beta\gamma = |\vec{p}(B)|/m_B$. Hence, as an alternative to the decay length, the proper decay time $c\tau$ can be used given by

$$c\tau = L_{3D} \cdot \frac{m_B}{|\vec{p}(B)|}. \tag{5.47}$$

The fragmentation characteristics of the b-quark are such that most of its momentum is carried by the B hadron. A large fraction of the momentum of the tracks observed close to the B meson is therefore expected to be carried by the daughter tracks of the B. Thus, the number of extra tracks close to the B candidate tends to be small. This feature can be exploited by an isolation variable, $\mathcal{I}$, which can be defined as:

$$\mathcal{I} = \frac{|\vec{p}(B)|}{|\vec{p}(B)| + \sum\limits_{\text{track}\, i \neq B} p_i(\Delta\mathcal{R})}. \tag{5.48}$$

Here, $\sum\limits_{\text{track}\, i \neq B} p_i$ is the scalar sum of the momenta of all tracks excluding the tracks used to build the B candidate that fall within a cone of certain size $\Delta\mathcal{R} = \sqrt{|\phi|^2 + |\eta|^2}$ in ϕ and η space around the momentum vector $\vec{p}(B)$ of the B candidate.

5.2 $B_s^0 \to \mu^+\mu^-$

As it was discussed in the previous chapter the purely leptonic decay $B_s^0 \to \mu^+\mu^-$ is the gold-plated mode for probing new physics in rare B decays. In the SM, the B_s^0 decay into two

leptons is enhanced with respect to its B_d^0 counterpart by $|V_{ts}/V_{td}|^2$ giving hadron colliders a better perspective for its search, than at e^+e^- machines. The decay channel into two muons provides a clear experimental signature of only two muons in the final state, whose momenta combine then to the B_s^0 mass. The mass resolution in the tracking detectors plays a crucial role to suppress background.

5.2.1 The Experimental Search at Tevatron

The first search for $B_s^0 \to \mu^+\mu^-$ decays at hadron colliders was already reported in 1988 by UA1 [146]. The detector could not resolve B_s^0 from B_d^0 decays such that a combined limit for an unseparated mixture of $B_{d,s}^0$ of $\mathcal{B}(B_{d,s}^0 \to \mu^+\mu^-) < 9 \times 10^{-5}$ at a 90% C.L. was obtained.

The search for $B_s^0 \to \mu^+\mu^-$ was then continued at the Tevatron collider during Run I and is presently one of the core analysis channels for Run II. The previously reported limits from CDF and DØ are listed in Tab. 5.15:

Table 5.15: Overview of Tevatron limits for the decay $B_s^0 \to \mu^+\mu^-$.

Experiment	Luminosity [pb^{-1}]	90% C.L. limit	Reference
CDF Run I	98	2×10^{-6}	PRD **57**, 3811 (1998)
CDF Run II	171	5.8×10^{-7}	PRL **93**, 032001 (2004)
DØ Run II	240	4.1×10^{-7}	PRL **94**, 071802 (2005)
DØ Run II (prel.)	300	3.0×10^{-7}	DØ Note 4733-Conf
CDF Run II	364	1.5×10^{-7}	hep-ex/0508036

Both Tevatron experiments use very similar methodologies to search for $B_s^0 \to \mu^+\mu^-$ decays: Oppositely charged muon pairs are selected in a mass window around the B_s^0 mass. The analysis are performed with a hidden signal box to avoid any bias in the results using sideband data for background determination. The widths of the signal box and of the sidebands are determined by the expected mass resolution for the signal channel and is drastically different between the CDF and DØ detectors. The mass resolution of CDF is estimated to be 24 MeV/c^2 while DØ evaluates its resolution to be 90 MeV/c^2. The superior mass resolution allows CDF an unique separation of B_s^0 from B_d^0 decays and to perform an independent search on $B_d^0 \to \mu^+\mu^-$ decays as well.

The data samples used by the Tevatron experiments consist of di-muon triggered events within a restricted pseudorapidity region to be well inside the fiducial acceptance of the detectors. CDF is dividing the data set into a "central" region for muon pairs within $|\eta| < 0.6$ and a "central-extended" region containing di-muon where one muon is reconstructed in the central and the other in the extended muon system ($0.6 < |\eta| < 1.0$). DØ is utilizing its excellent muon coverage selecting muon pairs within $|\eta| < 2.0$. A cut on the transverse momentum of the di-muon pairs is required to be 4 GeV/c for CDF and 5 GeV/c for the DØ analysis to suppress random combinatoric background which dominates at low momentum.

After a set of pre-selection cuts on track and vertex quality, further discriminating variables for the final event selection are then exploited. CDF is using lifetime information $c\tau$,

3-dimensional pointing angle and a track isolation criteria for the B candidate. The latter two discriminants are also employed in the DØ analysis. Instead of the proper life time, DØ is using the transverse decay length significance $L_{xy}/\sigma_{L_{xy}}$, which has been found to give better discrimination power than the decay length information L_{xy} alone, as large values of L_{xy} may originate due to large uncertainties.

To increase the sensitivity for the rare decay, both experiments perform an optimization over the discriminating variables, while leaving the signal box hidden. CDF constructs from the three discriminating variables i a likelihood ratio given by

$$L_R = \frac{\Pi_i P_s(x_i)}{\Pi_i P_s(x_i) + \Pi_b(x_i)} \tag{5.49}$$

where $P_{s,b}(x_i)$ is the probability that a signal (background) event has an observed value x_i for variable i. The probability distributions for signal events are obtained from signal MC and the background distributions are taken from side band data. The analysis optimizes the Likelihood ratio cut for the best expected limit. This optimization is performed separately for the two search channels of CDF, i.e., for di-muons in the central/central and central/extended regions.

DØ maximizes the sensitivity $P = \epsilon/(1+\sqrt{N_{back}})$ where ϵ is the signal efficiency obtained from a signal MC and N_{back} is the number of expected background events as estimated from the sidebands. The figure of merit P is a measure of the sensitivity for small signal searches [147] and allows an unbiased limit determination that is independent of any limit-setting algorithms. The optimization itself is performed in a random-grid, which scans through all cut value combinations according to the signal event probability distribution that is obtained from MC.

Relative to the pre-selected samples the signal efficiencies for the selection cuts of the three discriminating variables are quite similar for DØ and CDF. For their optimal Likelihood cut, CDF obtains a selection efficiency of 35% while DØ quotes 38% after optimization.

After all cuts, the remaining events in the signal boxes for CDF and DØ are shown in Fig. 5.34. The observed number of events, the expected background events and other analysis information are listed Tab. 5.16.

The limit on the branching ratio is computed using the measured decay $B^+ \to J/\psi K^+$ with $J/\psi \to \mu^+\mu^-$ as normalization mode. The idea is that exactly the same selection cuts on the di-muons in signal and normalization channel are applied, such that systematic errors tend to cancel. Normalizing the signal to $B^+ \to J/\psi K^+$ rather than to the $B_s^0 \to J/\psi\phi$ decays has the advantage that the former mode has a higher statistics and the branching ratio and life time are well known from measurements at e^+e^- experiments. In addition, understanding the efficiency to detect $B_s^0 \to J/\psi\phi$ events is complicated by the presence of CP even and odd decay components with significant different lifetimes.

The master equation to calculate an upper limit on the decay $B_s^0 \to \mu^+\mu^-$ is given by:

$$\mathcal{B}(B_s^0 \to \mu^+\mu^-) \leq \frac{N_{\rm ul}}{N_{B^\pm}} \cdot \frac{\epsilon_{\mu\mu K}^{B^\pm}}{\epsilon_{\mu\mu}^{B_s^0}} \cdot \frac{\mathcal{B}(B^\pm \to J/\psi(\mu^+\mu^-)K^\pm)}{f_s/f_u + R \cdot \frac{\epsilon_{\mu\mu}^{B_d^0}}{\epsilon_{\mu\mu}^{B_s^0}}}, \tag{5.50}$$

where

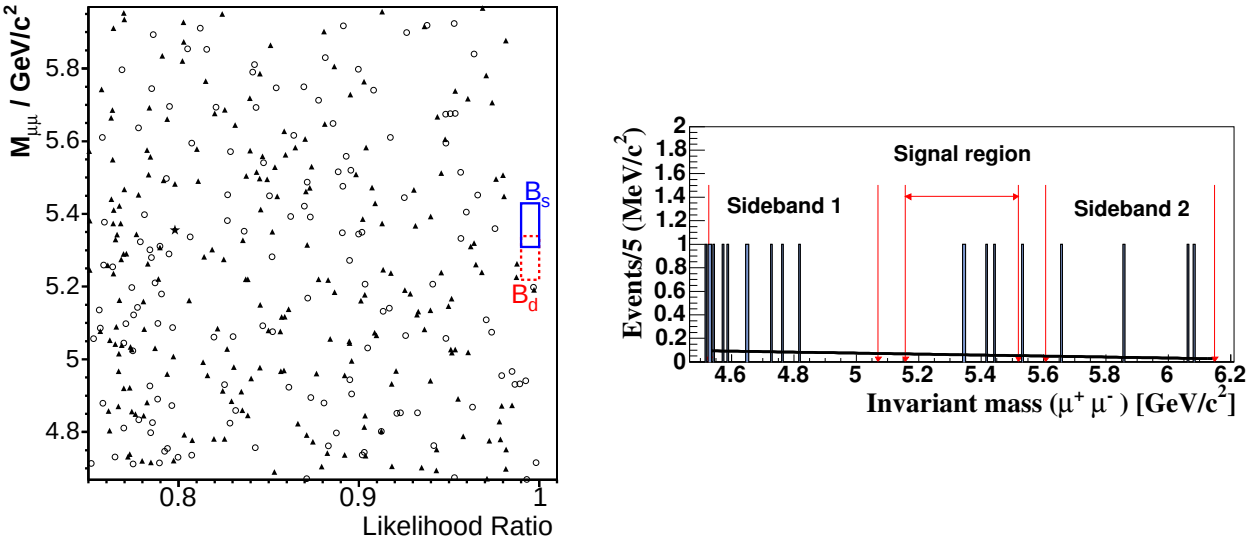

Figure 5.34: The mass distribution after opening the signal box for CDF (left) and DØ (right). CDF observed zero events in the $B^0_{d,s}$ search channels while four events were found in the DØ signal region.

- $N_{\rm ul}(N_{obs}, N_{back})$ is the upper limit on the number of observed events at a chosen C.L. for N_{obs} observed events in the signal region with N_{back} expected background events. Hence, the limit on $\mathcal{B}(B^0_s \to \mu^+\mu^-)$ is obtained from a single-channel counting experiment.

- $\epsilon^{B^0_s}_{\mu\mu}$ and $\epsilon^{B^\pm}_{\mu\mu K^\pm}$ are the efficiencies of the signal and normalization channels, obtained from MC simulations and $N_{B^\pm}$ is the number of recorded normalization events.

- f_u and f_s are the fragmentation fractions of a b or $\bar{b}$ quark to a $B^\pm/B^0_d$ or a B^0_s meson, respectively. The ratio which enters into the limit calculation at Tevatron has been calculated using the latest world average values [8] for the fragmentation for $B^0_{u,d}$ and B^0_s mesons, respectively. For the uncertainty on the fragmentation ratio the correlations between the two as given by Ref. [9] has been assumed ($f_u/f_s = 3.71 \pm 0.41$).

- $\mathcal{B}(B^\pm \to J/\psi\, K^\pm) = (1.00 \pm 0.04) \times 10^{-3}$ and $\mathcal{B}(J/\psi \to \mu^+\mu^-) = (5.88 \pm 0.1)\%$ [8]; and

- $R \cdot \epsilon^{B^0_d}_{\mu\mu}/\epsilon^{B^0_s}_{\mu\mu}$ is the branching fraction ratio $\mathcal{B}(B^0_d \to \mu^+\mu^-)/\mathcal{B}(B^0_s \to \mu^+\mu^-)$ of $B^0_{d,s}$ mesons decaying into two muons multiplied with their detection efficiency ratio for the defined mass window centered around the B^0_s mass. This efficiency ratio has to enter in the $B^0_s \to \mu^+\mu^-$ limit calculation of Eq. 5.50 due to a feed-down of $B^0_d \to \mu^+\mu^-$ decays into the B^0_s signal window. In the SM, R is given by $R = \tau(B^0_d)/\tau(B^0_s) \cdot m_{B^0_d}/m_{B^0_s} \cdot f^2_{B^0_d}/f^2_{B^0_s} \cdot |V_{td}|^2/|V_{ts}|^2$, where $\tau_{B^0_{d,s}}$ are the lifetimes of the B-mesons and $f_{B^0_{d,s}}$ the meson decay constants. The ratio $\epsilon^{B^0_d}_{\mu\mu}/\epsilon^{B^0_s}_{\mu\mu}$ has been determined for the DØ analysis from simulation to be 0.92 ± 0.04. In case of CDF, the efficiency ratio is close to zero, due to the superior mass separation.

To simplify the calculation of the upper limit on the branching fraction $\mathcal{B}(B_s^0 \to \mu^+\mu^-)$, it was assumed for DØ that there are no contributions from $B_d^0 \to \mu^+\mu^-$ decays ($R \approx 0$) in the search window centered around the B_s^0 mass. This assumption is acceptable since the decay is suppressed by $|V_{td}/V_{ts}|^2 \approx 0.04$ in the SM. Any non-negligible contribution due to B_d^0 decays ($R > 0$) would make the obtained branching fraction $\mathcal{B}(B_s^0 \to \mu^+\mu^-)$ as given in Eq. 5.50 smaller. It is thus a conservative approach.

Table 5.16: Summary of experimental inputs from the CDF and DØ analysis that were used to calculate the $B_s^0 \to \mu^+\mu^-$ limits.

	CDF: central	CDF: central/extended	DØ
Luminosity	364 pb^{-1}	336 pb^{-1}	300 pb^{-1}
$\frac{\epsilon_{\mu\mu K}^{B^\pm}}{\epsilon_{\mu\mu}^{B_s^0}}$	0.852 ± 0.084	0.485 ± 0.048	0.247 ± 0.019
$N_{B^\pm}$	1785 ± 60	696 ± 39	906 ± 41
N_{back}	0.81 ± 0.12	0.66 ± 0.13	4.3 ± 1.2
N_{obs}	0	0	4
ses ($\times 10^7$)	1.04 ± 0.16	1.52 ± 0.25	0.59 ± 0.09
ses ($\times 10^7$)	0.617 (CDF combined)		
expect. limit 90% C.L.	3.5×10^{-7}	5.6×10^{-7}	3.5×10^{-7}
expect. limit 90% C.L.	2.0×10^{-7} (CDF combined)		
final limit 90% C.L.	1.5×10^{-7} (CDF combined)		3.2×10^{-7}

In Tab. 5.16 the single-event-sensitivity (*ses*) and the expected upper limit at a 90% C.L. are listed as well. The *ses* is defined as the obtained numerical branching ratio in case of $N_{\rm ul} = N_{obs} = 1$. It can be interpreted as a measure of the inverse of the total signal efficiency (including acceptance) of the analysis multiplied with the collected statistics, i.e., luminosity. The numbers in Tab. 5.16 show, that DØ has a slightly better single event sensitivity than CDF, even with about 20% less luminosity that was used in the DØ analysis. This is mainly due to the wider range in muon pseudorapidity that DØ is covering. The expected upper limit as quoted in Tab. 5.16 is defined as the average upper limit that is obtained if the experiment is hypothetically repeated by summing over all possible experimental outcomes weighted with their Poisson probability factor of occurrence. The expected upper limit is a measure of the exclusion power in a search for an unobserved decay. In its calculation the expected background plays a dominant role. The lower background expectation of CDF is then the reason why the expected upper limit for the two combined CDF channels is much better than for DØ. The expected number of background events in the two CDF search regions are 0.81 ± 0.12 and 0.66 ± 0.13, respectively, while DØ expects 4.3 ± 1.2 events. The major part of CDF's lower background expectation is explained by the almost four times better mass resolution since a small and narrow signal region yields a smaller number of expected background events, even if the overall background rejection in the full mass region of interest is the same.

The final limits with the actual number of observed events are shown in the last row of Tab. 5.16. Since zero events were found in the CDF search, the final limit is significantly smaller than the expected limit.

5.2.2 Tevatron Combination and Outlook

Both results on the upper limits have been combined [103] taking properly into account the correlated and uncorrelated uncertainties. The uncertainties on fragmentation ratio and branching ratios for the normalization channel were added in quadrature and treated as fully correlated in the limit calculation. All other uncertainties were assumed to be uncorrelated. The combined upper limit was obtained with a Bayesian technique [148] that parameterizes the uncertainties as gaussian distributions in the integration. A flat prior was chosen for the a priori unknown signal cross section and various robustness tests by changing the cut-offs of the prior distribution were performed. The final combined limit for $B_s^0 \to \mu^+\mu^-$ is then

$$\mathcal{B}(B_s^0 \to \mu^+\mu^-)_{comb.} < 1.2\,(1.5) \times 10^{-7} \text{ at a } 90\%\,(95\%) \text{ C.L.} \tag{5.51}$$

assuming for the fragmentation ratio the standard PDG value [8] of $f_u/f_s = 3.71 \pm 0.41$. Using an evaluation of the fragmentation function based on Tevatron data alone ($f_u/f_s = 3.32 \pm 0.59$) the limit would then improve by 10%.

The excellent mass resolution allows CDF to carry out an independent search analysis for the leptonic decays of B_s^0 and B_d^0, which is not possible for the DØ experiment. The analysis of DØ however, shows also sensitivity to $B_d^0 \to \mu^+\mu^-$ decays. Setting $\mathcal{B}(B_s^0 \to \mu^+\mu^-) = 0$ allows to combine the Tevatron results to obtain an upper limit on $B_d^0 \to \mu^+\mu^-$ decays:

$$\mathcal{B}(B_d^0 \to \mu^+\mu^-)_{comb.} < 3.2\,(4.0) \times 10^{-8} \text{ at a } 90\%\,(95\%) \text{ C.L.} \tag{5.52}$$

It should be stressed, that the Tevatron combined bound on $B_d^0 \to \mu^+\mu^-$ is not independent of the B_s^0 limit, since the information from one single DØ search result was used twice.

The projected Tevatron reach for the DØ and CDF combined search on $B_s^0 \to \mu^+\mu^-$ is shown in Fig. 5.35 as function of the Run II luminosity. The projection was obtained by assuming an optimization of the analysis with about 1 fb^{-1} of data. In case of an absence of any signal, the expected limit reaches 2×10^{-8} at a 90% C.L. for an accumulated luminosity of 8 fb^{-1} per experiment. Such an upper limit is less than a factor of ten away from the SM value. The stringent limit could eliminate a large part of the high $\tan\beta$ parameter region in supersymmetric models.

5.2.3 The $B_s^0 \to \mu^+\mu^-$ reach at LHC

The search for the rare decay $B_s^0 \to \mu^+\mu^-$ has also moved into the central focus of the LHC experiments. An overview of the expected number of $B_s^0 \to \mu^+\mu^-$ events and expected background after the first LHC year is given in Tab. 5.17. The first LHC year corresponds to a luminosity of 2×10^{32} cm^{-2}s^{-1} for LHCb and 1×10^{33} cm^{-2}s^{-1} for Atlas/CMS. In general, it is difficult to estimate reliably the background from MC, since an enormous amount of inclusive $b\bar{b}$ events has to be generated and processed with detector simulation and reconstruction programs. Most of the background expectations are therefore rather rough estimations.

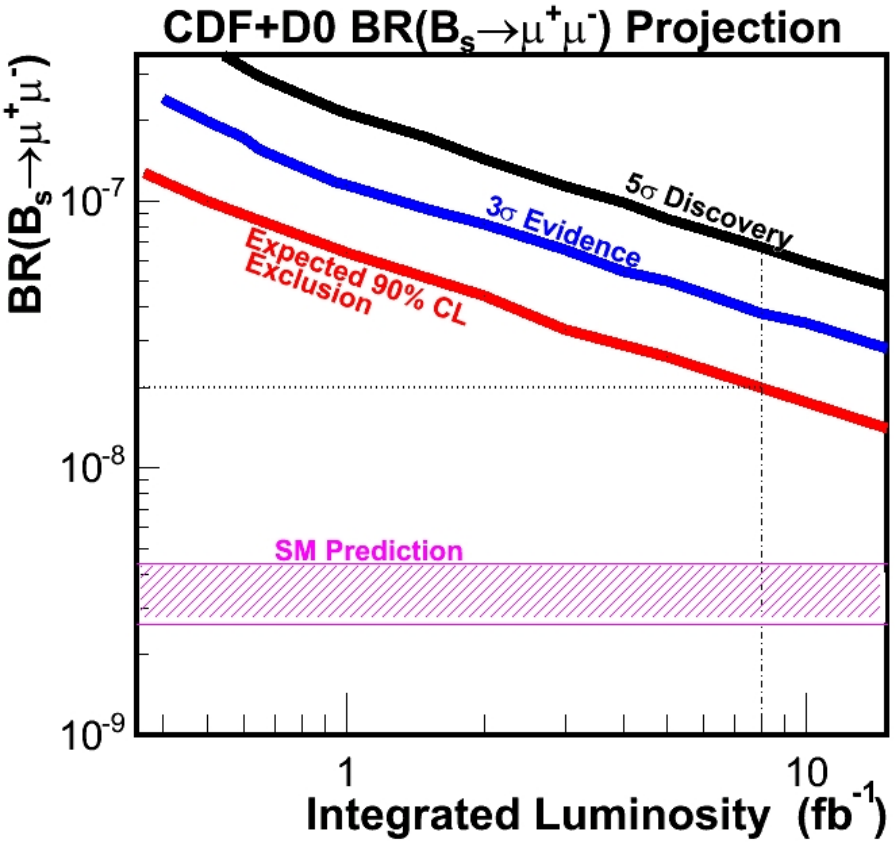

Figure 5.35: The projected Tevatron reach for $B_s^0 \to \mu^+\mu^-$ as function of the integrated luminosity for DØ and CDF.

Table 5.17: Overview of expected signal yield for $B_s^0 \to \mu^+\mu^-$ events after one year of LHC data taking assuming the SM branching ratio. The numbers were taken from Ref. [149].

$B_s^0 \to \mu^+\mu^-$	CMS	Atlas	LHCb
luminosity	10 fb^{-1}	10 fb^{-1}	2 fb^{-1}
signal events	7	16	17
background events	< 1	< 31	< 100
mass resolution (MeV/c^2)	46	80	18

Assuming the SM value for the branching ratio of 3.5×10^{-9} for $B_s^0 \to \mu^+\mu^-$ decays, LHCb selects [150] in one year of data taking 17 signal events. Very similar to the Tevatron analysis, the event selection at LHCb requires the di-muon candidate to be well-separated from the primary interaction vertex, but identifies di-muons with a rather low transverse momentum of 3.5 GeV/c. The overall selection efficiency has been evaluated to be 3.1% and

trigger efficiencies are estimated to be 79%. The present limit on the background level for LHCb was estimated from about 11M fully simulated and reconstructed inclusive $b\bar{b}$ events and 10M $b\bar{b}$ events, where both b-quarks were decaying semileptonically ($b \to \mu X$, $\bar{b} \to \mu X$). This so-called double semileptonic background is presently considered to be the most serious background for this decay, but other processes such as two hadron decays of B mesons with mis-identified muons and $B_c^{\pm} \to J/\psi(\to \mu^+\mu^-)\mu^{\pm}\nu$ decays could be dangerous as well. With the presently available MC statistics of background simulation, an upper limit at a 90% C.L. on the background to signal ratio of $B/S < 5.7$ was determined for LHCb.

The Atlas and CMS search will certainly benefit from the larger available luminosity and their di-muon triggers will not be problematic at the initial luminosity values. The signal yields in the first year however, will not exceed the LHCb expectations since trigger thresholds and offline selection cuts on the di-muon momentum for instance have to be set to higher values than at LHCb. In contrast to LHCb, the background studies for Atlas and CMS were performed on smaller MC samples, such that background expectations are rather crude. Compared to CMS, Atlas will additionally suffer from a significantly worse mass resolution making background rejection more difficult.

It is expected that a significant signal of $B_s^0 \to \mu^+\mu^-$ decays after the first year of LHC running can be reached, if the SM value for the branching ratio is assumed. The great interest for this decay will certainly lead to additional MC investigation at Atlas, CMS and LHCb, such that revised signal yield numbers and better background estimations will be presented in the near future.

5.3 Other Leptonic Decays

5.3.1 $B_s^0 \to \tau^+\tau^-$

The leptonic decay rate of neutral B mesons into τ's is by m_τ^2/m_μ^2 larger than its muonic counterpart. Were it not an experimental challenge to detect relative low-momentum τ's efficiently and separate them from large background, this decay would be certainly the prime candidate for a new physics search[4].

The characteristic feature of τ leptons is that they mostly (66%) decay into hadronic modes, of which just 77% have just one charged hadron (one-prong decay, mostly $\rho^{\pm}$ and $\pi^{\pm}$) and are accompanied by one neutrino in the final state. If the τ's are at large enough energies, such as from $Z \to \tau^+\tau^-$ or W decays, the hadronic decay products from τ decays are boosted into the original direction of the τ. An identification of hadronic τ decays is then possible by looking for a narrow, pencil-like jets with rather low track-multiplicity. At hadron colliders such measurements have been performed for τ's coming from $Z \to \tau^+\tau^-$ and $W^{\pm} \to \tau^{\pm}\nu$ decays. Moreover, the search for $H \to \tau^+\tau^-$ decay is also of prime interest in searches for the Higgs boson.

The distinct feature of τ decays at high momentum is not necessarily true anymore, if the τ leptons are produced from B decays, where τ's have in general much less transverse momentum. In fact, a reconstruction of B mesons decaying semileptonically into τ leptons has been achieved so far only at e^+e^- machines.

[4]To give an example of the difficult τ-detection, the Babar reach for $\mu^+\mu^-$ and $\tau^+\tau^-$ final states can be compared. Even at a e^+e^- annihilation machines with a well-defined initial state and a small background environment, the obtained upper limit on $B_d^0 \to \mu^+\mu^-$ is about 10^5 smaller than for $B_d^0 \to \tau^+\tau^-$.

The inclusive τ production cross section $\sigma(pp \to \tau X)$ at LHC is large and corresponds to about 120 μb. The dominant fraction (77%) of this huge τ production source is from $D_s^{\pm} \to \tau^{\mp} X$ decays, while τ production at larger p_t, i.e., from Z or W decays contribute with only 22 nb very little to the total inclusive production cross section.

A search for $B_s^0 \to \tau^+\tau^-$ at hadron colliders is therefore extremely complicated due to the presence of low momentum τ decay products from various meson decays that represent an overwhelming background. The isolation of $B_s^0 \to \tau^+\tau^-$ poses an almost unsolvable task. The decay contains at least two and as many as four neutrinos, so there is no clean kinematic discriminant that separates signal from background due to the undetected particles. Certainly, the most dangerous single background source for $B_s^0 \to \tau^+\tau^-$ signal events comes from the $B_s^0 \to D_s^{\pm}\tau^{\mp}\nu$ decays with a branching fraction of about 3×10^{-3} and the subsequent decay of $D_s^{\pm} \to \tau^{\pm}\nu$ with a branching fraction of 6.4%. The total branching fraction of $\mathcal{B}(B_s^0 \to D_s^{\pm}\tau^{\mp}\nu) \times \mathcal{B}(D_s^{\pm} \to \tau^{\mp}\nu)$ is then about 2×10^{-4}, i.e., a factor of two-hundred above the signal. If the two τ's are identified through the leptonic decays $\tau \to (e, \mu)\nu$, then there are not many handles over this background, as its topology is similar to the signal. A slight chance to cope with this background might be to identify the τ's through their three-prong decay channel $\tau \to 3\pi\nu$. The dominant background source is again from $B_s^0 \to D_s^{\pm}\tau^{\mp}\nu$ and the subsequent $\tau \to 3\pi\nu$ and $D_s \to 3$ prong (about 20%, mainly $KK\pi$) decays. This background might be suppressed by K identification, requiring π/K separation. In addition there could be an option to exploit the $B_s^0 \to \tau^+\tau^-$ kinematics in a constrained fit with three available vertices in the event.

No MC study has been made to look into the possibility of detecting $B_s^0 \to \tau^+\tau^-$ events neither at Tevatron nor LHC. It is obvious that such a search will be very difficult and complex and it might turn out to be completely impossible. But it might be worth to start an effort at LHC. As a first step towards this challenge it could make sense to begin with a search for the lepton-flavor violating decay $B_s^0 \to \mu^{\pm}\tau^{\mp}$ in order to better understand the large background levels.

5.3.2 Dalitz Decays $B_s^0 \to \mu^+\mu^-\gamma$

The helicity suppression does not apply in the Dalitz decay if an additional photon line exists. Therefore, the sensitivity of this decay to new physics is also reduced. Nevertheless, the Dalitz decay represents an interesting rare B decay mode and its measurement may complement the picture obtained from $B_s^0 \to \mu^+\mu^-$ decays. The Dalitz decay should be detectable at LHC within the first few years.

In order to experimentally determine a branching ratio or limit, the Dalitz decay $B_s^0 \to \mu^+\mu^-\gamma$ could be normalized to $B^+ \to \chi_{c1}^0(1P)K^+$ events with subsequent decay of $\chi_{c1}^0(1P) \to J/\psi\,\gamma$ and $J/\psi \to \mu^+\mu^-$. Apart from the additional kaon track, the event topology between signal and normalization mode is very similar, such that a relative measurement wold benefit from the cancelation of systematic effects.

The branching ratio of $B^+ \to \chi_{c1}^0(1P)K^+$ amounts to 6.5×10^{-4}, while for the radiative decay $\chi_{c1}^0(1P) \to J/\psi\,\gamma$ the fraction is 36.1%. Given the large number of B^+ mesons available at hadron colliders, large statistics for the normalization channel is feasible. As an example, CDF has already reconstructed [151] in 110 pb^{-1} of Run I about 20 ± 7 $B^+ \to \chi_{c1}^0(1P)K^+$ events.

An event selection strategy could then start with combining two muons to a common

vertex and adding a calorimeter cluster consistent with an electromagnetic shower deposition above a certain transverse energy to efficiently remove low energy γ's and π^0's. The location of the cluster and the reconstructed di-muon vertex determines then the momentum vector of the photon. Further background suppression has to be applied by requesting minimum transverse momentum, decay length, pointing angle and isolation of the $\mu^+\mu^-\gamma$ candidate. Since only the short distance physics if of interest, the resonant region in the di-muon mass around the J/ψ and ψ' has to be cut away. In addition, the signal mode has to be separated from the radiative penguin $B_s^0 \to \phi(\to \mu^+\mu^-)\gamma$ decays by excluding also the ϕ resonance.

There are no MC studies available that investigate signal and background yield, neither at Tevatron nor at LHC. The experimentally "visible" branching ratio will strongly dependent on the chosen energy cut on the photon and on the sizes of the cut-out regions in the di-muon mass. Theoretical calculations to evaluate the expected branching ratio after experimental cuts are therefore necessary to guide the experiments. It might be worth to start a search for this decay at Tevatron, and to begin to experimentally constrain $\mathcal{B}(B_s^0 \to \mu^+\mu^-\gamma)$. The decay is definitively a good search candidate for the LHCb experiment which is capable of measuring di-muons down to low transverse momenta. After a few years of data taking, an observation at LHC should be possible.

5.4 Exclusive B Decays with Electroweak Penguins

5.4.1 The DØ search for $B_s^0 \to \phi\,\mu^+\mu^-$

The decay $B_s^0 \to \phi\,\mu^+\mu^-$ is an exclusive FCNC decay related to the transition of $b \to s\,\mu^+\mu^-$ at quark level. Within the SM the decay rate $B_s^0 \to \phi\,\mu^+\mu^-$ decay is predicted to be of the order of 1.6×10^{-6} [85] excluding long-distance effects from charmonium resonances with about 30% uncertainties due to poorly known form factors.

DØ has conducted a blind analysis search [88] for $B_s^0 \to \phi\mu^+\mu^-$ decays using about 300 pb^{-1} of Run II data that were collected with the di-muon trigger. Since the interest lays only in the non-resonant decay, which is mediated through a FCNC diagram, the invariant mass of the two muons is requested to be outside the charmonium resonances. The events in the search are normalized to the resonant decay $B_s^0 \to J/\psi(\mu^+\mu^-)\,\phi$ events. The event final state contains two muons and two kaon candidate tracks that form a ϕ candidate and is the same for signal channel and (resonant) normalization channel.

A pre-selection of events is applied to collect a sample of B_s^0 candidates consisting of two muons and two oppositely charged tracks (from $\phi \to K^+K^-$) within the fiducial volume of the detector forming a good vertex. In the di-muon mass region of $0.5 < m_{\mu^+\mu^-} < 4.4$ GeV/c^2 of the analysis, the $J/\psi(\to \mu^+\mu^-)$ and $\psi'(\to \mu^+\mu^-)$ resonances are excluded with cut-out regions that cover $\pm 5\sigma$ wide windows around the observed resonance masses. The selected B_s^0 candidate is further requested to have $p_t(B) > 5$ GeV/c.

For the final event selection the same three discriminating variables (isolation, pointing angle and transverse decay length significance) are used that were also employed in the DØ analysis for the search of $B_s^0 \to \mu^+\mu^-$. The signal box is kept hidden during the whole analysis and background is determined by interpolation from the two sidebands, that are chosen to be sufficiently far away from the signal region. The optimal set of cuts is found in a random grid search by maximizing the sensitivity $P = \epsilon_{\phi\mu\mu}/(1 + \sqrt{N_{Back}})$. Here, $\epsilon_{\phi\mu\mu}$ is the reconstruction efficiency of the signal MC after the pre-selection and N_{Back} is the expected number of background events extrapolated from the sidebands. The total signal efficiency

relative to pre-selection of the three discriminating cuts is $(54 \pm 3)\%$. A linear extrapolation of the sideband population for the whole data sample into the final signal region yields an expected number of background events of 1.6±0.4. After opening the box and examining the signal region, zero events were found. The Poisson probability of observing zero events for an expected background of 1.6 ± 0.4 is $p = 0.22$. Figure 5.36 shows the remaining background events populating the lower and upper sidebands.

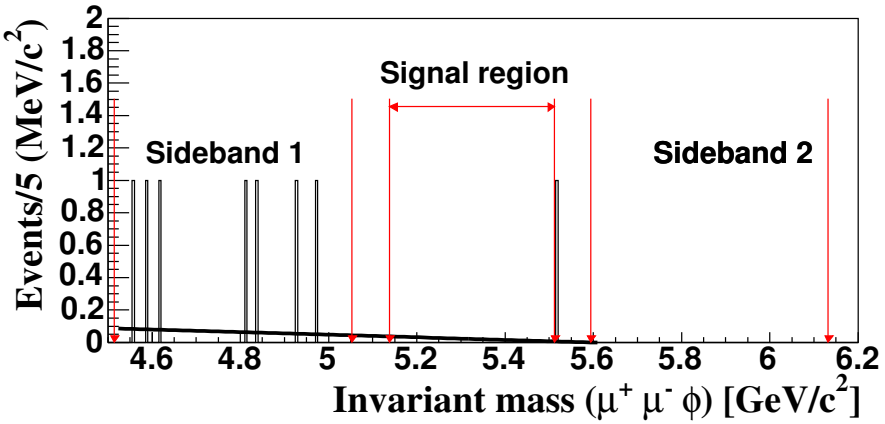

Figure 5.36: The invariant mass distribution for the full data sample after optimization. Zero events were found in the signal region.

In the absence of a signal in the search region an upper limit on the ratio $(B_s^0 \to \phi\,\mu^+\mu^-/B_s^0 \to J/\psi\,\phi)$ can be calculated

$$\frac{\mathcal{B}(B_s^0 \to \phi\,\mu^+\mu^-)}{\mathcal{B}(B_s^0 \to J/\psi\phi)} = \frac{N_{\rm ul}(N_{obs}, N_{back})}{N_{B_s^0}} \cdot \frac{\epsilon_{J/\psi\phi}}{\epsilon_{\phi\mu\mu}} \cdot \mathcal{B}(J/\psi \to \mu\mu), \tag{5.53}$$

where $N_{\rm ul}(N_{obs}, N_{back})$ is the calculated upper limit for N_{obs} observed events while N_{back} are expected. The number of reconstructed normalization events is $N_{B_s^0}$ and $\epsilon_{\phi\mu\mu}$ and $\epsilon_{J/\psi\phi}$ are the efficiencies of the signal and normalization channels. The signal efficiency is based on the input for the NNLO Wilson coefficients and form factors of Ref. [78] and no theoretical uncertainty is included in the systematics. The final limit is

$$\mathcal{B}(B_s^0 \to \phi\,\mu^+\mu^-)/\mathcal{B}(B_s^0 \to J/\psi\,\phi) < 4.4\,(3.5) \times 10^{-3}$$

at 95% (90%) C.L., respectively. Using only the central value of the world average branching fraction [8] of $\mathcal{B}(B_s^0 \to J/\psi\,\phi) = 9.3 \pm 3.3 \cdot 10^{-4}$, this limit corresponds to $\mathcal{B}(B_s^0 \to \phi\,\mu^+\mu^-) = 4.1\,(3.2) \cdot 10^{-6}$ at 95% (90%) C.L. respectively.

Since the search yielded less observed events than expected, it is good statistical practice to also quote the sensitivity of the search, i.e., the ensemble average of all expected upper limits in the absence of a signal for a hypothetical repetition of the experiment. Assuming there is only background a 95% C.L. upper limit weighted by the Poisson probability of occurrence for each possible value of observation is calculated. Including the statistical and systematical uncertainties the sensitivity is then given by

$$\langle \mathcal{B}(B_s^0 \to \phi\,\mu^+\mu^-)/\mathcal{B}(B_s^0 \to J/\psi\,\phi) \rangle = 1.1\,(1.2) \times 10^{-2}$$

at 95% C.L. using the Feldman and Cousins (Bayesian) approach, respectively.

It is important to note that the SM calculation of $\mathcal{B}(B_s^0 \to \phi\,\mu^+\mu^-) = 1.6 \times 10^{-6}$ in Ref. [85] does not correctly incorporate the size of the cut-out regions around the charmonium resonances. The experimental cuts as they are effectively applied in the DØ analysis are wider due to a finite mass resolution and decrease the "visible" branching fraction of the non-resonant decay considerably. A new SM calculation [152] taking into account the DØ cuts was therefore carried out, leading to $\mathcal{B}'(B_s^0 \to \phi\,\mu^+\mu^-) = 0.7 \times 10^{-6}$, i.e., significantly below the aforementioned SM calculation.

5.4.2 Future reach at Tevatron

The future DØ reach for the search of $B_s^0 \to \phi\,\mu^+\mu^-$ is presented in Fig. 5.37. It shows the expected average upper limit as a function of integrated luminosity for the decay. The predicted SM branching fraction [152] for the invariant dimuon mass regions as used by DØ is indicated as a horizontal band. The extrapolation was obtained by scaling the number of background and normalization events according to the total integrated luminosity. A re-optimisation for each point was not performed since the expected number of background events is still reasonably small even at higher integrated luminosities. The limit band indicates a ±10% variation of the number of normalization events. The SM branching fraction might be reachable with an integrated luminosity of 16 fb^{-1}, but that is far beyond the optimistic scenario of Tevatron's Run II.

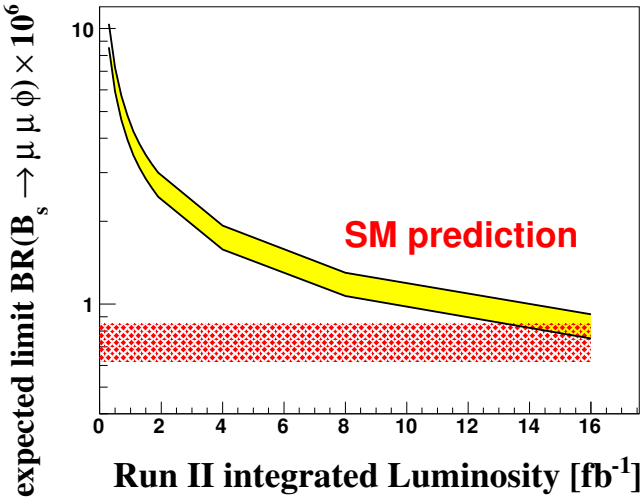

Figure 5.37: Expected average upper limit at a 95% C.L. for the decay $B_s^0 \to \mu^+\mu^-\phi$ as a function of integrated luminosity.

For the DØ search program, it is almost impossible to achieve a SM sensitivity to an exclusive $b \to s\mu^+\mu^-$ penguin decay in the B_s^0 meson system. A drawback of DØ is certainly the large di-muon mass resolution which leads to a removal of large parts of the non-resonant signal region when cutting out the charmonium resonances in the analysis. The situation should be more advantageous at CDF which has a di-muon mass resolution that is more than

three times better.

5.4.3 Exclusive Rare B Decays at LHC

Due to the high luminosity and the more favorable $\sigma_{b\bar{b}}/\sigma_{had}$ at LHC many exclusive rare B decays will be measured with high precision. This includes exclusive B decays based on $b \to (s,d)\gamma$ transitions as well as $b \to (s,d)\mu^+\mu^-$ processes. While several of these channels have already been observed at Belle and Babar in case of decaying B_d^0 mesons, the experiments at LHC, and in particular LHCb, will certainly measure the modes for the B_s^0 meson system. In any addition, LHC will provide a radically increased statistics and much more measurements in the global field of exclusive rare B decays.

Radiative Rare B Decays
The exclusive radiative penguin decays that have been evaluated so far for LHC are:

$$B_d^0 \to K^{*0}\gamma;\ B_d^0 \to \omega\gamma \text{ and } B_s^0 \to \phi\gamma$$

Table 5.18 summarizes the LHCb and Atlas expectations after one year of running at 2×10^{32} cm^{-2}s^{-1} for LHCb and 2×10^{33} cm^{-2}s^{-1} for Atlas. The data corresponds then to 2 fb^{-1} for LHCb and 20 fb^{-1} for Atlas.

Table 5.18: Expected event yields for exclusive radiative B decays after one year of LHC.

	$B_d^0 \to K^{*0}\gamma$	$B_d^0 \to \omega\gamma$	$B_s^0 \to \phi\gamma$	Ref.
LHCb	35000	40	9300	[153]
Atlas	5700	–	2300	[154]

Due to the dedicated B triggers, the LHCb expectations for the signal yields are clearly higher than at Atlas. The estimated LHCb trigger efficiencies for the radiative modes are 34-38% with selection efficiencies varying from 0.64% for the $B_d^0 \to K^{*0}\gamma$ to 0.03% for $B_d^0 \to \omega\gamma$. For the latter mode, the reconstruction of the decay $\omega \to \pi^+\pi^-\pi^0$ is complicated by the π^0 reconstruction.

Due to lack of simulated background events, the signal to background ratios S/B can not be precisely evaluated. However, it is expected that S/B for the $B_s^0 \to \phi\gamma$ decay for instance, will be at least greater than 0.4 for LHCb and larger than a few percent for Atlas. Hence, a clear observation of these radiative decays could be possible after one year of LHC.

Rare B Decays with Di-muons
The di-muons in the final state that come from $b \to s(d)\mu^+\mu^-$ exclusive B decays are easier to select than radiative decays. This remark is particularly true for Atlas and CMS, which are limited to muon-based B triggers. One of the prime candidates for $b \to s\mu^+\mu^-$ transitions to study is the decay $B_d^0 \to K^{*0}\mu^+\mu^-$, whose signal yields were evaluated for Atlas, CMS and LHCb. As mentioned in the previous chapter, large statistics of this type of decay gives access to interesting observables which – when measured with sufficient precision – allow tight constraints on the Wilson coefficients and hence on contributions of new physics.

Table 5.19: Expected event yields for the exclusive electroweak penguin decay $B_d^0 \to K^{*0}\mu^+\mu^-$ after one year of LHC.

	$B_d^0 \to K^{*0}\mu^+\mu^-$	Ref.
CMS	8000	[155]
LHCb	4400	[156]
Atlas	3000	[157]

Tab. 5.19 summarizes the statistics for one year at low luminosity. The luminosity assumptions are 2 fb^{-1} for LHCb and 30 fb^{-1} for Atlas/CMS.

A large sample of $B_d^0 \to K^{*0}\mu^+\mu^-$ can be selected at LHC. The expected LHC sample after one year can be compared to the presently available number of 113.6 ± 13 $B \to K^{*0}\ell^+\ell^-$ decays at Belle, that were recorded in 386 million $B\bar{B}$ pairs.

The Atlas and LHCb results have been obtained with the full detector simulation of the latest detector layout. The CMS result refers only to an older version of the detector layout. In addition, the CMS study was done only on the particle level, explaining the large discrepancy between the numbers for Atlas and CMS. Due to the specific di-muon trigger the signal significance will be radically larger than for radiative decays and clean signals should be observed after one year of running.

At LHCb it is expected to measure the branching ratio after the first year in both interesting q^2 regions. In the low-q^2 region, defined between 1-6 GeV^2, the anticipated accuracy is $\pm 6\%$, while the branching ratio of the high-q^2 region (> 14 GeV^2) can be determined with $\pm 3\%$ relative uncertainty. The large statistics for this decay allows also to extract the zero of $A_{FB}(q^2)$ and hence the ratio of the Wilson coefficients C_7^{eff}/C_9^{eff} with an accuracy of 13% after five years of LHCb data taking. This measurement will then represent a very clean test of new physics with a potential huge phenomenological impact.

Other exclusive decays that are based on electroweak penguins are $B_d^0 \to \rho\,\mu^+\mu^-$ and $B_s^0 \to \phi\,\mu^+\mu^-$. It is possible to observe both decays at LHCb in the first year. Their statistics however, will not be sufficient to allow an elaborated analysis of $A_{FB}(q^2)$ as in the case of $B_d^0 \to K^{*0}\mu^+\mu^-$.

5.5 Rare Decays of b-Baryons

With the high b production rate on the one side and the access to all sorts of flavored b-hadrons on the other side, a high luminosity hadron collider such as LHC offers a plethora of new opportunities in flavor physics. A new territory is given by the study of CP violation effects in b-baryons [89]. Since baryon number is conserved, neither tagging nor time-dependent measurements for b-baryon decays are required which is in contrast to neutral B meson modes. There are several baryon decay modes that are expected to have sizeable CP violation effects. Of general interest are further the investigation of all rare b-baryon decays that are induced by quark transitions such as $b \to s\gamma$ and $b \to s\ell^+\ell^-$ that also appear in mesonic counterparts. A study of these decay processes is also an important test of the understanding of the quark-hadron dynamics.

Table 5.20 presents an overview of b-baryons, their quark content, (expected) mass and rough estimated production rates relative to $\sigma_{b\bar{b}}$ at LHC. On the experimental side, there is still some work to do, since the only b-baryon, that has been experimentally unambiguously observed is the Λ_b^0, whose mass and lifetime have been measured. However, there exists clear evidences of the production of a mixture of Ξ_b^0 and Ξ_b^- at LEP [158]. All the other b-baryons are still awaiting their discovery. The predictions for the masses of some (yet) unobserved b-baryons are taken from a recent quark model calculation of Ref. [159], while the rate estimations are taken from Ref. [160]. There are also beauty baryons with double-charm and double-b content which are not listed in the table. Their production is further suppressed, since additional heavy quarks have to produced in the fragmentation.

Table 5.20: Overview of some b-baryons.

Name	quark content	charge	mass (MeV/c^2)	$\sigma_{baryon}/\sigma_{b\bar{b}}$
Λ_b^0	udb	0	5624 ± 9 (exp.)	$(9.4 \pm 0.6) \times 10^{-2}$
Σ_b^-	ddb	-1	5824.2 ± 9.0	$(6.0 \pm 0.2) \times 10^{-3}$
Σ_b^0	udb	0	5824.2 ± 9.0	$(6.0 \pm 0.2) \times 10^{-3}$
Σ_b^+	uub	+1	5824.2 ± 9.0	$(6.0 \pm 0.2) \times 10^{-3}$
Ξ_b^0	usb	0	5805.7 ± 8.1	$(5.0 \pm 0.5) \times 10^{-3}$
Ξ_b^-	dsb	-1	5805.7 ± 8.1	$(5.0 \pm 0.5) \times 10^{-3}$
Ω_b^-	bss	-1	6068.7 ± 11.1	$\sim 5 \times 10^{-4}$

In the context of a FCNC program the interesting rare decays for b-baryons are the electroweak penguin decays. As in the meson system there are $b \to (d,s)\gamma$ or $b \to (d,s)\ell^+\ell^-$ transitions possible. Examples for $b \to d\gamma$ processes are:

$$\Lambda_b^0 \to n\gamma,\ \Xi_b^0 \to \Lambda^0\gamma,\ \Xi_b^0 \to \Sigma^0\gamma,\ \Xi_b^- \to \Sigma^-\gamma,\ \Omega_b^- \to \Xi^-\gamma$$

Examples for $b \to s\gamma$ transitions are:

$$\Lambda_b^0 \to \Lambda\gamma,\ \Xi_b^0 \to \Xi^0\gamma,\ \Xi_b^- \to \Xi^-\gamma,\ \Omega_b^- \to \Omega^-\gamma$$

Replacing the γ with a $\ell^+\ell^-$ pair leads then to the corresponding $b \to (d,s)\ell^+\ell^-$ processes. The branching ratios of the listed decays should typically have branching fractions between 10^{-7} and 10^{-5}. With the exception of some of the rare Λ_b^0 decays [68, 90], they have not yet been estimated in the SM. It is thus desirable, to have theoretical progress in order to guide the experimentalists towards the optimal modes.

From the experimental point of view, not all b-baryon decays are suitable for a measurement. Rather clean modes are Λ_b^0 and Ξ_b baryons decaying into $\Lambda^0 \to p\pi$ plus either a hard photon or a lepton pair in the final state.

A search or measurement of the $\Lambda_b^0 \to \Lambda^0\mu^+\mu^-$ and $\Xi_b^0 \to \Lambda^0\mu^+\mu^-$ decays can be carried out in complete analogy to the presented $B_s^0 \to \phi\,\mu^+\mu^-$ analysis. The measured decay $\Lambda_b^0 \to J/\psi\Lambda^0$ with a branching ratio of $(4.7 \pm 2.8) \times 10^{-4}$ serves best as normalization channel, since signal and normalization mode have the same final state. For the signal channel, the

regions of the charmonium resonances in the di-muon mass spectrum have to be excluded as well. A rough estimation of the DØ reach for $\Lambda_b^0 \to \Lambda\mu^+\mu^-$ can be obtained from

$$\langle \mathcal{B}(\Lambda_b^0 \to \Lambda^0\mu^+\mu^-)\rangle = \frac{< N_{ul} >}{N_{J/\psi\Lambda}} \times \frac{\epsilon_{J/\psi\Lambda}}{\epsilon_{\mu\mu\Lambda}} \times \mathcal{B}(J/\psi \to \mu^+\mu^-) \times \mathcal{B}(\Lambda_b^0 \to \Lambda^0 J/\psi) \qquad (5.54)$$

Assuming a similar efficiency ratio of $\epsilon_{J/\psi\Lambda}/\epsilon_{\mu\mu\Lambda}$ for the normalization mode relativ to the signal channel as in the $B_s^0 \to \phi\mu^+\mu^-$ analysis and a (conservative) 50% smaller Λ_b^0 production with respect to B_s^0 in fragmentation, a sensitivity of about $2{\times}10^{-2}{\times}\mathcal{B}(\Lambda_b^0 \to \Lambda J/\psi) \approx 1{\times}10^{-5}$ could be reached already with existing DØ data of 300 pb^{-1}.

A search for $\Lambda_b^0 \to \Lambda^0\mu^+\mu^-$ decays has much in common with the existing $B_s^0 \to \phi\,\mu^+\mu^-$ analysis at DØ such as data sets, analysis technique and trigger systematics. It is therefore worthwhile to pursue it at DØ as well.

Similar arguments as above hold in principle also for $\Xi_b^0 \to \Lambda^0\mu^+\mu^-$ decays. The decay could be normalized to the (not yet observed) $\Xi_b^0 \to J/\psi\Lambda^0$ decay, such that signal and normalization channels are of almost equal topology. The branching ratio of the normalization mode has not yet been theoretically calculated, but might be naively estimated from $\mathcal{B}(\Lambda_b^0 \to J/\psi\Lambda^0)$ with the help of the underlying quark process. The decay $\Lambda_b^0 \to J/\psi\Lambda^0$ is based on the $b \to cW(\to \bar{c}s)$, while $\Xi_b^0 \to J/\psi\Lambda^0$ proceeds via $b \to cW(\to \bar{c}d)$ such that

$$R_{\mathcal{B}} = \frac{\mathcal{B}(\Lambda_b^0 \to J/\psi\Lambda^0)}{\mathcal{B}(\Xi_b^0 \to J/\psi\Lambda^0)} \approx \frac{|V_{cb}V_{cs}|^2}{|V_{cb}V_{cd}|^2} \approx 20 \qquad (5.55)$$

This very crude and naive estimation leads then to $\mathcal{B}(\Xi_b^0 \to J/\psi\Lambda^0) \approx 2 \times 10^{-5}$.

It is interesting to understand if the resonant decay might be discovered at Tevatron towards the end of Run II with high statistics. This could then be the first step towards the search for non-resonant $\Xi_b^0 \to \Lambda^0\mu^+\mu^-$ decays at LHC. The achieved DØ mass resolution of reconstructed $\Lambda_b^0 \to \Lambda^0 J/\psi$ decays is about 40 MeV, while the mass difference between the Λ_b^0 and Ξ_b^0 baryons corresponds to 180 MeV making a mass separation in principle possible.

In the Λ_b^0 lifetime analysis [161], DØ detected about 60 $\Lambda_b^0 \to J/\psi\Lambda^0$ events in 250 pb^{-1} of data. Assuming the same detection efficiency for $\Xi_b^0 \to J/\psi\Lambda^0$ and a fragmentation ratio of $f(\Lambda_b^0)/f(\Xi_b^0) \approx= 0.1/(5 \times 10^{-3}) = 20$ for the production of the Λ_b^0 baryon relative to the Ξ_b^0, about $N_{\Xi^0} \approx 60/(20 \cdot 20) = 0.15$ events per 250 pb^{-1} are expected. Thus, an observation of $\Xi_b \to J/\psi\Lambda^0$ at DØ could be only possible with significant luminosity, i.e., at the end of Run II.

As a final remark it should be mentioned, that the investigation of rare baryon decays will be part of the long-term physics program of LHCb. First MC studies of $\Lambda_b^0 \to \Lambda^0\gamma$ decays are presently underway.

6 Summary

Although the SM of particle physics offers a very successful description of strong and electroweak interactions, it is only supposed to be an effective theory valid at low energies. Thus, the SM is likely to be embedded in a more fundamental theory having additional degrees of freedom.

One of the most important tasks of the upcoming LHC is to unravel the deeper structure of the underlying theory. In that respect, much progress can be expected from direct experimental searches for new particles, as well as from measurements which are indirectly sensitive to contributions from new physics.

One crucial aspect of flavor physics is to search or to constrain the new degrees of freedom beyond the SM. A decisive role in such tests is played by flavor-changing neutral currents, which are absent at the tree level, but proceed in higher order diagrams. Due to virtual loop contributions from new particles, the investigation of FCNC decays can reveal physics at a higher scale even before direct access to such energies is available.

This work reviewed the present experimental status of rare FCNC decays in the B sector. The experimental facilities that are capable of doing B physics were presented. In contrast to e^+e^- annihilation machines, hadron colliders such as the LHC offer the great advantage of a high $b\bar{b}$ cross section with more than $\mathcal{O}(10^{12})$ produced $b\bar{b}$ events per year. The other big asset is the access to all sort of b-flavored hadrons and to study flavor physics in several bound b-systems. At hadron colliders however, $b\bar{b}$ events represent only a small fraction of all events, such that dedicated triggers for B physics are essential. Other detector key elements for a successful B physics program are position sensitive detectors that are typically based on semiconductor technology and achieve excellent vertex resolution and a highly efficient tracking.

In the field of flavor physics, the prime decay candidate for a new physics search at hadron colliders is definitively the decay $B_s^0 \to \mu^+\mu^-$. This decay is helicity suppressed and features an enormous sensitivity to new physics, in particular if new chirality flipping operators become important. Those operators are very small in the SM but are greatly enhanced at high $\tan\beta$ in supersymmetric extensions of the SM. The $B_s^0 \to \mu^+\mu^-$ decay is theoretically very clean and – on a mid-term perspective – is probably one of the most interesting items in B physics at hadron colliders.

At the Tevatron, this decay belongs now to the core physics program of Run II. The search analysis for this decay was described and the combined Tevatron limit of $\mathcal{B}(B_s^0 \to \mu^+\mu^-) < 1.2 \times 10^{-7}$ at a 90% C.L. presented. The Tevatron exclusion potential for this decay is expected to be 2×10^{-8} at a 90% C.L. if a luminosity of 8 fb^{-1} for each experiment at the end of Run II is available. The Tevatron reach will not suffice to reach the SM sensitivity of this decay but its limit will have significant phenomenological impact on supersymmetric models at high $\tan\beta$. Concerning the phenomenology of new physics at Tevatron, it might be an interesting and probably powerful way to further constrain minimal flavor violating supersymmetry by better exploiting the strong correlations between $B_s^0 \to \mu^+\mu^-$ and ΔM_s, since both observables are simultaneously being probed at Tevatron.

In case of no observation of $B_s^0 \to \mu^+\mu^-$ events at Tevatron, it is expected to discover or at least find strong evidence for this channel after one year of LHC running. Atlas, CMS and LHCb have studied this decay and anticipate to collect enough events for a significant signal if the value of the SM branching ratio is assumed. Beside the measurement of the B_s^0

leptonic decay at LHC, its B_d^0 decay counterpart should not be forgotten. A very clean test of the minimal flavor violation assumption consists in a measurement of the ratio $\mathcal{B}(B_s^0 \to \mu^+\mu^-)/\mathcal{B}(B_d^0 \to \mu^+\mu^-) \propto |V_{ts}|^2/|V_{td}|^2$. It is therefore important to probe such relations as a long-term prospect at LHC as well.

The leptonic decay $B_s^0 \to \tau^+\tau^-$ features the same sensitivity to new physics but has a larger SM branching ratio than the muonic decay. It was pointed out in this work, that the decay is extremely difficult to isolate due to at least two missing neutrinos in the final state and due to the large background from low-momentum τ's. So far, there is no MC study on this topic, but it might be worth to investigate this decay and to evaluate its feasibility for LHC.

Beside the leptonic decays $B_{d,s}^0 \to \mu^+\mu^-$, it is also interesting to look at the closely related Dalitz decays $B_{d,s}^0 \to \mu^+\mu^-\gamma$. Those decays do not suffer from helicity suppression and may offer additional interesting observables as probe of new physics. A first analysis idea was sketched by normalizing this decay to $B^\pm \to \chi_{c1}^0 K^+$. The Dalitz decay can be probably measured at LHCb after a few years, but no dedicated MC study exists.

Electroweak penguin decays of B_d^0 mesons that are mediated by $b \to s\gamma$ and $b \to s\ell^+\ell^-$ decays are one of the main aspects of the Babar and Belle physics program and much progress over the last years has been made. At Tevatron there is no real chance to be competitive, but searches for exclusive electroweak penguin decays in the B_s^0 meson system should clearly be continued. The upper limit of $\mathcal{B}(B_s^0 \to \phi\,\mu^+\mu^-) < 3.2 \times 10^{-6}$ at a 90% C.L. obtained by DØ was presented. Unfortunately, the future expected sensitivity at DØ will not be sufficient to reach the SM value of this decay, mainly due to the mass resolution of the detector. The situation however, will be different at LHC. For instance LHCb, can detect within one year a large sample of the exclusive decay $B_d^0 \to K^{*0}\mu^+\mu^-$ containing about $1000\times$ more statistics than what is presently available at e^+e^- machines. The high-statistics sample can be analyzed to extract useful information on the Wilson coefficients from the forward-backward asymmetry observable.

Finally, there is the possibility to access rare b-baryon decays at LHC. This field is almost completely unexplored and offers beside FCNC decays also interesting CP-violating phenomena. Much more theoretical input is necessary that helps to guide the experimenters in selecting the interesting decay modes that are worth for a search analysis or measurement. A first search for $\Lambda_b^0 \to \Lambda^0\mu^+\mu^-$ decays could be carried out at DØ in a rather straightforward way. The analysis method is in complete analogy to the search for $B_s^0 \to \phi\,\mu^+\mu^-$ using $\Lambda_b^0 \to J/\psi\phi$ as normalizing mode.

Historically, the search for FCNC decays and its measurement have significantly helped to shape and form the SM of particle physics. It could be very likely that this situation will occur once more, when LHC will hopefully reveal the underlying structure of a more complete theory beyond the SM.

References

[1] B. Aubert *et al.* [Babar Collab.], Nucl. Instr. Meth. **A479**, 1 (2002).

[2] A. Abashian *et al.* [Belle Collab.], Nucl. Instr. Meth. **A479**, 117 (2002).

[3] S. Hashimoto *et al.*, KEK-Report-2004-4; J. Seeman *et al.*, SLAC-Pub-10547, 2004.

[4] G. Bonvicini *el.* [CLEO Coll.], hep-ex-0510034.

[5] P. Nason, S. Dawson and R. K. Ellis, Nucl. Phys. **B327**, 49 (1989), Erratum-ibid. **B335**, 260 (1990); M. L. Mangano, P. Nason and G. Ridolfi, Nucl. Phys. **B373**, 295 (1992).

[6] For a review, see for example: M. Mangano, AIP Conf. Proc. 753, 247 (2005); hep-ph/0411020.

[7] S. Frixione, Proceedings of XII. Workshop on Deep Inelastic Scattering, Strbske Pleso, Slovakia, March 2004.

[8] S. Eidelman *et al.*, Phys. Lett. **B592**, 1 (2004).

[9] E. Barberio *et al.*, Heavy Flavor Averaging Working Group (HFAG), hep-ex/0505100.

[10] D. Acosta *et al.* [CDF Collab.], Phys. Rev. **D69**, 012002 (2004).

[11] S. Abachi *et al.* [DØ Collab.], Nucl. Instr. Meth A **338**, 185 (1994).

[12] S. Abachi *et al.* [DØ Collab.], FERMILAB-Pub-96/357-E.

[13] V. Abazov *et al.* [DØ Collab.], FERMILAB-Pub-05-341-E.

[14] LHCb Collab., Reoptimized Detector Design and Performance Technical Design Report, CERN-LHCC/2003-30.

[15] LHCb Collab., LHCb VELO Technical Design Report, CERN-LHCC/2001-11.

[16] LHCb Collab., LHCb RICH Technical Design Report, CERN-LHCC/2000-37.

[17] LHCb Collab., LHCb Calorimeters Technical Design Report, CERN-LHCC/2000-36.

[18] LHCb Collab., LHCb Muon System Technical Design Report, CERN-LHCC/2001-10.

[19] G. Charpak *et al.*, Nucl. Phys. Meth. **A306**, 439 (1991).

[20] N. Ellis and A. Kernan, Phys. Rept. **195**, 23 (1990).

[21] B. Ashmanskas *et al.*, Nucl. Instrum. Meth. **A518**, 532 (2004).

[22] B. Abbott *et al.*, DØ note 4318.

[23] LHCb Collab., LHCb Trigger System Technical Design Report, CERN-LHCC/2003-31.

[24] J. Kemmer, Nucl. Instr. Meth. **A169**, 499 (1980).

[25] F. Bedeschi *et al.*, IEEE Trans. Nucl. Sci. **33**, 140 (1986).

[26] F. Lehner, Nucl. Instr. Meth. **A447**, 9 (2000).

[27] F. Lehner, Nucl. Instr. Meth. **A530**, 105 (2003); J. Gardner *et al.*, DØ note 3962.

[28] DØ Collab., FERMILAB-PUB-02-327-E.

[29] DØ Collab. , DØ Layer 0 Conceptual Deasign Report, October 2003.

[30] LHCb Collab., LHCb Inner Tracker Technical Design Report, CERN-LHCC/2002-29.

[31] J. Gassner *et al.*, LHCb notes 2004-109 and 2004-110.

[32] N. van Bakel, The Beetle Reference Manual, http://wwwasic.kip.uni-heidelberg.de

[33] F. Lehner, Proceedings of the 11th Workshop on Electronics for LHC and future Experiments, Heidelberg, 12 - 16 September 2005.

[34] S.W. Herb *et al.*, Phys. Rev. Lett. **39**, 252 (1977).

[35] C. Berger *el al.*, Phys. Lett. **B76**, 243 (1978); C.W. Darden *et al.*, Phys. Lett. **B78**, 246 (1978); J.K. Bienlein *et al.*, Phys. Lett. **B78**, 360 (1978).

[36] M.E. Nelson *et al.*, Phys. Rev. Lett. **50**, 1542 (1980).

[37] C. Albajar *et al.* [UA1 Collab.], Phys. Lett. **B186**, 247 (1987).

[38] H. Albrecht *et al.* [ARGUS Collab.], Phys. Lett. **B192**, 245 (1987).

[39] R. Ammar *et al.* [CLEO Collab.], Phys. Rev. Lett. **71**, 674 (1993).

[40] K. Abe *et al.* [Belle Collab.], Phys. Rev. Lett. **87**, 091802 (2002); B. Aubert *et al.* [Babar Collab.], Phys. Rev. Lett. **87**, 091801 (2002).

[41] N. Cabibbo, Phys. Rev. Lett. **10**, 531 (1963); M. Kobayashi and K. Maskawa, Prog. Theor. Phys. **49**, 652 (1973).

[42] D. Cline, Proceedings of Ecol. Int. Hecg. Novi (1967), and Thesis at Univ. of Wisconsin (1965).

[43] S. L. Glashow, J. Iliopoulos and L. Maiani, Phys. Rev. **D2**, 1285 (1970).

[44] M. K. Gaillard and B. W. Lee, Phys. Rev. **D10**, 897 (1974).

[45] J. J. Aubert *et al.*, Phys. Rev. Lett. **33**, 1404 (1974).

[46] J. E. Augustin *et al.*, Phys. Rev. Lett. **33**, 1406 (1974).

[47] J. R. Ellis *et al.*, Nucl. Phys. **B131**, 285 (1977).

[48] M. Gronau and D. London, Phys. Rev. **D55**, 2845 (1997); F. del Aguila *et al.*, Nucl. Phys. **B510**, 39 (1998); G. Barenboim *et al.*, Phys. Rev. **D64**, 015007 (2001).

[49] T. M. Aliev, A. Ozpineci and M. Savci, Eur. Phys. J **C29**, 265 (2003).

[50] R. Mohanta, Phys. Rev. **D71**, 114013 (2005).

[51] C. D. Carone and R. T. Hamilton, Phys. Lett. B **301**, 196 (1993).

[52] G. Valencia and S. Willenbrock, Phys. Rev. **D50**, 6843 (1994); M. Herz, hep-ph/0301079.

[53] N. Arkani-Hamed, S. Dimopolous and G. R. Dvali, Phys. Rev. **D59**, 086004 (1999).

[54] G. Kane, C. Kolda and J. Lennon, hep-ph/0310042.

[55] S. Glashow and S. Weinberg, Phys. Rev. **D15**, 1958 (1977).

[56] A. Chamseddine *et al.*, Phys. Rev. Lett. **49**, 970 (1982); R. Barbieri *et al.*, Phys. Lett. **B119**, 343 (1982); L. J. Hall *et al.*, Phys. Rev. **D27**, 2359 (1983).

[57] S. R. Choudhury and N. Gaur, Phys. Lett. **B451**, 86 (1998); C.-S. Huang and Q.-S. Yan, Phys. Lett. **B442**, 209 (1998); K. Babu and C. Kolda, Phys. Rev. Lett. **84**, 228 (2000).

[58] A. Dedes, Mod. Phys. Lett. **A18**, 2627 (2003).

[59] C. Greub, T. Hurth and D. Wyler, Phys. Rev. **D54**, 3350 (1996). A. J. Buras, A. Czarnecki, M. Misiak and J. Urban, Nucl. Phys. **B611**, 488 (2001), ibid. **631**, 219 (2002).

[60] P. Gambino and U. Haisch, JHEP, 0110, 020 (2001).

[61] F. Borzumati and C. Greub, Phys. Rev. **D58**, 074004 (1998); M. Ciuchini *et al.*, Nucl. Phys. **B534**, 3 (1998); M. Carena *et al.*, Phys. Lett. **B499**, 141 (2001).

[62] P. Gambino and M. Misiak, Nucl. Phys. **B611**, 338 (2001).

[63] K. Abe *et al.* [Belle Collab.], hep-ex/0506079; B. Aubert *et al.* [Babar Collab.], Phys. Rev. Lett **94**, 011801 (2005).

[64] L. Silvestrini, Proceedings of XV. Lepton-Photon Conference, Uppsala 2005, hep-ph/0510077.

[65] W. Adam *et al.* [Delphi Collab.], Z. Phys. **C72**, 207 (1996).

[66] D. Acosta *et al.* [CDF Collab.], Phys. Rev. **D66**, 112002 (2002).

[67] A. Ali, Nucl. Instrum. Meth. **A384**, 8 (1996).

[68] H.-Y. Cheng and K.-C. Yang, Phys. Lett. **B533**, 271 (2002).

[69] A. Ghinculov *et al.*, Nucl. Phys. **B648**, 254 (2003). H. M. Asatrian *et al.*, Phys. Rev. **D66**, 094013 (2002).

[70] H. H. Asatrian, H. M. Asatrian, C. Greub and M. Wallker, Phys. Lett. **B507**, 162 (2001); Phys. Rev. **D65**, 074004 (2002); Phys. Rev. **D66**, 034009 (2002). A. Ghinculov *et al.*, Nucl. Phys. Proc. Suppl., **116**, 284 (2003).

[71] T. Hurth, Rev. Mod. Phys. **75**, 1159 (2003).

[72] J. Kaneko *et al.* [Belle Collab.], Phys. Rev. Lett. **90**, 021801 (2003).

[73] B. Aubert *et al.* [Babar Collab.], hep-ex/0308016.

[74] M. Iwasaki *et al.* [Belle Coll.], Phys. Rev. **D72**, 092005 (2005).

[75] A. Ghinculov *et al.*, Nucl. Phys. **B675**, 351 (2004).

[76] A. Ali, E. Lunghi, C. Greub and G. Hiller, Phys. Rev. **D66**, 034002 (2002).

[77] A. Ali, G. Hiller, L. T. Handoko and T. Morozumi, Phys. Rev. **D55**, 4105 (1997).

[78] A. Ali, P. Ball, L.T. Handoko and G. Hiller, Phys. Rev. **D61**, 074024 (2000).

[79] D. Melikhov, N. Nikitin and S. Simula, Phys. Lett. **B410**, 290 (1997).

[80] K. Abe *et al.* [Belle Collab.], Phys. Rev. Lett. **88**, 021801 (2002).

[81] A. Ishikawa *et al.* [Belle Collab.], Phys. Rev. Lett. **91**, 261601,(2003).

[82] B. Aubert *et al.* [Babar Collab.], Phys. Rev. Lett. **91**, 221802, (2003).

[83] K. Abe *et al.* [Belle Collab.], hep-ex/0410006.

[84] K. Abe *et al.* [Belle Collab.], hep-ex/0508009.

[85] C.-Q. Geng and C. C. Liu, J. Phys. **G29**, 1103 (2003).

[86] A. Deandrea and A. Polosa, Phys. Rev. **D64**, 074012 (2001).

[87] G. Erkan and G. Turan, Eur. Phys. J. **C25**, 575 (2002).

[88] V. Abazov *et al.*, [DØ Collab.], DØ note 4862-Conf.

[89] I. Dunietz, Z. Phys. **C56**, 129 (1992).

[90] C.-H. Chen and C.-Q. Geng, Phys. Rev. **D64**, 074001 (2001);

[91] A. Buras, Proceedings of Probing the Standard Model of Particle Interactions, Les Houches 1997, hep-ph/9806471.

[92] R. Barate *et al.* [ALEPH Collab.], Eur. Phys. J. **C19**, 213 (2001).

[93] Y. Grossman, Z. Ligeti and E. Nardi, Nucl. Phys. **B465**, 369 (1996); erratum-ibid **B**480, 753 (1996).

[94] B. Aubert *et al.* [Babar Collab.], hep-ex/0207069 and hep-ph/0304020.

[95] K. Abe *et al.* [Belle Collab.], hep-ex/0507034.

[96] G. Buchalla, G. Hiller and G. Isidori, Phys. Rev **D63**, 014015 (2001).

[97] B. Grzadkowski and P. Krawczyk, Z. Phys. **C18**, 43 (1983).

[98] T. Inami and C. S. Lim, Prog. Theor. Phys. **65**, 297 (1981); Erratum ibid. **65**, 1772 (1981).

[99] G. Buchalla and A. J. Buras, Nucl. Phys. **B400**, 225 (1993); M. Misiak and J. Urban, Phys. Lett. **B451**, 161 (1999).

[100] A. J. Buras, Phys. Lett. **B566**, 115 (2003).

[101] B. Aubert *et al.* [Babar Collab.], hep-ex/0408096.

[102] M. Acciarri *et al.* [L3 Collab.], Phys. Lett. **B391**, 474 (1997).

[103] R. Bernhard *et al.*, hep-ex/0508058.

[104] B. Aubert *et al.* [Babar Collab.], hep-ex/0511015.

[105] See for example: G. Isidori, AIP Conf. Proc. **722**, 181 (2004) and references therein.

[106] L. T. Handoko *et al.*, Phys. Rev. **D65**, 077506 (2002).

[107] H. E. Logan and U. Nierste, Nucl. Phys. **B586**, 39 (2000).

[108] S. R. Choudary and N. Gaur, Phys. Lett. **B451**, 86 (1999); C. S. Huang, W. Liao, Q. S. Yan and S. H. Zhu, Phys. Rev. **D63**, 114021 (2001), [Erratum-ibid. **D64**, 059902 (2001)]; P. H. Chankowski and L. Slawianowska, Phys. Rev. **D63**, 054012 (2001); C. Bobeth, T. Ewerth, F. Kruger and J. Urban, Phys. Rev. **D64**, 074014 (2001); K. S. Babu and C. F. Kolda, Phys. Rev. Lett. **84**, 228 (2000); G. Isidori and A. Retico, JHEP **0209**, 063 (2002); G. D'Ambrosio, G. F. Giudice, G. Isidori and A. Strumia, Nucl. Phys. **B645**, 155 (2002); A. Dedes and A. Pilaftsis, Phys. Rev. **D67**, 015012 (2003); A. J. Buras, P. H. Chankowski, J. Rosiek and L. Slawianowska, Nucl. Phys. **B659**, 3 (2003); C. S. Huang and X. H. Wu, Nucl. Phys. **B657**, 304 (2003).

[109] A. Dedes and T. Huffman, Phys. Lett. **B600**, 261 (2004).

[110] C.-S. Huang *et al.*, Eur. Phys. J. **C18**, 393 (2000); J. K. Mizukoshi *et al.*, Phys. Rev. **D66**, 115003 (2002); S. Baek *et al.* Phys. Rev. Lett. **89**, 271801 (2002).

[111] A. Dedes, H. K. Dreiner and U. Nierste, Phys. Rev. Lett. **87**, 251804 (2001); T. Ibrahim and P. Nath, Phys. Rev. **D67**, 016005 (2003); J. K. Mizukoshi, X. Tata and Y. Wang, Phys. Rev. **D66**, 115003 (2002); R. Arnowitt, B. Dutta, T. Kamon and M. Tanaka, Phys. Lett. **B538**, 121 (2002); S. Baek, P. Ko and W. Y. Song, Phys. Rev. Lett. **89**, 271801 (2002).

[112] J. K. Mizukoshi, X. Tata and Y. Wang, Phys. Rev. **D66**, 115003 (2002).

[113] G. W. Bennet *et al.*, Phys. Rev. Lett. **92**, 161802 (2004).

[114] A. Vainshtain, Prog. Part. Nucl. Phys. **55**, 451 (2005).

[115] C. L. Bennett *et al.*, Astrophys. J. Suppl. **148**, 1 (2003).

[116] S. Baek *et al.*, JHEP **0502**, 067 (2005).

[117] D.S. Akerib *et al.*, Phys. Rev. Lett. **93**, 211301 (2004).

[118] S. Baek *et al.*, hep-ph/0506115.

[119] S. Desau *et al.* [Super-K Collab.], Phys. Rev. **D70**, 083523 (2004).

[120] J. Ahrens *et al.* [Amanda Collab.], Phys. Rev **D66**, 032006 (2002).

[121] A.J. Buras *et al.*, Nucl. Phys. **B619**, 434 (2001); Phys. Lett. **B546**, 96 (2002); Nucl. Phys. **B659**, 3 (2003).

[122] J. Foster *et al.*, JHEP **0508**, 094 (2005); Phys. Lett. **B609**, 102 (2005).

[123] R. Dermisek *et al.*, JHEP **0509**,029 (2005); R. Dermisek *et al.*, JHEP **0303**, 037 (2003); T. Blazek *et al.*, Phys. Rev. Lett. **88**, 111804 (2002).

[124] J.H. Jang *et al.*, Phys. Rev. **D55**, 7296 (1997).

[125] Z. H. Xiong and J. M. Yang, Phys. Lett. **B546**, 221 (2002); L. Randall and R. Sundrum, Phys. Lett. **B312**, 148 (1993).

[126] A. J. Buras *et al.*, Nucl. Phys. **B660**, 225 (2003).

[127] P. Dey and G. Bhattacharyya, Phys. Rev. **D69**, 076009 (2004).

[128] G. Hiller and E. O. Iltan, Mod. Phys. Lett. **A12**, 2837 (1997).

[129] S. Bosch and G. Buchalla, JHEP **0208**, 054 (2002).

[130] M. Acciarri *et al.* [L3 Collab.], Phys. Lett. B **363**, 137 (1995).

[131] K. Abe *et al.* [Belle Collab.], BELLE-CONF-0522, 2005.

[132] A. Gemintern *et al.*, Phys. Rev. **D70**, 035008, 2004.

[133] B. Aubert *et al.*, Phys. Rev. **D93**, 091802 (2004).

[134] J. Chen *et al.*, hep-ph/0509093.

[135] C.-Q. Geng *et al.*, Phys. Rev. **D62**, 074017 (2000); S D. Melikhov and N. Nikitin, Phys. Rev. **D70**, 114028 (2004); Y. Dincer and L. Sehgal, Phys. Lett. **B521**, 7 (2001); G. Eilam, G. D. Lu and D.X. Zhang, Phys. Lett. **B391**, 491 (1997); T. M. Aliev, A. Öspineci and M. Savci, Phys. Rev. **D55**, 7059 (1997).

[136] R. Choudhury *et al.*, hep-ph/0504193; T. M. Aliev *et al.*, Phys. Lett. **B520**, 69 (2001).

[137] Y. Dincer and L. M. Sehgal, Phys. Lett. **B556**, 169 (2003).

[138] A. Dedes *et al.*, Phys. Lett. **B549**, 159 (2002); J.K. Parry, hep-ph/0510305.

[139] X.-G. He *et al.*, Phys.Rev. **D70**, 113011 (2004).

[140] M. L. Brooks *et al.* [MEGA Collab.], Phys. Rev. Lett. **83**, 1521 (1999).

[141] K. Hayasake *et al.* [Belle Collab.], Nucl. Phys. Proc. Suppl. **144**, 149 (2005).

[142] F. Abe *et al.* [CDF Collab.], Phys. Rev. **D57**, 3811 (1998).

[143] M.-C. Chang *et al.* [Belle Collab.], Phys. Rev. **D68**, 111101 (2003).

[144] A. Bornheim *et al.*, [CLEO Collab.], Phys. Rev. Lett. **93**, 241802 (2004).

[145] H. B. Prosper, Proceedings of the Conference on Statistical Problems in Particle Physics, Astrophysics and Cosmology (Phystat 2003), SLAC, September 2003; P. Bhat, Proceedings of the VII International Workshop on Advanced Computing & Analysis Techniques, Fermilab, October 2000.

[146] C. Albajar *et al.* [UA1 Collab.], Phys. Lett. **B209**, 385 (1988).

[147] G. Punzi, Proceedings of the Conference on Statistical Problems in Particle Physics, Astrophysics and Cosmology (Phystat 2003), SLAC, September 2003; physics/0308063.

[148] I. Betram *et al.*, Fermilab-TN-2401; J. Conway *et al.*, CDF Note 6428.

[149] O. Schneider, Talk at the Workshop "Flavour in the era of LHC", CERN, November 2005.

[150] B. de Paula, F. Marinho and S. Amato, LHCb-2003-16.

[151] D. Acosta *et al.* [CDF Collab.], Phys. Rev. **D66**, 052005 (2002).

[152] E. Lunghi, private communication.

[153] I. Belyaev, LHCb-2005-001.

[154] S. Viret, Nucl. Phys. Proc. Suppl. **142**, 420 (2005).

[155] P. Ball *et al*, hep-ph/0003238.

[156] P. Koppenburg, Talk at the Workshop "Flavour in the era of LHC", CERN, November 2005.

[157] N. Nikitine, Talk at the Workshop "Flavour in the era of LHC", CERN, November 2005.

[158] P. Abreu *et al.* [Delphi Collab.], Z. Phys. **C68**, 541 (1995); D. Buskulic *et al.* [Aleph Collab.], Phys. Lett. **B384**, 449 (1996).

[159] E. Jenkins, Phys. Rev. **D55**, 1 (1997).

[160] A. Fridman and R. Kinnunen, CERN-PPE/93-61.

[161] V. M. Abazov *et al.* [DØ Collab.], Phys. Rev. Lett. **94**, 102001 (2005).